Advancements in the GRACE and GRACE-FO Gradiometer Mode

Nikeet Prashant Pandit

A THESIS SUBMITTED TO THE FACULTY OF GRADUATE STUDIES IN PARTIAL FULFILLMENT OF THE REQUIREMENTS FOR THE DEGREE OF

MASTER OF SCIENCE

GRADUATE PROGRAM IN EARTH AND SPACE SCIENCE

YORK UNIVERSITY

TORONTO, ONTARIO, CANADA

OCTOBER 2024

ABSTRACT

Gravity gradients have not been globally measured since 2013. Accordingly, we advance GRACE gradiometer mode (GM) to enable GRACE, GRACE-FO, and future gravity missions to be used in a gravity gradient mode. The benefit for the geosciences is that gravity and gravity gradients contain complementary information about Earth's structure. Based on the seminal contribution from Peidou (2020), we develop a novel configuration for GM that views any single gravimeter satellite as a 'gradiometer'. The new GRACE-C 'gradiometer' gradients more clearly delineate global tectonic plate boundaries in the Himalayas and North Africa regions, the Aleutian trench, the Java trench, and the Peru-Chile trench. Over Canada, the effect of glacial isostatic adjustment is apparent. We also observe signals resembling terrestrial water storage changes in Africa, among others. Overall, we highlight the usefulness of GM gradients for a wide variety of geoscience applications. We then develop a software package to produce GM gradients.

DEDICATION

For my family.

‘What I am able to defend is an old idea, that of measurement…’ – Jannis Kounellis

ACKNOWLEDGMENTS

First and foremost, I am most grateful to my supervisor, Professor Pagiatakis. His relentless commitment to mentorship, discovery, and perseverance has been invaluable for me as his student. My time with Professor Pagiatakis has inspired me with desire to undertake challenging pursuits, and the confidence needed for determination.

A special thanks to Professor Mike Daly, it has been a pleasure. Thank you for our discussions and providing feedback. Marica Gaynor, thank you for organizing my teaching and research assistantships. I am very indebted to the department of Earth and Space Science for financial assistance, and it was a privilege to perform my teaching duties and gain this experience.

Alice and Myrto, thank you so much for so many conversations and ideas. I am extremely grateful for all the time spent working together, the many lab meetings, and our friendship. In particular, Myrto, I thank you for providing so much guidance over the years. Diego, my friend, thank you very much for our inspirited debates and discussions on many aspects of science over the years.

This research was supported by Natural Sciences and Engineering Research Council of Canada (NSERC Discovery Grant), held by Professor Pagiatakis.

CO-AUTHORSHIP

The thesis titled ‘Advancements in the GRACE and GRACE-FO Gradiometer Mode’ is based on the research efforts of the author, Nikeet Pandit. Parts of this thesis are excerpts of the original research article, ‘Advancements in the GRACE and GRACE-FO Gradiometer Mode’, submitted to American Geophysical Union’s (AGU) Earth and Space science. The manuscript is co-authored by Dr. Spiros Pagiatakis.

Contributor Role Taxonomy (CRediT) author statement:

Nikeet Pandit: Methodology, Software, Validation, Formal Analysis, Investigation, Writing – Original Draft, Visualization. Spiros Pagiatakis: Conceptualization, Writing – Review and Editing, Supervision, Funding Acquisition

TABLE OF CONTENTS

LIST OF TABLES

LIST OF FIGURES

LIST OF ABBREVIATIONS

AF - Accelerometer Frame

A/D - Analog-to-digital

AOCS - Attitude and orbit control

CHAMP - Challenging Minisatellite Payload

CRediT - Contributor Role Taxonomy

CoM - Centre of Mass

CRF - Celestial Reference Frame

CWT - Continuous Wavelet Transform

DLR - German Space Agency

DM - Differential Mode

DS - Dual-Satellite

DWT - Discrete Wavelet Transform

D/o - Degree/order

ECI - Earth-Centered Inertial

EGG - Electrostatic gravity gradiometer

EFRF - Earth Fixed Reference Frame

EO - Earth Observation

ESDS - Earth Science Data System

ESA - European Space Agency

FWT - Fast Wavelet Transform

GCRF - Geocentric Celestial Reference Frame

GFZ - German Research Centre for Geosciences

GGMT - GRACE and GRACE-FO Gradiometer Mode Toolkit

GGT - Gravitational Gradient Tensor

GM - Gradiometer Mode

GNSS - Global Navigation Satellite System

GOCE - Gravity Field and Steady-State Ocean Explorer

GIA - Glacial Isostatic Adjustment

GCRF - Geocentric Celestial Reference Frame

GPS - Global Position System

GRACE - Gravity Recovery and Climate Experiment

GRACE-FO - GRACE-Follow On

GRF - Gradiometer Reference Frame

ICRS - International Celestial Reference System

IERS - International Earth Rotation Systems Service

IRF - Inertial Reference Frame

ITRF - International Terrestrial Reference Frame

J2000 - Terrestrial Time on January 1, 2000

JERF - J2000 Equatorial Reference Frame

JPL - Jet Propulsion Laboratory

KBR - K-band intersatellite ranging

LEO - Low-Earth Orbit

LOS - Line-of-sight

LRI - Laser ranging interferometer

LRR - Laser Retro Reflectors

LS - Least-Squares

LTI - Linear time invariant

MBW - Measurement Bandwidth

MAGIC - Mass Change and Geosciences International Constellation

MRA - Multi -resolution analysis

N-S - North-South

NASA - National Aeronautics and Space Administration

OBC - Onboard-computer

ONERA - Office National D'études et de Recherches Aérospatiales

POD - Precise Orbit Determination

PO.DAAC - Physical Oceanography Distributed Active Archive Center

REC - Receiver

SF - Satellite Frame

SH - Spherical Harmonic

SST - Satellite-to-satellite

SRF - Science (instrument) reference frame

SRP - Solar Radiation Pressure

SS - Single-Satellite

TIRF - Terrestrial Intermediate Reference Frame

TWS - Terrestrial Water Storage

UTCSR - University of Texas for Space Research

LIST OF SYMBOLS

$\boldsymbol{a}_d$ - Vector of differential mode acceleration

$\boldsymbol{a}_{cal}$ - Vector calibrated linear accelerations

$\boldsymbol{a}_{obs}$ - Vector measured linear accelerations

B - Accelerometer bias vector

$\delta(t)$ - Unit-impulse function

f_c - Corner frequency

G - Gravitational constant

h - Impulse response function

m - Meters

M - Spherically distributed Earth mass

P - Perturbation potential

ψ - Mother wavelet function

$\boldsymbol{Q}$ - Quaternion (q0, q1, q2, q3)

r - Radial distance between satellite and Earth centre of mass

r - Position vector of the satellite

$\mathbb{R}$ - Real number space

R - Rotation matrix

$\boldsymbol{r}_d$ - Vector of differential mode positions

s - Seconds

$\boldsymbol{S}$ - Accelerometer calibration scaling matrix

σ - Standard deviation

t - Time

$\boldsymbol{\Upsilon}$ - Gravitational gradient tensor

V_{ij} - The 2nd derivative of the gravitational potential along the directions *i* and *j*

$X(f)$ - Frequency domain input signal

$y(t)$ - Time domain output signal

1 Introduction

1.1 Background

Continuous observation of global mass distribution and its movement about the Earth is essential for climate study and prediction (Kornfeld et al., 2019). Further, mass resolve of the Earth provides one of the most important insights for exploration geophysics[1] since the Earth cannot be probed directly (Telford, 1976). Gravitation is the attractive force between masses and so, the Earth gravity field[2], related functionals[3], and products serve as a key input in oceanography, hydrology, cryosphere, and solid Earth sciences (Wouters et al., 2014). In general, the gravity functionals can be used to determine how the Earth mass distribution structure varies with respect to a reference, typically the Earth ellipsoid[4]. Changes in the functionals through space and time can signify mass-transfer events (movement of mass), due to e.g., water cycle changes that happen on monthly time scales (Bonsor et al., 2018).

Gravity field measurements may be taken on the Earth topography or in space using artificial satellites. The satellite orbit perturbations are observable as the sum of gravitational and non-gravitational accelerations acting on the satellite. The orbit states (position and velocity) are estimated from the on-board Global Positioning System (GPS) geodetic receiver measurements, using precise orbit determination (POD) methodologies, whereas the non-gravitational accelerations can be measured directly by the on-board 3D accelerometer.

The gravitational accelerations relate primarily to the Earth's gravitational field and its time variability. In addition to the irregularly distributed and time-changing Earth mass (including the Earth atmosphere), additional gravitational accelerations of the satellite stem from, for instance, tidal effects due to gravitational gradients (Vaníček & Krakiwsky, 1986; Hofmann-Wellenhof &

[1] Measurements that pertain to properties of the Earth subsurface.
[2] The gravity field model includes the gravitational field and the centrifugal potential model, while the gravitational model contains the gravitational field model only (Poutanen & Rózsa, 2020). Often the terms are used interchangeably.
[3] Functionals are derived from measurements. So, any quantity that is derived (through a function or a model) is called a functional. Examples of gravity functionals are gravity anomalies, gravity gradients, geoid, etc.
[4] The ellipsoid best fits (in the least-squares (LS) sense) the global Earth mean sea level (Hofmann-Wellenhof & Moritz, 2005).

Moritz, 2005) between, e.g., the Earth and Moon, and other perturbations, such as relativistic effects due to the very-high satellite velocities (Wu et al., 2023). Such gravitational accelerations must be subtracted from the total acceleration of the satellite (via dynamic models) if the gravitational field of the Earth is to be determined.

Further, the non-gravitational perturbations, the most significant to low-Earth orbiting (LEO) satellites are atmospheric drag and solar radiation pressure (SRP), as well as thermal effects (Wang et al., 2023), must be subtracted from the total accelerations to determine the variable gravitational field of the Earth. Whereas the non-gravitational accelerations can be estimated using physical models, they can also be measured accurately by and on-board accelerometer. The non-gravitational accelerations on the artificial satellites measured by a 3D accelerometer also provide essential information for investigating upper atmosphere dynamics (Ince & Pagiatakis, 2017; Peidou & Pagiatakis, 2019; Tzamali & Pagiatakis, 2023).

Observing gravity on the Earth topography provides very high-resolution information, since the Earth gravitational attraction signal attenuates inversely proportional to the square of the altitude because of Newton's law of gravitation. Even so, artificial satellites have unveiled the true potential of measuring orbital perturbations (via on-board precise GPS positioning) in combination with non-gravitational acceleration measurements (via an on-board 3D accelerometer) for the purpose of investigating the dynamic Earth system. Indeed, it is not feasible to observe the time-variable global gravity field without the use of artificial satellites.

To efficiently capture global coverage and homogenous datasets of similar resolution, near-polar and near-circular orbits are used. The altitude of the satellite trajectory acts as a low-pass filter to the high-resolution details and so, the gravitational field does not change very much in-response to short-wavelength Earth structure anomalies when sensed from space. Therefore, it is necessary to fly satellites in very low-Earth orbits despite the increasing atmospheric drag perturbations (Tzamali & Pagiatakis, 2023).

It is also possible to measure the gravitational acceleration gradient field, i.e., the first derivatives of the gravitational field (Rummel et al., 2011), using an on-board gradiometer. Gravitational gradients are more sensitive to changes in the short-wavelength Earth structure anomalies (Zhou & Wu, 2015), and do not significantly attenuate with altitude (Keller & Sharifi, 2005; Peidou &

Pagiatakis, 2019). This is because the spectral properties of a gradient operator are those of a high-pass filter, which counteracts the low-pass filter of altitude. Still, altitude is more effective at attenuating short-wavelength signals than long-wavelength signals (Martinec, 2014), and long-wavelength signals reflect deeper Earth density variations (Garland, 1977; Smithson et al., 1979; Vaníček & Krakiwsky, 1986).

1.2 Motivation

For addressing global Earth dynamics, the German Research Centre for Geosciences (GFZ) launched the first dedicated gravity space mission, namely the Challenging Minisatellite Payload (CHAMP) in 2000. After, GFZ, in collaboration with National Aeronautics and Space Administration's (NASA) Jet Propulsion Laboratory (JPL), launched the Gravity Recovery and Climate Experiment (GRACE) mission in 2002. A near-identical follow-on mission (GRACE-FO) was launched in 2018. In 2009, the European Space Agency (ESA) launched a dedicated gravity gradiometry mission for the first time, namely, the Gravity Field and Steady-State Ocean Circulation Explorer (GOCE). Indeed, observing the Earth's parameters from space shares the same age as space exploration itself, as radio signals from Sputnik 1 and 2 determined the Earth's oblateness significantly more accurately than ever before (Flurry, 2017).

The dedicated gravity space missions have been immensely successful, so much so, that they are driving international initiatives, primarily from NASA/JPL, ESA, and the German Space Agency (DLR/GFZ), to continue monitoring the Earth's dynamic gravity field in space and time through designing GRACE-FO's successor constellation – the candidate Mission of Opportunity for ESA–NASA cooperation in the frame of the Mass Change and Geosciences International Constellation (MAGIC), planned to be launched in 2028 (Massotti et al., 2021; Wiese et al., 2022).

The gravity space missions are designed to have continuous observations of the satellites' trajectory to determine the total acceleration, namely the gravitational and non-gravitational accelerations acting on the satellites. CHAMP, GRACE, and GRACE-FO each boast 3-D accelerometers located precisely at the satellite centre of mass (CoM), so that the measured accelerations are proportional to the non-gravitational accelerations acting on the satellite, while they are free from spacecraft rotational accelerations (Bandikova et al., 2019). The difference

between the two reveals information about the Earth gravitational field. In this way, CHAMP and GRACE are gravitational space missions as they ultimately measure the gravitational field.

GOCE was the first gravitational gradiometry mission, measuring the gravitational gradient field (the gravitational acceleration differences). For this purpose, GOCE carried a 3-axis gradiometer that consisted of three pairs of 3D accelerometers, each separated by a 0.5 m baseline, to observe the gravitational difference between each orthogonal pair of accelerometers (ESA, 2008; Rummel et al., 2011). As a result of the very small separation between the accelerometers, GOCE recovered very high-resolution information. This is because the precision of differential accelerometry measurements is inversely proportional to baseline separation (Rummel, 2003; Keller & Sharifi, 2005).

Similarly, GRACE are tandem space missions that consist of 'twin' satellites flying in the same orbit plane, offset by a very-long 220 km baseline (Kornfield et al., 2019). Unlike the GOCE accelerometers which were fixed to a very-short 0.5 m baseline, GRACE intersatellite separation changes are a result of the variable Earth gravitational field that accelerates each leading and trailing GRACE satellite differently. GRACE carries precise intersatellite ranging measurements to continuously measure the line-of-site (LOS) separation, which are used to improve the resolution of GRACE gravitational field solutions (Ghobadi-Far et al., 2020). Conceptually, the tandem configuration of GRACE may be viewed as a one-axis gradiometer along the (220 km) baseline (Seeber, 2003). Accordingly, Keller & Sharifi (2005) first explored the idea of estimating the gravitational gradient along the line-of-sight (LOS) separating the GRACE satellites. However, it did not work, primarily because (among other factors) of the very-long baseline separation between the two satellites (Casotto & Fantino, 2007; Peidou & Pagiatakis, 2019). Further, this method only would function as a one-axis gradiometer, thereby missing the other two components to fully populate the gravitational gradient tensor (GGT).

In general, CHAMP, a single-satellite (SS) mission, recovered low-frequency details; GRACE, which can be viewed as a 'CHAMP-like' tandem mission that has precise intersatellite ranging measurements, recovers medium-frequency details; while GOCE, primarily due to the much shorter-baselines of the on-board accelerometers, recovered high-frequency details (Johannessen, 1999). Clearly, the combination of 3-D tracking and accelerometry on board the Challenging

Minisatellite Payload (CHAMP), Gravity Recovery and Climate Experiment (GRACE), Gravity Field and Steady-State Ocean Circulation Explorer (GOCE) and the planned follow-on missions has and will continue to revolutionize the monitoring of our ever-changing planet and its climate.

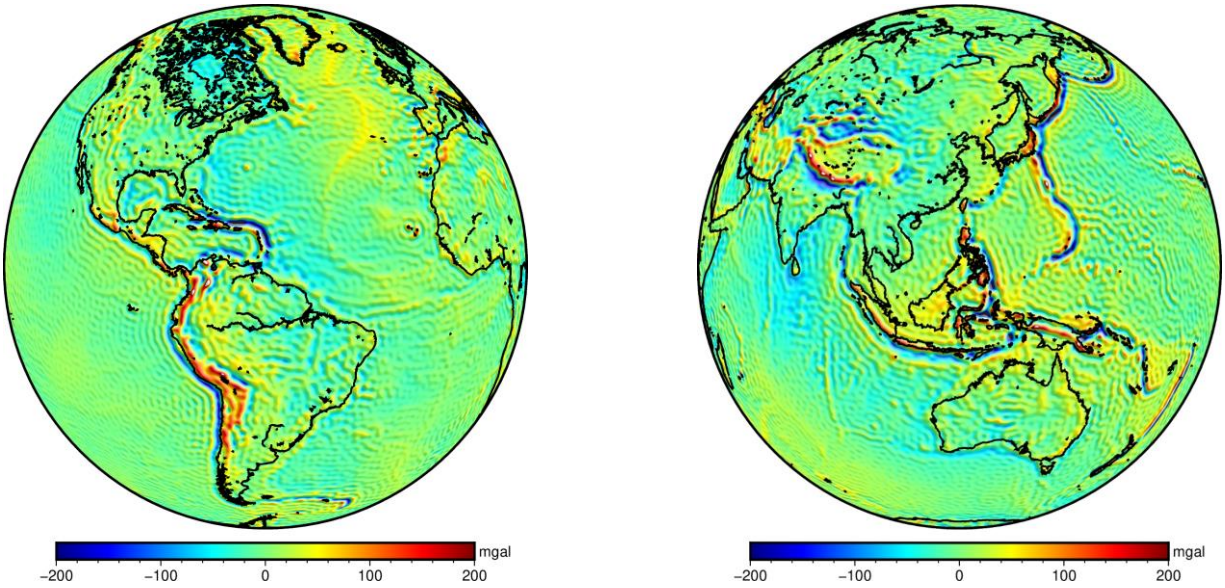

Figure 1: GRACE-FO GGM05G gravity field anomalies retrieved from the International Centre for Global Earth Models (ICGEM) and plotted in Generic Mapping Tools (GMT).

Even so, realizing the potential of the data produced by Earth observation (EO) gravity space missions is challenging (Borgeaud et al., 2015), if not impossible, creating a myriad of research opportunities to discover new important information from GRACE, even as they orbit in space. GRACE measurements do not generally provide a direct observation of the Earth's geodynamic parameters of interest. Therefore, is necessary to translate 'raw measurements' into applicable and tailored 'data products' that satisfy the requirements for specific geoscience applications, such as profiling the upper atmosphere with radio occultation (RO) techniques (Beyerle, 2005), or mapping subsurface terrestrial water storage (TWS) changes (Bonsor et al., 2018; Fatolazadeh & Goïta, 2021).

Overall, mass change determination is one of the five highest-priority parameters to advance Earth systems sciences over the next decade (National Academies, 2018). The expansive scientific and societal value that the dedicated gravity missions provide is clear, as they provide information that directly informs policymaking. For instance, in the recent Intergovernmental Panel on Climate Change 2022 report, GRACE-FO was the third most cited space mission (GFZ, 2022).

1.3 Research objectives

The core objective this thesis is to discover important and new geophysical information from GRACE by advancing the concept of GRACE and GRACE-FO gradiometer mode (GM). In this pursuit, we translate GRACE and GRACE-FO satellite measurements into data products that provide novel geophysical information, not currently offered by any other institution. Further, we develop an open-sourced and user-friendly software package that can produce our data products to be used by geophysicists and other scientists for exploring the Earth dynamic system.

The global gravitational gradient field has not been observed since the decommission of GOCE in 2013. Based on the foundational work of Peidou and Pagiatakis (2019), our objective for this thesis is to advance the concept of GRACE gradiometer mode (GM) for the purpose of using GRACE, GRACE-FO, and future single-, dual-, or satellite constellation gravity space missions as 'gradiometer missions', even though the missions have not, or may not carry a gradiometer in their payload.

GRACE has never carried a gradiometer, it is only the concept of GM introduced by Peidou & Pagiatakis (2019) which creates a fictitious 3-axis gradiometer system very similar to GOCE, only the GRACE 'gradiometers' have longer and variable baselines, an unprecedented paradigm for space-based gravitational gradiometry. In GM, we first move (fictitiously) the trailing GRACE satellite to be as close as possible to the 'fixed' leading satellite. To determine the closest approach of the satellites, we use POD solutions for each satellite trajectory. At the closest approach of the twin GRACE satellites (a few to hundreds of metres), the non-gravitational perturbations on each satellite are considered the same, except we find each satellite attitude is not perfectly aligned due to the gravitational gradients.

The satellite attitude is a function of non-gravitational perturbations and gravitational gradients (Gerlach, 1965; Peidou & Pagiatakis, 2019). By reciprocity (Peidou & Pagiatakis, 2019), when we align the satellite attitudes to a common reference, we can insert gravitational gradients which caused the attitude misalignments. We then use the non-gravitational accelerations, observed by the time-shifted trailing and leading satellite accelerometers, to minimize or remove the common non-gravitational accelerations on each satellite at closest approach. Finally, we estimate

gravitational gradients from the differential accelerations in a common reference frame, usually one of the leading satellites, also incorporating the 3D distance separation between the satellites at closest approach.

Peidou and Pagiatakis (2019) used GM to derive gravitational gradients and explore geodynamically active regions around the globe. They demonstrated the similarities of the GRACE-GM gradients to those observed by the GOCE gradiometer. They also showed that GRACE-GM gradients contain geophysical signals in a wider bandwidth, compared to GOCE, as a result of the variable GM 'gradiometer' baselines separating the satellites. We herein refer to the configuration of the GM, which uses two satellites in unison as a 'gradiometer', as *dual-satellite gradiometer mode* (DS-GM). It is very important to emphasize that in order to achieve the shortest distance between the two satellites, when their speed is on average 7.6 km/s, Peidou & Pagiatakis (2019) interpolated the available data, namely POD (0.2 Hz), accelerometer measurements (1 Hz) and attitude information (0.2 Hz) to 10 Hz sampling frequency using cubic splines.

1.4 Original research contributions

In this thesis, we focus on applying the GM concept to GRACE-FO for the first time. The trailing GRACE-FO satellite (GRACE-D) accelerometer was powered down in 2018 due to systematic errors (Harvey et al., 2022). Since non-gravitational accelerations measured by the leading and trailing GRACE satellites are necessary for the DS-GM, we successfully implement in this thesis a simpler configuration of GM that views only one GRACE satellite as the 'gradiometer'. In doing so, we can achieve GRACE-FO gradiometry using the accelerometer measurements from the operational GRACE-C satellite, taking advantage of the available high sampling frequency of 10 Hz. The required GRACE-C positions and satellite attitude are then interpolated to the GPS time-tags of the 10 Hz accelerations. We call this new configuration *single-satellite gradiometer mode* (SS-GM).

Like Peidou & Pagiatakis (2019), we investigate the geodynamics of active regions around the globe and further demonstrate the ability of GRACE and GRACE-FO 'gradiometers' to depict useful geophysical information. We compare GM configurations using one (SS-GM) and two (DS-GM) GRACE and GRACE-FO satellites. Our investigations result in the discovery of the benefits

of our novel SS-GM approach compared to DS-GM, which are further enhanced by GRACE-C improvements in data quality and satellite design. The SS-GM and DS-GM should produce nearly identical results, when the only one fundamental assumption of DS-GM is that the 'twin' satellites are identical (Peidou & Pagiatakis, 2019). In practice, the satellites and payload are not identical, except this is evidently achieved in SS-GM since only one satellite is used. Furthermore, we find that the SS-GM 'gradiometer' average baseline separation magnitude is about 230 times shorter than in DS-GM configuration. This should yield higher resolution gradients, since the precision of gradiometers is inversely proportional to baseline separation (Rummel, 2003; Keller & Sharifi, 2005).

In applications, the benefits of GRACE-C SS-GM are evident, resulting in more robust[5] gradient solutions that depict more useful[6] geophysical information than DS-GM. In GOCE global gradient solutions, it was very clear that the solutions delineate global plate boundaries and subduction zones (Panet et al., 2014). In SS-GM, we also observe that our gradients delineate tectonic plate boundaries and subduction zones in the Himalayas and North Africa regions, the Aleutian trench, the Java trench, and the Peru-Chile trench. This is a significant discovery of SS-GM that further proves that gradiometry using GRACE, or similar dedicated gravity space missions, produces meaningful geophysical information. Further, we demonstrate that the GRACE and GRACE-FO 'gradiometers' probe deeper into the Earth than the GOCE gradiometer, reflecting very-deep Earth structure anomalies, using a multi-resolution analysis (MRA).

Over Canada, we see that the effect of glacial isostatic adjustment (GIA) is apparent. In Africa, we observe well-known signals resembling terrestrial water storage (TWS) changes, among other global signals. Indeed, like the TWS anomalies over Africa, we also do not clearly see the GIA signal over Canada in the GOCE gradients. Although the 'gradiometers' show limitations, the GM appears to provide an indicator for accelerometer performance. We show that the SS-GM amplifies the perturbation signal in the gradients, providing an effective configuration for studying field-

[5] Robust solutions are more insensitive to minor changes or perturbations in the input.
[6] Useful in this context means that they compare more favourably with the global characteristics of the Earth structure.

aligned currents (FACs), attitude thruster activations, and accelerometer measurement ‘jumps’ (Tzamali & Pagiatakis, 2023).

We anticipate that the results presented herein will harbour enthusiasm from geophysicists and other scientists to use our new set of tailored data products, derived directly from GRACE and GRACE-FO satellite measurements. These include Level 1, Level 2, and Level 3 GRACE GM data products, namely GGM1B, GGM2B, and GGM3B, respectively. In harmony with the NASA Earth Science Data System commitment to open science, we develop an open-sourced MATLAB software package, named the GRACE and GRACE-FO gradiometer mode toolkit (GGMT).

1.5 Layout of thesis

Chapter 2 presents a description of the mission concepts for GRACE and GOCE, key instrumentation, data products, coordinate systems and their transformations. Chapter 3 provides the methodology for the data processing used in this thesis and then reviews the concept of GRACE dual-satellite gradiometer mode (DS-GM), introduced by Peidou & Pagiatakis (2019). After a review of the GM concept and assumptions, we derive our own estimate for the gravitational gradient tensor (GGT) using GRACE DS-GM and compare the solutions to those observed by the GOCE gradiometer for validation. After the review, we compute GRACE-C and -D DS-GM gradients for the first time, except the GRACE-D accelerometer is non-operational and uses a ‘transplanted’ accelerometer data product from the operational GRACE-C accelerometer.

We find that this does not provide meaningful geophysical information and so, in Chapters 4, we develop the single-satellite GM (SS-GM) configuration and perform investigations of geodynamically active regions around the globe using our GM gradients, demonstrating the benefits of the new approach. In Chapter 5, we use a multi-resolution analysis (MRA) to assess the GOCE and GRACE-C SS-GM gradients, showing the benefits of the variable baseline GM ‘gradiometers’, compared to GOCE. In the next section of Chapter 5, we explore the perturbations affecting GRACE accelerometers using GM, showing how GM gradients can provide an indicator for accelerometer performance. In Chapter 6, we provide a software manual overview for the GRACE and GRACE-FO Gradiometer Mode Toolkit – GGMT (the complete manual is in Appendix A). Finally, Chapter 7 concludes our thesis and offers recommendations for future work.

2 GRACE and GOCE Gravity Space Missions

In this chapter, we introduce critical GRACE and GOCE mission concepts for understanding the GRACE and GRACE-FO gradiometer mode (GM). We explain the key objectives of these space missions, including the instrumentation, data products used in this thesis, and coordinate reference frames. The later is an especially pertinent concept, since the validity of GM for estimating gradients using GRACE is based on correct transformations between the relevant reference frames.

2.1 Mission concepts

The gravitational potential at the altitude of an artificial satellite orbiting the Earth is given by $V = -\frac{GM}{r} + P$, where G is the gravitational constant, M is the Earth mass, r is the radial distance between the satellite and Earth centre of mass (CoM), and P is the perturbation potential (Hu, 2015). The gradient operator is a vector of partial derivatives in $\mathbb{R}^3$, and the gravitational acceleration is the gradient of V. The Keplerian laws of orbital motion perfectly describe the states of the satellite orbit trajectory (position and velocity), when the perturbation potential is zero (Vaníček & Krakiwsky, 1986; Hu, 2015). The perturbing potential is very small. Specifically, it is only of magnitude 10^{-3} of the radial term (Vaníček & Krakiwsky, 1986). When we express the gravitational potential in terms of the radial term and perturbation potential, the second term absorbs the effects of higher-order Earth mass density anomalies, tidal, relativistic, and other non-gravitational perturbations on the satellite trajectory. Consequently, it is the deviations from the Keplerian orbit that allow us to infer the important geophysical information for the Earth (including the Earth atmosphere), such as the Earth gravitational field, using artificial satellites.

The primary objective of GRACE is to generate static and dynamic gravity field models[7] to spatial scales of 200 km and 300 km, respectively (Kornfeld et al., 2019). Based on the success of the initial GRACE mission, a near-identical follow-on (GRACE-FO) mission was launched in 2018

[7] The division between static (long-term models) and dynamic (time-variable) gravity models introduces an unavoidable time-space trade-off. Specifically, there is a limitation in obtaining high-resolution information in both space and time, simultaneously. We expand on this concept in Section 3.2.

(Kornfield et al., 2019). The primary objective of GOCE, decommissioned in 2013, was to generate static gravity field models to spatial resolution better than 100 km (Rummel et al., 2011). To support climate and Earth science objectives, these gravity space missions were designed to provide global coverage, using near-polar and near-circular orbits. GOCE and GRACE flew at initial orbit altitudes of approximately 250 km and 500 km, respectively. The satellite trajectory is estimated from the on-board Global Positioning System (GPS) geodetic receiver measurements, using precise orbit determination (POD) methodologies. The GRACE and GOCE satellite attitude, or more precisely, the orientation of the science/instrument reference frame (SRF) with respect to the Terrestrial Intermediate Reference Frame – TIRF (Luzum & Petit, v. 1.3.0., 2019) (formally GCRF-intermediate, also known as CRF, ECI and IRF in GRACE/GOCE literature), is observed by star cameras (ESA, 2008; Wen et al., 2019). The definitions of these reference frames and their transformations are described in the sequel.

Figure 2: GRACE-FO being built. Image credit: Airbus DS GmbH/A. Ruttloff

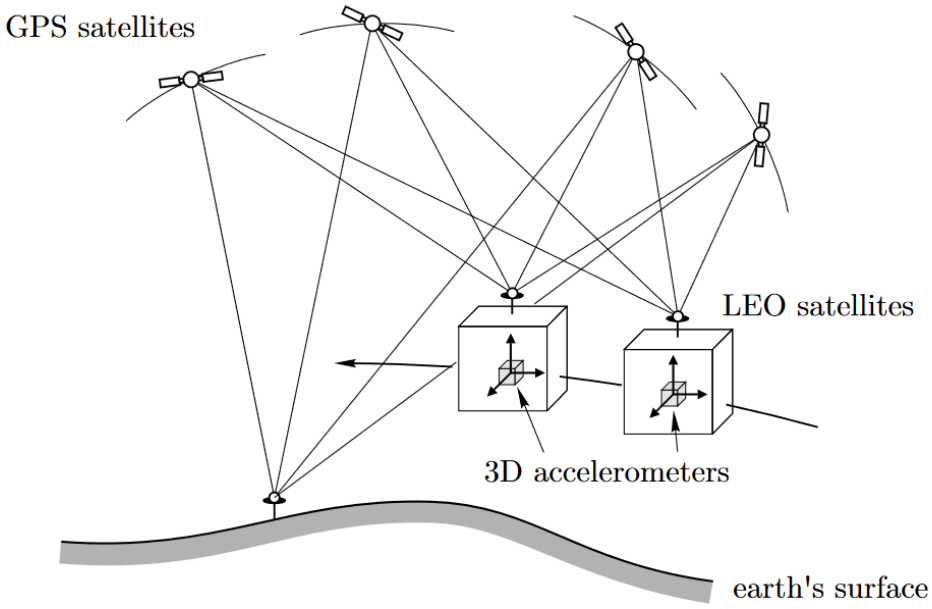

Figure 3: GRACE mission operating principle (Hofmann-Wellenhof & Moritz, 2005). The satellite trajectory is estimated using GPS receivers on each satellite. The K-band ranging (KBR) instrument is used for very precise intersatellite ranging. Each satellite carries a 3D accelerometer, situated at the satellite centre of mass (CoM), to measure the non-gravitational accelerations on the spacecraft.

To observe the temporal variations of the gravitational field, the GRACE primary payload includes the precise micrometer K-band intersatellite ranging (KBR) instrument that performs satellite-to-satellite tracking (SST) in a 'low-low' mode. The near-identical GRACE satellites fly in tandem, separated by ~220 km (Hofmann-Wellenhof & Moritz, 2005). For GRACE, the leading and trailing satellites are referred to as A and B, respectively. For GRACE-FO, they are C and D.

Intersatellite separation changes between the leading and trailing satellites are partially due to variations in the Earth gravitational field. For instance, when the twin satellites fly towards a gravitational field anomaly, due to, e.g., a mountain range, the leading satellite accelerates towards the mountain range first, thus increasing the intersatellite distance since the trailing satellite is still too far to experience the same acceleration. The intersatellite distance will then decrease once the leading satellite passes the mountain range and the trailing satellite approaches it. This results in a continuous change of the intersatellite separation, as the twin satellites encounter mass density variations at different times. Misfelt (2019) provided an excellent Figure showing the changes in the inter-satellite spacecraft distance while flying over the Himalayas (ibid., 2019; Figure 3.2).

In addition to the KBR, GRACE-FO carries a laser ranging interferometer (LRI), a technology demonstration for future gravity missions, that uses a laser to measure the inter-satellite distance. The LRI has been shown to significantly outperform the KBR in terms of precision (Abich et al., 2019), and because of its outstanding success, it is currently being adopted to serve as the primary instrument in the next generation of gravity missions, such as Mass Change and Geosciences International Constellation (MAGIC) (Misfeldt et al., 2023). The spatial resolution of the temporal gravity field models has been improved by the incorporation of the KBR measurements, and they have been improved further by one order of magnitude with the incorporation of the LRI (Ghobadi-Far et al., 2020).

The Earth gravity field solutions are recovered from GRACE-FO by combining KBR, LRI, and POD solutions. The estimation process usually incorporates other sources of a-priori (previously known) information, such as models for ocean tides, gravitational perturbations due to the other planets in the solar system, etc. to remove systematic effects from the measurements to obtain an ideally 'pure' Earth gravitational field signal (Flurry, 2017; Save 2019). However, errors in both the models and measurements carry forward and result in uncertainty in the final solution (Taylor & Thompson, 1982; Wöske et al. 2019). Therefore, it is not possible to recover an error-free gravity field solution.

To isolate the contributions of the gravitational field anomalies in the LRI, KBR, and POD solutions, the contribution of the non-gravitational perturbations in the solutions must be removed in a common reference frame, based on observations from the 3D accelerometer in the science reference frame (SRF; to be defined below) (Flurry, 2017). Accordingly, the quality of gravity field models depends significantly on the quality of the measurements of the non-gravitational accelerations (Harvey et al., 2022), as well as on the precision of the reference frame transformations. The GRACE-FO accelerometers are very similar to the one flown on GRACE, only with minor engineering improvements (Kornfeld et al., 2019).

The accelerometers, namely the SuperSTAR accelerometers, were both designed by the French Aerospace Lab of the Office national d'études et de recherches aérospatiales (ONERA), the French national aerospace research centre. The accelerometer comprises an electrostatic proof mass suspended inside of an electrostatic cubic cage, situated at the satellite centre of mass (CoM). The

acceleration measurements are the voltages applied to the electrodes, to ensure that the proof mass stays motionless with respect to the cage (Bandikova et al., 2019). The accelerometers are located at the satellite CoM to reduce or eliminate angular accelerations, and the measured accelerations (i.e., control voltages) are proportional to the non-gravitational forces acting on the satellite.

Since gravitational perturbations accelerate the electrostatic cage and proof mass by the same amount simultaneously, there is no relative motion of the proof mass with respect to the cage (and by extension to the spacecraft) and therefore they are not observed. Since the CoM is only estimated by indirect means (the 'true' CoM is never exactly known, only estimated), the accelerometer may measure residual rotational accelerations, albeit in practice they are negligible. The accelerometer calibration factors and biases need to be regularly estimated and are usually estimated prior to, or simultaneously with, the gravity field solutions to convert the accelerometer control voltages to acceleration units $[m/s^2]$.

The GOCE mission primary payload was a 3-axis electrostatic gravity gradiometer (EGG), designed to capture the short-wavelength gravitational signal (ESA, 2008). In fact, the tandem configuration of GRACE may conceptually be viewed as a one-axis gradiometer with a very-long (220 km) baseline (Seeber, 2003). Although the twin satellite configuration with low-low satellite-to-satellite tracking recovers higher resolution details of the gravitational field compared to Challenging Minisatellite Payload – CHAMP, the GOCE EGG recovered even higher-frequency details, since measurement precision of gradiometers are inversely proportional to the baseline separation (Rummel, 2003; Keller & Sharifi, 2005).

The GOCE electrostatic gravity gradiometer (EGG) consisted of three pairs of 3-axis accelerometers to estimate the full gravitational gradient tensor (GGT). The three pairs of 3-axis accelerometers were each separated by a 0.5 m baseline in order to observe the gravitational difference between each orthogonal pair (ESA, 2008; Rummel et al., 2011). The GOCE accelerometers in each pair operated in a similar servo-controlled mechanism to the GRACE SuperSTAR accelerometers. GOCE was the first gravitational gradiometry space mission. Gravitational gradiometry is a measure of the second derivatives of the gravitational potential (Freeden et al., 2010) and the gravitational gradient tensor $\boldsymbol{\Upsilon}$ (GGT) is defined as:

$$\Upsilon = V_{ij} = \begin{bmatrix} V_{xx} & V_{xy} & V_{xz} \\ V_{yx} & V_{yy} & V_{yz} \\ V_{zx} & V_{zy} & V_{zz} \end{bmatrix} = \begin{bmatrix} \frac{\partial^2 V}{\partial x^2} & \frac{\partial^2 V}{\partial x \partial y} & \frac{\partial^2 V}{\partial x \partial z} \\ \frac{\partial^2 V}{\partial y \partial x} & \frac{\partial^2 V}{\partial y^2} & \frac{\partial^2 V}{\partial y \partial z} \\ \frac{\partial^2 V}{\partial z \partial x} & \frac{\partial^2 V}{\partial z \partial y} & \frac{\partial^2 V}{\partial z^2} \end{bmatrix}, \quad (2.1)$$

where V_{ij} denotes the 2nd derivative of the gravitational potential along the directions *i* and *j*.

The GOCE accelerometers were not located in the GOCE CoM, and therefore the accelerometers observed the rotational accelerations of the spacecraft, in addition to non-gravitational accelerations. Indeed, the GOCE EGG was based on the concept of differential accelerometery (Rummel et al., 2011), and therefore minimized the non-gravitational accelerations by the subtraction of accelerations at each accelerometer pair, as the non-gravitational perturbations on each accelerometer were approximately the same when separated by the short 0.5 m baseline. The residual non-gravitational perturbations were minimized by the 'drag-free' GOCE spacecraft bus, a necessary development, since air drag for low-Earth orbiting satellites is the primary perturbation in the along-track direction (Bandikova et al., 2019; Tzamali & Pagiatakis, 2023). In addition to the satellite design, the orbit selection, namely a sun-synchronous dusk-dawn orbit, helped isolate the gravitational perturbation signal, since the orbit minimizes thermal gradient perturbations (ESA, 2008).

The gravitational gradients contain complementary information to gravitation and are used directly in the study of postglacial rebound (Bouman et al., 2016; Métivier et al., 2016), mass density distribution of the upper mantle (Bouman et al., 2015; Fullea et al., 2015), and near-surface geological structures (Martinec, 2014). GOCE gravitational gradients referenced to GOCE's 250 km altitude have been shown to be sensitive to the mass density distribution of the upper mantle (Bouman et al., 2015; Fullea et al., 2015), while GOCE gradients downward continued to the Earth's surface have been used to investigate near-surface geological structures (Martinec, 2014). GRACE, which observes the gravitational field at 500 km, accordingly, allows very-deep Earth probing, e.g., GRACE measurements have been used to study the dynamic processes inside the fluid core (Mandea et al., 2012; Mandea et al., 2020).

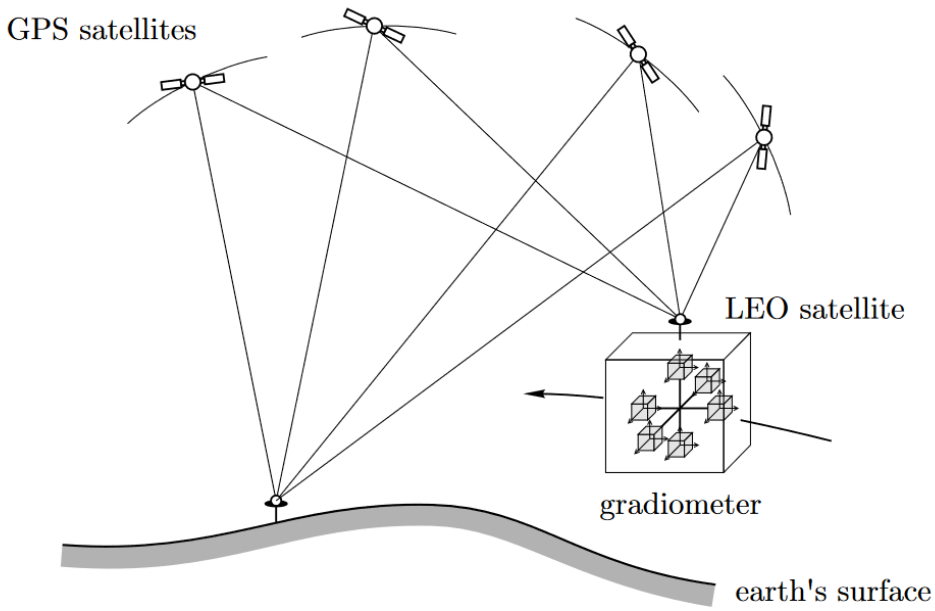

Figure 4: GOCE operating principle (Hofmann-Wellenhof & Moritz, 2005). The satellite trajectory is estimated using GPS receivers on each satellite. The satellite carries a 3-axis gradiometer, i.e., six 3-axis accelerometers, offset from the GOCE CoM, and separated by a 0.5 m baseline, in the orthogonal gradiometer reference frame (GRF).

2.2 Reference frames

The GRACE and GOCE data products we use in this thesis are referenced to different reference systems and frames. The GRACE data products were last retrieved on January 15, 2023 from NASA's Physical Oceanography Distributed Active Archive Center (PO.DAAC) via podaac.jpl.nasa.gov, operated by the Jet Propulsion Laboratory (JPL) in Pasadena, California. The GOCE data products were retrieved from the European Space Agency's Earth Online system via earth.esa.int/eogateway (Jan 15, 2023). Since then, the GRACE and GOCE science teams may have changed the definitions of the reference frames or provided the data in a different reference frame than what is documented here. Therefore, we recommend referring to the data product handbooks and release notes to find the most up-to-date information.

2.2.1 Inertial Reference Frame (IRF)

The GRACE Level 1 data documentation (Case et al., 2010) adopts the nomenclature of 'Inertial (reference) Frame' − IRF to refer to the International Celestial Reference System – ICRS (Luzum

& Petit, 2010). In fact, the frame is not strictly inertial since the coordinate system associated with this frame is geocentric (GC). The GOCE documentation defines the IRF by the J2000 Equatorial Reference Frame (JERF) (ESA, 2008). The realizations of each frame are very similar. The geocentre in the ICRS and JERF is defined as the Earth centre of mass, including the atmosphere and oceans.

According to the International Earth Rotation and Reference Systems Service (IERS), the body responsible for standardizing the Earth reference systems, these frames are currently named Terrestrial Intermediate Reference Frame − TIRF (Luzum & Petit, v. 1.3.0., 2019), although this may change in the future. The frame is formally known as the Geocentric Celestial Reference Frame – intermediate (GCRF) in the latest IERS Conventions 2010 (Luzum & Petit, 2010). Other current popular names are the Celestial Reference Frame (CRF) and Earth-Centered Inertial (ECI) frame. In general, for both GOCE and GRACE, the 'Inertial Frame' is the TIRF.

We choose to adopt the IRF nomenclature in this research to be in harmony with the terminology used by the GRACE and GOCE science teams and relevant literature. The xy-plane of the IRF is kinematically very close to the mean equator of J2000. The x-axis is kinematically fixed to the mean equator and points very close/towards the vernal equinox, i.e., the intersection of celestial equator with the ecliptic, in a direction known as the Celestial Intermediate Origin (CIO). The z-axis is normal to the xy-plane and is fixed to the Conventional Reference Pole – CRP. The CRP is nearly aligned to the Earth spin-axis. The y-axis forms the right-handed triad.

2.2.2 Earth Fixed Reference Frame (EFRF)

The Earth Fixed Reference Frame (EFRF) for GRACE and GOCE is kinematically realized by the International Terrestrial Reference Frame (ITRF). The ITRF is a geocentric equatorial system (Luzum & Petit, 2010). The xy-plane of the ITRF is the mean equatorial plane of the Bureau International de l'Heure (BIH) reference frame orientation of 1984, within 0.005" uncertainty. The x-axis points towards the Terrestrial Intermediate Origin (TIO); that is very close to Greenwich meridian. The z-axis is in the direction of the IERS Reference Pole (IRP), and the y-axis forms the right-handed triad.

2.2.3 GRACE and GRACE-FO

The GRACE SuperSTAR accelerometers measure non-gravitational accelerations acting on the satellite in the science reference frame (SRF), defined in Table 1.

Table 1: Definition of the Science Reference Frame (SRF).

Axis	Description
X_{SRF}	Points to other satellite K-band microwave intersatellite ranging system (KBR) (along-track axis).
Y_{SRF}	Forms right-handed system with X_{SRF} and Z_{SRF} (cross-track axis).
Z_{SRF}	Nadir-pointing.

For GRACE-FO, the Level 1A GRACE-FO accelerometer measurements are provided in the accelerometer frame (AF). The origin of the accelerometer frame (AF) is the CoM of the accelerometer proof mass; that is, within 0.1 mm of the satellite CoM.

The relation to SRF is given by the following:

$$X_{AF} \cong +Y_{SRF}, \tag{2.2}$$

$$Y_{AF} \cong +Z_{SRF},$$

$$Z_{AF} \cong +X_{SRF}.$$

The SCA1B data product provides the quaternions for the purpose of transforming between the IRF and SRF frames. This is needed, e.g., to remove the non-gravitational forces measured by the accelerometer in the POD solutions. To transform the accelerometer measurements provided in the AF to IRF, it is first necessary to translate the AF measurements to SRF before using the rotational quaternions provided in the SCA1B data product.

The rotation matrix corresponding to the quaternions provided in the SCA1B product, which transforms IRF to SRF, is expressed by (Wu et al., 2006):

$$\boldsymbol{R}_{IRF}^{SRF} = \begin{bmatrix} q_0^2 + q_1^2 - q_2^2 - q_3^2 & 2(q_1 q_2 + q_0 q_3) & 2(q_1 q_3 - q_0 q_2) \\ 2(q_1 q_2 - q_0 q_3) & q_0^2 - q_1^2 + q_2^2 - q_3^2 & 2(q_2 q_3 + q_0 q_1) \\ 2(q_1 q_3 + q_0 q_2) & 2(q_2 q_3 - q_0 q_1) & q_0^2 - q_1^2 - q_2^2 + q_3^2 \end{bmatrix}, \quad (2.3)$$

where $\boldsymbol{Q} = q_0 + \boldsymbol{i}q_1 + \boldsymbol{j}q_2 + \boldsymbol{k}q_3$. Vector $\vec{\boldsymbol{r}}_{IRF} = [x\ y\ z]^T$ in the SRF is given by $\vec{\boldsymbol{r}}_{SRF} = \boldsymbol{R}_{IRF}^{SRF}\vec{\boldsymbol{r}}_{IRF}$. The inverse of a quaternion is $\boldsymbol{Q}^{-1} = -q_0 + \boldsymbol{i}q_1 + \boldsymbol{j}q_2 + \boldsymbol{k}q_3$, hence substituting $q_0 = -q_0$ into Eq. (2.3) yields the rotational matrix $\boldsymbol{R}_{SRF}^{IRF}$ to transform $\vec{\boldsymbol{r}}_{SRF}$ to $\vec{\boldsymbol{r}}_{IRF}$.

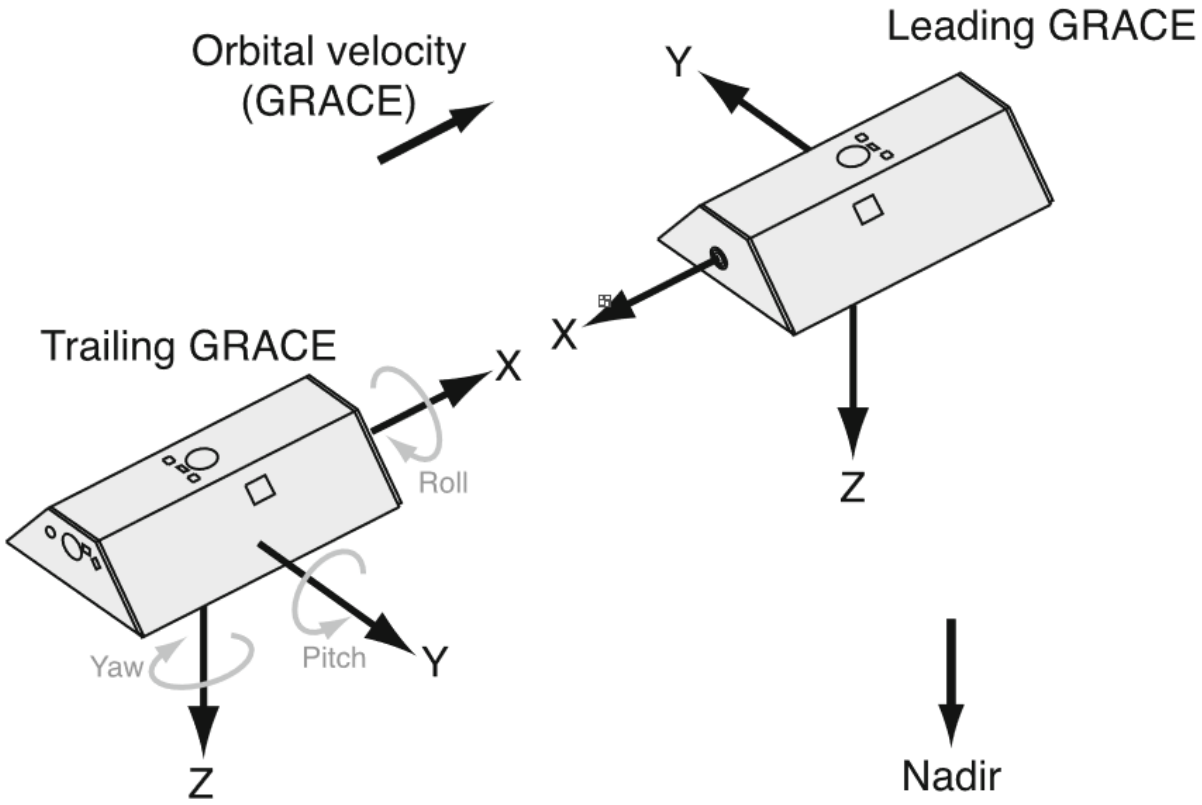

Figure 5: Definition of the spacecraft GRACE and GRACE-FO satellite reference frame (SRF) (Doornbos, 2012).

2.2.4 GOCE

Level 1B GOCE gradiometer measurements are provided in the Gradiometer Reference Frame (GRF). Each axis of the GRF represents a one-axis gradiometer. X_{GRF} is in the along track direction, Z_{GRF} is zenith pointing, and Y_{GRF} completes the right-handed triad. Each accelerometer has its own accelerometer frame (AF) aligned as close as possible with the corresponding GRF axes.

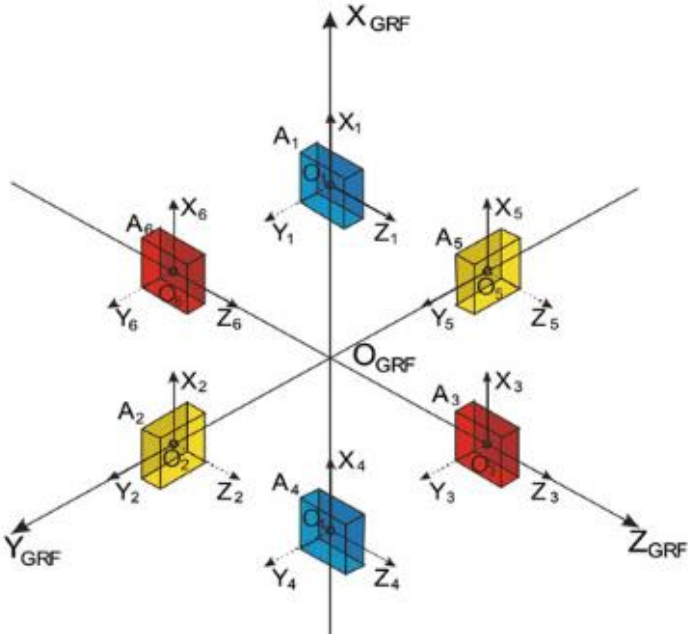

Figure 6: Location of the six accelerometers in the Gradiometer Reference Frame (GRF) (Rummel et al., 2011).

2.3 Data products and instrumentation for GRACE

The GRACE Science Data System oversees GRACE data processing (Case et al., 2010). The Science Data System is a cross-functional team consisting of JPL, the German Research Centre for Geosciences (GFZ), and the University of Texas Center for Space Research (UTCSR). JPL and GFZ derive Level 1 data products from Level 0 data products, while the UTCSR processes the Level 2 data products. Table 2 provides the description of GRACE data processing levels. For GRACE, the Level 1A data products have not released to the scientific community. For GRACE-FO, some Level 1A data products are publicly available. Table 3 and Table 4 outline the GRACE and GRACE-FO data products used in this thesis.

Table 2: GRACE and GRACE-FO data product processing Levels.

Level	**Description**
0	Telemetry data from GRACE satellites in the form of two files (science and housekeeping). Data is downlinked every pass by of the Raw Data Center in Neustrelitz, Germany.

1A	Measurements are converted to engineering units. Reversible.
1B	Level 1A data is time-tag corrected and then compressed. Possibly irreversible.
2	Gravity field solutions and other gravity field functionals.

Table 3: GRACE-A and -B data products used in thesis.

Product	**Description**	**Sampling Rate**	**Frame**
ACC1B	Measured linear accelerations of proof mass.	1Hz	SRF
GNV1B	Position and velocity with associated modelling errors in the Earth Fixed Reference Frame (ITRF). The realization (year) of the frame is not provided in the documentation.	1Hz	ITRF
SCA1B	Rotational quaternions rotating the Inertial Reference Frame (IRF) to Science Reference Frame (SRF).	0.2Hz	--
THR1B	Thruster activation data for attitude and orbit control (AOCS).	--	--

Table 4: GRACE-C and -D (follow-on) data products used in thesis.

Product	**Description**	**Sampling Rate**	**Frame**
ACC1A	Measured linear accelerations of proof mass in onboard-computer time.	10 Hz	AF
ACT1A	Calibrated linear accelerations of proof mass in onboard-computer time.	10Hz	AF
ACT1B	Time-tag corrected and compressed ACT1A data, using a 7^{th} order digital filter with ~35 mHz corner frequency (Wu et., al 2006).	1Hz	SRF
GNV1B	Same as GRACE GNV1B.	1Hz	ITRF 2014
GNI1B	Same as GRACE GNV1B, referenced in IRF.	1Hz	IRF
SCA1B	Same as GRACE SCA1B.	1Hz	--
CLK1B	Clock offsets to convert receiver time to GPS time.	0.1Hz	--

TIM1B	Mappings from onboard computer to receiver time.	0.1Hz	--
THR1B	Same as GRACE THR1B.	--	--

2.3.1 Accelerometer

The GRACE non-gravitational accelerations are observed with a 3-axis SuperSTAR accelerometer. The SuperSTAR instrument characteristics are provided in Table 5. The accelerations provided in the daily data files are not separated to the linear part of the SuperSTAR instrument measurement bandwidth (10^{-4} to 10^{-1} Hz), and therefore must be band-pass filtered. We describe in detail the filtering procedure in Section 3.1.

Table 5: GRACE and GRACE-FO SuperSTAR instrument characteristics.

SuperSTAR Accelerometer		
Accelerometer Axis	X_{SRF}, Z_{SRF}	Y_{SRF}
Sensitivity	$10^{-10}\frac{m}{s^2}/\sqrt{Hz}$	$10^{-9}\frac{m}{s^2}/\sqrt{Hz}$
Measurement Bandwidth	10^{-4} to 10^{-1} Hz	10^{-4} to 10^{-1} Hz

In addition to the non-gravitational accelerations that disturb all low Earth orbiting (LEO) free-fall artificial satellites (e.g., drag or solar radiation pressure – SRP), the accelerometer onboard GRACE also measures disturbances related to the satellite operation, which is important to consider since we use the measured linear accelerations to compute gradients in the GRACE gradiometer mode (GM). For instance, the accelerometer measures disturbances due to attitude and orbit control thruster activations due to satellite design imperfections and misalignments (Bandikova et al., 2019). Although the thrusters are a secondary attitude actuator for GRACE, when any of the magnetorquer rods are parallel to the magnetic field, there is insufficient torque generated from the magnetorquers for attitude control (Bandikova et al., 2019). For this reason, attitude thruster activations are very prominent in the mid-equatorial region and around the poles (**Figure 27**).

The Science Data System suspects that the accelerometer returns spurious measurements during the thruster activations due to analog-to-digital (A/D) aliasing (McCullough et al, 2019). Aliasing occurs (for baseband and real signals – Cumming & Wong, 2005) when a frequency f in a signal $g(x)$ is greater than ½ the sampling rate of $g(x)$ and folds over into the low-frequency spectrum

of the sampled signal $g(x_k)$, creating a false (aka aliased or spurious) peak in the spectrum (Amidror, 2015; Pagiatakis & Peidou, 2021).

To mitigate aliasing effects in the accelerometer measurements due to thrusters, the Science Data System models and replaces the observed measurements with regressed (interpolated) values of the accelerometer responses to the thruster firings. This procedure is only done for the GRACE-C and -D ACT Level 1A and 1B accelerometer data products. The GRACE-C and -D accelerometers each have an individual thruster model for the linear acceleration response due to thruster firings (McCullough et al., 2019). Incorporating the modelled measurements has been shown to improve the quality of the Science Data System gravity field solutions (Bandikova et al., 2019).

In addition to the thruster modelling, after July 6, 2018, the GRACE-D accelerometer was turned off due to systematic errors (Harvey et al., 2022). Since the accelerometer measurements of GRACE-D are necessary for gravity field recovery, the Science Data System 'transplants' the accelerometer dataset from GRACE-C into -D in order to estimate the GRACE-D accelerometer measurements. In Section 3.6 we provide details on the transplant method.

Based on the lessons learned from GRACE-A and -B, there has been two primary engineering changes to improve the quality of the accelerometer measurements of GRACE-C and -D. Firstly, for GRACE-A and -B, the radiation foil on the nadir side of spacecraft body experienced anisotropic vibrations in response to thermal environmental changes, which subsequently 'leaked' into the accelerometer measurements (Kornfeld et al., 2019). These artefacts were named 'twangs' and manifested themselves in accelerometer data as damped oscillations lasting several seconds (Kornfeld et al., 2019). The twangs were significant disturbances to the quality of the accelerometer data, and they contaminated 30% of nadir-pointing (Z_{SRF}) accelerometer data (Gerlach et al., 2005).

To mitigate the twangs, GRACE-C and D use a more rigid attachment of the foils (Kornfeld et al., 2019). Secondly, the GRACE-A and -B accelerometers use a bang-bang feedback controller, a thermal regulation system that rapidly switches between 'on' and 'off' states. The intense heater switching affected nearly 30-40% of the accelerometer data in all 3-axes (Gerlach et al., 2005). The bang-bang control system was replaced with a linear heating controller to reduce these error sources in GRACE-C and -D accelerometer measurements.

Each SuperSTAR accelerometer requires three calibration factors (one for each axis) to accurately relate the control voltages of the instrument to accelerations. For GRACE-C, linear accelerations provided in the Level 1A and 1B ACC1A and ACT1A data products have calibration factors already applied to the measurements. Compared to GRACE-C ACC1A linear accelerations, in the ACT1A linear accelerations, the Science Data System removes and interpolates outlier measurements called 'phantom accelerations', in addition to removing and modelling the accelerometer measurements during the thrusters. The linear accelerations in the GRACE-C ACC1A data product are consequently the same as the ones in the GRACE-C ACT1A data product, except for the modelling and interpolation due to the thrusters and phantom accelerations, respectively. We use this property in Section 4.1 to derive a 'thruster-free' and 'phantom-free' GRACE-C linear acceleration data product when processing the GRACE-C gradiometer mode (GM) gradients. The phantom accelerations are believed to be caused by aliasing during the A/D conversion. The phantom accelerations are of unknown origin and exhibit beta angle correlation[8].

For GRACE-A and -B, the observed linear accelerations provided in the ACC1B data product do not have the accelerometer instrument calibration factors applied. To apply scaling and bias factors to the observed accelerations $\boldsymbol{a}_{obs}$ provided in the GRACE-A and -B ACC1B data product, the equation is given by: $\boldsymbol{a}_{cal} = \boldsymbol{S}\boldsymbol{a}_{obs} + \boldsymbol{B}$, where $\boldsymbol{S}$ is a 3x3 scaling matrix, $\boldsymbol{B}$ is the 3x1 bias vector, and $\boldsymbol{a}_{cal}$ is the calibrated accelerations (Bettadpur, 2009). The specific bias values are modelled within a few percent to the actual value by fitting a quadratic to the daily estimates. To determine the bias at a specific epoch, we use the following:

$$\boldsymbol{B} = c_0 + c_1(T_d - T_0) + c_2(T_d - T_0)^2, \tag{2.4}$$

where T_d is the Modified Julian date, and T_0 is the reference epoch. For dates after March 7, 2003, $T_0 = 52532$ is used and for dates before March 7, 2003, $T_0 = 53736$ is used. The scale factors for GRACE-A and -B, as well as the coefficients (c_0, c_1, c_2) to evaluate the quadratic (Eq. 2.4) are computed by Bettadpur (2009), and are provided in Table 6, Table 7, and Table 8, respectively.

[8] The beta angle is the angle between the satellite orbit plane and the geocentric position vector of the Sun (Tzamali & Pagiatakis, 2023).

Table 6: Recommended accelerometer scales for GRACE-A and -B.

Direction (SRF)	GRACE-A	GRACE-B
X	0.9595	0.9465
Y	0.9797	0.9840
Z	0.9485	0.9303

Table 7: Recommended GRACE-A accelerometer bias coefficients for data after March 7, 2003.

Direction (SRF)	C0	C1	C2
GRACE-A X	-1.2095	-4.128E-5	9.7E-9
GRACE-A Y	29.3370	6.515E-4	-3.9E-7
GRACE-A Z	-0.5606	-2.352E-6	3.8E-9

Table 8: Recommended GRACE-B accelerometer bias coefficients for data after March 7, 2003.

Direction (SRF)	C0	C1	C2
GRACE-B X	-0.6049	-1.982E-5	3.5E-9
GRACE-B Y	10.6860	1.159E-3	-4.3E-7
GRACE-B Z	-0.7901	4.783E-5	-6.5E-9

2.3.2 Timing information

The GRACE-FO ACT1A data product is provided in onboard-computer time (OBC). Since the position, attitude, and thruster information are provided in GPS time, defined as continuous seconds from January 1, 2000, 11:59:47 UTC, we convert the non-gravitational accelerations provided in the onboard-computer time to GPS time to obtain a common time reference with the other data products that we use in the GRACE gradiometer mode (GM). This requires that we first map onboard-computer time to receiver (REC) time using the TIM1B data product. We then add the offsets provided in CLK1B data product to transform receiver to GPS time. The onboard-computer time is referenced to a quartz oscillator on the onboard-computer, while the receiver (REC) time is referenced to an ultra-stable oscillator (USO). The ultra-stable oscillator is used to sample the GPS and K-band ranging system measurements (KBR) (Case et al., 2010). We assume linear clock drifts, as TIM1B and CLK1B are given in 8 s sampling interval, while the ACT1A data product is provided in 10 Hz.

2.3.3 Satellite attitude

The GRACE satellite attitude provided in the SCA1B data product has been optimally estimated through a combination of star camera attitude and angular rate measurements about the SRF (Wen et al., 2019). The star cameras image the stars, and the images are processed by the instrument processing units (IPU) to estimate the attitude. The attitude estimation is performed in the instrument processing units by relating the stars in the images to the 'known' fixed positions of the stars, provided by a star catalogue in a specified frame (Liebe, 1995). The angular rates are estimated using the inertial measurement unit (IMU) measurements.

A Kalman filter is then used to combine all available information (star camera attitude information, angular rates, and instrument noise models), to provide a more robust attitude determination solution, compared to the one achieved by any star camera alone (Wen et al., 2019). Based on the lessons learned from GRACE, the number of star camera heads has been increased from two to three for GRACE-FO, since the arrangement of the three heads ensures at least two camera heads are not 'blinded' by the Sun or the Moon, thus providing a more robust attitude estimate.

2.3.4 Intersatellite ranging

The GRACE-A and -B satellites carried the KBR, while GRACE-FO carries both the KBR and LRI. The instruments send microwave and laser signals between the two satellites, respectively, for the purpose of measuring the line-of-sight (LOS) separation in space and time. The KBR and LRI measure phase changes, plus bias and correction terms which need to be corrected for (Wen et al., 2019). The KBR and LRI biased range data, including the various correction terms, can be found in the KBR1B and LRI1B data products, respectively.

2.3.5 Precise Orbit Determination and GPS

The GRACE geodetic quality receivers can track up to 16 GPS satellites for precise orbit determination (POD), while four channels are mostly used for radio occultation (RO) measurements (Kang et al., 2020). For effective and precise orbit determination using GPS data, it is possible to use only geometric information without incorporating any information on the satellite dynamics (e.g., gravitational field, drag, SRP, etc.) (Li et al., 2017). This is known as the

kinematic method. In the reduced dynamic orbit determination method, the previous known information about the satellite dynamics is optimally weighted with the GPS observations to estimate the satellite orbit trajectory.

Alternatively, it is possible to simultaneously estimate the orbit solution together with the force models. The later method, known as the dynamic POD method, has an advantage since it solves for the orbit, while also updating the previously estimated satellite dynamic information (e.g., SuperSTAR accelerometer calibration parameters), based on the 'innovation' of the new GPS observations. The dynamic POD method is used to estimate the satellite trajectory in the ITRF (Bertiger et al., 2010). Laser retro reflectors (LRR) are used to provide external calibration to the geodetic GPS positioning receivers (Wen et al., 2019), and so the laser ranging data can be used to constrain the POD solutions.

2.3.6 Thrusters

Each satellite has twelve 10-mN gas thrusters for attitude control, and two 50-mN gas thrusters for obit control (Wen et al., 2019). The thruster activation data, such as the commanded thruster 'on times', can be retrieved from the THR1B data product.

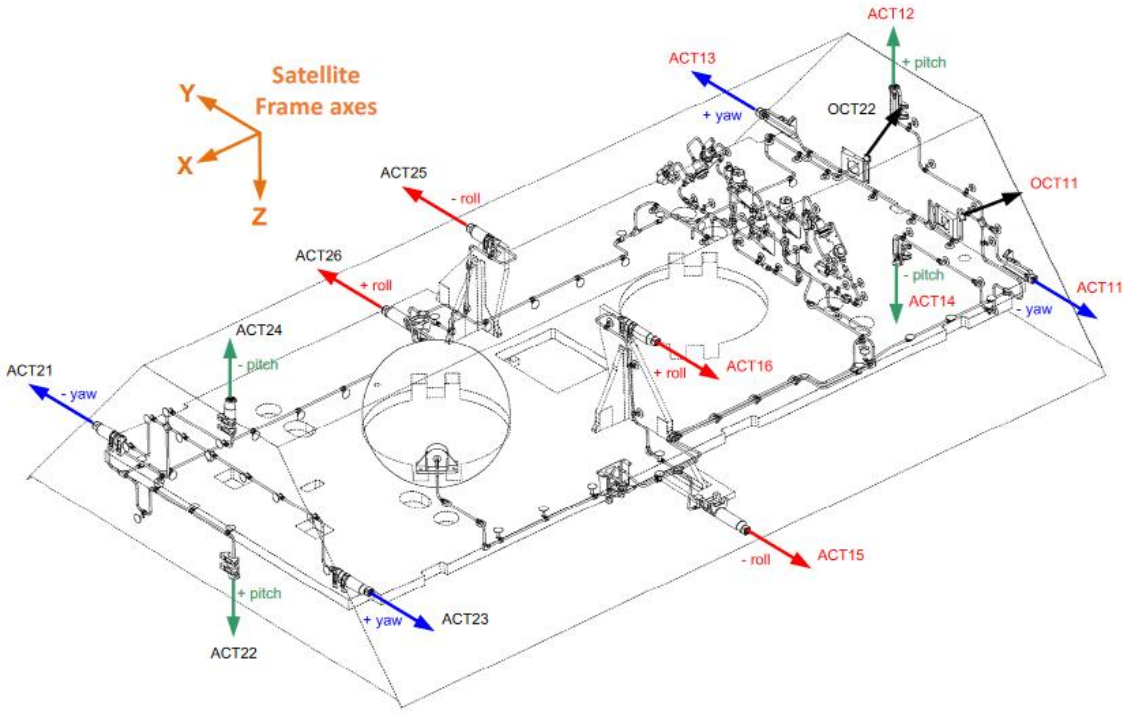

Figure 7: Coloured arrows showing the location of the thrusters on the satellite body (Wen et al., 2019).

2.4 Data products and instrumentation for GOCE

The GOCE team disseminates three levels of processed raw data products, similar to GRACE. To compare the GRACE gradiometer mode (GM) estimated gradients, we use the measurements from the GOCE Electrostatic Gravity Gradiometer (EGG). The EGG measured the gravitational gradient tensor (GGT) in the gradiometer reference frame (GRF), using three orthogonal 3-axis pairs of accelerometers each separated by a 0.5 m baseline (ESA, 2008). Each accelerometer used an electrostatic servo-controller, like the GRACE SuperSTAR accelerometers. The information in Table 9 should be read in tandem with **Figure 6**.

Table 9: GOCE Electrostatic Gravity Gradiometer (EGG) instrument characteristics.

Electrostatic Gravity Gradiometer (EGG)		
Accelerometer Pair (AF)	Ultra-sensitive $10^{-12}\frac{m}{s^2}/\sqrt{Hz}$	Less-sensitive $10^{-10}\frac{m}{s^2}/\sqrt{Hz}$
A_1, A_4	X, Z (GRF)	Y (GRF)
A_2, A_5	Y, X (GRF)	Z (GRF)
A_3, A_6	Z, X (GRF)	Y (GRF)

Like the GRACE SCA1B data product provides the satellite attitude in the SRF with respect to the IRF, the GOCE EGG_GIM_1B data product provides the satellite attitude of the GRF with respect to the IRF. Instead of using Level 1B POD solutions, we use the Level 2 GOCE trajectory in the form of the SST_PSO_2 data product due to large data gaps in the Level 1B data product. In Table 10, we show the GOCE data products used in this thesis. The GOCE Level 1B and 2 data products are provided in GPS time, defined as continuous seconds from January 6, 1980.

Table 10: Description of GOCE data products used in thesis.

Product	**Description**	**Sampling Rate**	**Frame**
EGG_GGT_1B	Gravitational gradient tensor.	1Hz	GRF
SST_PSO_2	Position and velocity with modelling errors.	0.1Hz	ITRF (2014)
EGG_GIM_1B	Transformation matrices from GRF to IRF.	0.2Hz	--

3 GRACE Dual-Satellite Gradiometer Mode

In this chapter, we focus on the concept of the GRACE dual-satellite gradiometer mode (DS-GM), introduced by Peidou & Pagiatakis (2019). After a review of the concept of GM, including the description of the processing methodology, we derive our own estimate for the gravitational gradient tensor (GGT) using GRACE-A and -B DS-GM. We then use our GRACE-A and -B DS-GM gradients as well as those measured by GOCE, to investigate the Himalayas for the same period as presented by Peidou and Pagiatakis (2019) for validation.

3.1 Data pre-processing

A filter is a linear time invariant (LTI) system designed to pass, reject, or modify spectral constituents in a signal (Smith, 2013). Filtering is an essential processing step for the gradiometer mode (GM). For example, we apply zero-phase (forward/backward) Gaussian band-pass filtering to the calibrated accelerations in the 10^{-4} to 10^{-1} Hz bandwidth to isolate the linear part of the SuperSTAR accelerometer response (Touboul et al., 1999).

One compact representation of an LTI system is the impulse response function h. The LTI system is described by the gain function – how the system scales an input sine wave in amplitude, and the phase function – how the system shifts an input sine wave in angle. For the gain function, the corner frequency specifies where the system output scales the input by $1/2$ of the peak power of h. It is necessary to compensate for the phase delay introduced by filters in some applications, as the phase delay causes deflections of signal constituents in the system output. One method of input/output (I/O) phase-preservation is to design an LTI system whose outputs are weighted by future inputs yet to be received – this is known as a non-causal system (Gelb, 1974). When the weighting function is finite, it is a non-causal (aka smoothing) finite impulse response system.

The equation for discrete time non-causal convolution is provided in Equation (3.1). The input values $x_{[i-j]}$ are to be interpreted as sampling continuous quantities at discrete and regular intervals. The output signal $y_{[i]}$ is of size N and the impulse response $h_{[j]}$ is size M. In this thesis, we use a Gaussian impulse response $h_{[j]}$ for filtering to minimize the effect of Gibbs phenomenon (Smith, 2013), i.e., the presence of power-leakage/rippling of neighboring frequencies due to the

discontinuous nature of the ideal low pass filter (aka boxcar function) that has sharp edges at the corner frequency. The rippling effect is minimized because the Fourier transform of a Gaussian window is also Gaussian (Smith, 2013).

$$y_{[i]} = \sum_{j\,=\,-M/2+1}^{M/2} x_{[i-j]}\, h_{[j]} \tag{3.1}$$

The size of $h_{[j]}$ is 7σ, where $\sigma^2$is the variance of the Gaussian window, since distances greater than 3σ contribute minimal weights to an output $y_{[i]}$. Circular convolution in the time domain is equivalent to multiplication in the frequency domain (Jenkins & Watts, 1968) and so, we perform all our filtering in the frequency domain directly for computational performance improvements. As an aside, lower-case symbols represent variables in the time (or space) domain, whereas their upper-case equivalent symbols indicate their Fourier transforms in the frequency domain.

The procedure for 1D filtering in the frequency domain is as follows:

Step 1. Take the FFT of $x(t)$ to derive $X(f)$.

Step 2. Design the low-pass Gaussian impulse response in time $h(t)$ by:

$$h(t) = \frac{1}{2\pi\sqrt{\sigma}}\, e^{-(\mathrm{x})^2/2\sigma^2}, \tag{3.2}$$

where x is the distance from the origin and σ is the standard deviation. The standard deviation of the Gaussian impulse response relates to the filter design corner frequency f_c by:

$$\sigma = \frac{Fs\sqrt{\ln(2)}}{2\pi f_c}, \tag{3.3}$$

where Fs is the sampling rate, as provided in Bottacchi (2008). We can also design high-pass, band-reject or band-pass filters from the low-pass impulse responses using Table 11, based on desired corner frequencies.

Step 3. Wrap the negative portions of $h(t)$ (in time) around and store the array to extreme right end to form $h_k(t)$, which must be padded with intermediary zeros to make an array of size N, as described by Press et. al, (1999). The size of $h(t)$ before zero-padding must

also have an odd number of elements, so weighting is not biased in either the forward or reverse direction relative to $y_{[i]}$.

Step 4. Take the FFT of $h_k(t)$ to derive the transfer function $H_k(f)$.

Step 5. Calculate filtered output by $Y(f) = X(f)^* H_k(f)$.

Step 6. Take the inverse FFT of $Y(f)$ to recover $y(t)$ in the time domain.

As mentioned in Step 2 of the filtering procedure, other filters in the time domain may be constructed from the low-pass impulse response function. This procedure is outlined in Table 8, where $\delta(t)$ is the unit-impulse function as given by:

$$\delta(t) = \begin{cases} 1 & t = 0 \\ 0 & t \neq 0 \end{cases}. \tag{3.4}$$

Table 11: Description of filter design using the low-pass impulse response function.

Low-Pass	$h_{lp} = h(t)$
High-Pass	$h_{hp} = \delta(t) - h_{lp}$
Band-Pass	$h_{bp} = \delta(t) - h_{br}$
Band-Reject	$h_{br} = h_{lp} + h_{bp}$

We now design an LTI system to filter GRACE accelerometer measurements in the pass-band of 10^{-4} to 10^{-1} Hz. Subsequently, we input a unit-impulse function $\delta(t)$ to the system and produce the power spectrum from the output (**Figure 8**). This shows the transfer function of the band-pass filter, and we can see the frequency responses passes the -3 dB points for the two corner frequencies of the SuperSTAR accelerometer measurement bandwidth (MBW).

In **Figure 9**, we investigate the impact of filtering GRACE-FO accelerations provided from the ACT1A data product. Before filtering, the accelerations in the along-track direction (X_{SRF}) are transformed from the accelerometer frame (AF) to the Science Reference Frame (SRF) using Equation (2.2). We see that outside the MBW, the filtered accelerations are attenuated relative to the accelerations without filtering, while preserving the pass-band. In both signals, we see spectral peaks positioned to the satellite orbital period harmonics. Further, both spectra show pink $(1/f)$

noise, albeit this is attenuated in the filtered signal. The cross-track (Y_{SRF}) and nadir-pointing (Z_{SRF}) accelerations show similar characteristics after filtering to the along-track (X_{SRF}) direction.

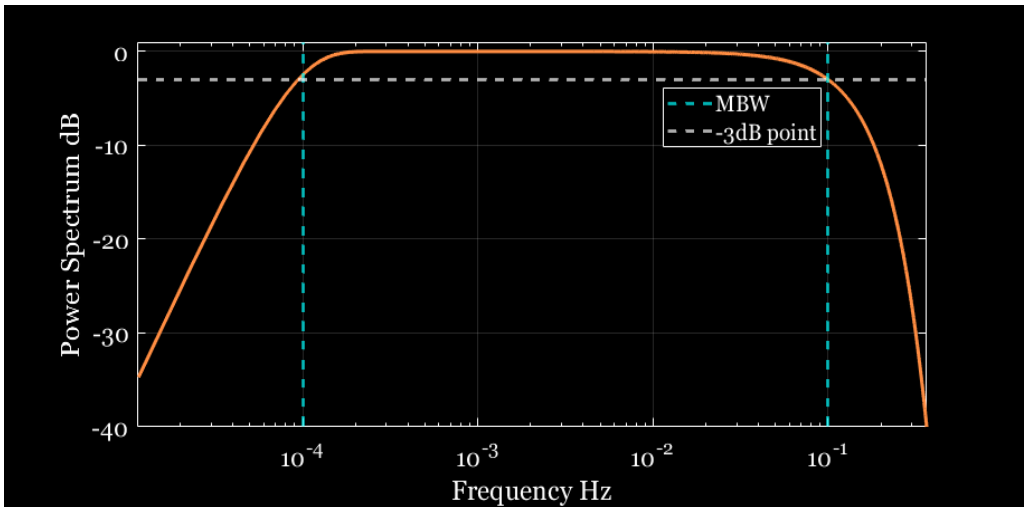

Figure 8: Band-pass filter frequency response to isolate the [10^{-4} to 10^{-1}] Hz bandwidth.

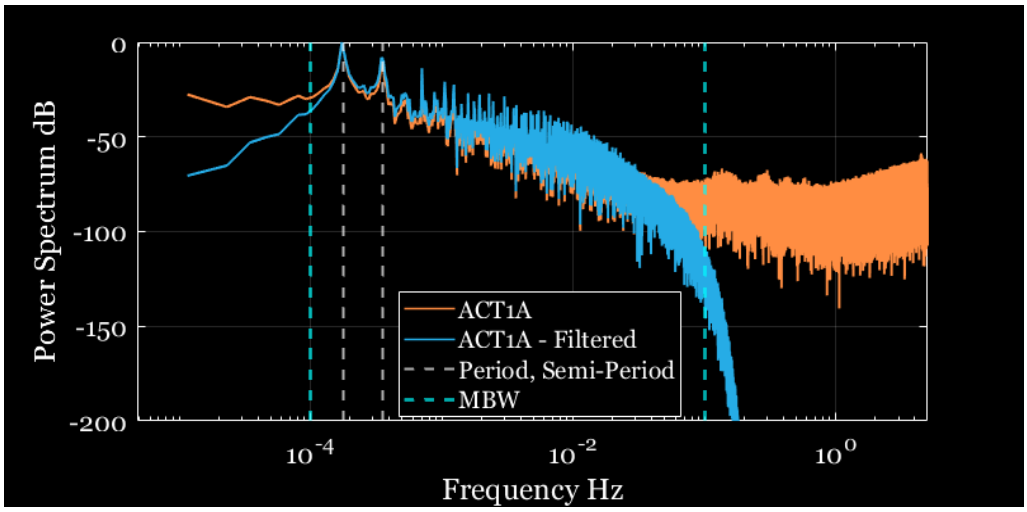

Figure 9: Power Spectrum of filtered and retrieved linear accelerations provided from the ACT1A data product. Accelerations are given in the along-track direction. The gray dashed lines indicate the frequencies of the satellite orbit.

3.2 Multi-resolution analysis

Multi-resolution analysis (MRA) has successfully been used in gravity field analysis (Peidou et al., 2017; Peidou & Pagiatakis, 2019). In Section 5.2, we perform a multi-resolution analysis (MRA) to analyze our GRACE-FO GM gradients and compare the solutions to those observed by the GOCE gradiometer. In this section, we describe the theoretical and algorithmic basis for method that we apply.

Spectral analysis is accomplished by transforming a signal, a function of time or space, to a sinusoidal basis which, through its decomposition, showcases the signal spectral variance (power). The transformation can provide the researcher a more compact and succinct representation to identify periodicities within the signal. The periodicities carry information about the system and may require characterization to develop an understanding of the system.

One method of spectral analysis is the Fourier transform, which represents the periodicities as global features of the signal. This is adequate, provided the signal has already reached a statistical equilibrium (signal stationarity), since the statistical properties (mean and variance) do not change over time (Jenkins & Watts, 1968). When the signal is non-stationary, transforming the signal from time to the time-frequency domain (simultaneously) has advantages over global frequency decomposition (e.g., Fourier transform). For instance, the time-frequency representation is better for detecting localized features in the signal (Ghaderpour & Pagiatakis, 2017). One method for time-frequency decomposition is the Wavelet transform.

There is an intrinsic limitation in achieving infinitesimal time and frequency resolution simultaneously. This is known as the uncertainty principal (Keller, 2004). Accordingly, the wavelet transform uses inversely proportional to frequency sized windows for spectrum computation (Brunton and Kutz, 2019). The continuous wavelet transform (CWT) is given in Brunton and Kutz (2019):

$$\gamma(a,b) = \frac{1}{\sqrt{a}}\int_{-\infty}^{\infty} f(t)\psi^*\left(\frac{t-b}{a}\right)dt, \tag{3.5}$$

where * signifies complex conjugate, a denotes scaling, b is translation, and ψ is the 'mother wavelet' function. This equation is analogous to a Fourier transform because the signal is weighted

by a set of basis functions (aka convolution). Unlike the Fourier transform, which specifies the basis to be cosine and sine, the wavelet transform only defines the framework for the transformation.

As the wavelet transform is a function of a and b, it gives indication on how the transformation provides time and frequency localization simultaneously. One may imagine compressing and sliding the mother wavelet function along a signal to correlate and detect short bursts of power dispersed throughout the signal. The mother wavelet function, from which all shifted and translated wavelets are derived, must obey several conditions. These conditions result in a function that must possess a band-pass spectrum (Keller, 2004). The CWT therefore requires weighting by an infinite amount of translated and scaled mother wavelet functions, or equivalently, infinitely many band-pass filter kernels to span the whole spectrum.

The discrete wavelet transform (DWT) replaces the integral in Equation (3.5) with a summation index of the signal size. There are many methods of discretizing the scale and translation parameter. One method is based on a dyadic sampling sequence – this results in a dyadic decomposition in the frequency spectrum (Barros, 2012), or equivalently, a dyadic sampling grid of the CWT. The DWT is a separable transformation and so, we can compute the 2D DWT for an input matrix $f(x, y)$ by computing the 1D DWT along the rows followed by the resultant columns (Gonzalez & Woods, 2018). We use the DWT in this work where the dyadic sampling sequence separates the gravity functionals (in our study, gravitational gradients) into approximately independent frequency bands to show the effective bandwidth of the functionals (Mallat, 1999; Barros, 2012; Smith, 2013; Peidou & Pagiatakis 2019). *This decomposition is the multi-resolution analysis (MRA).*

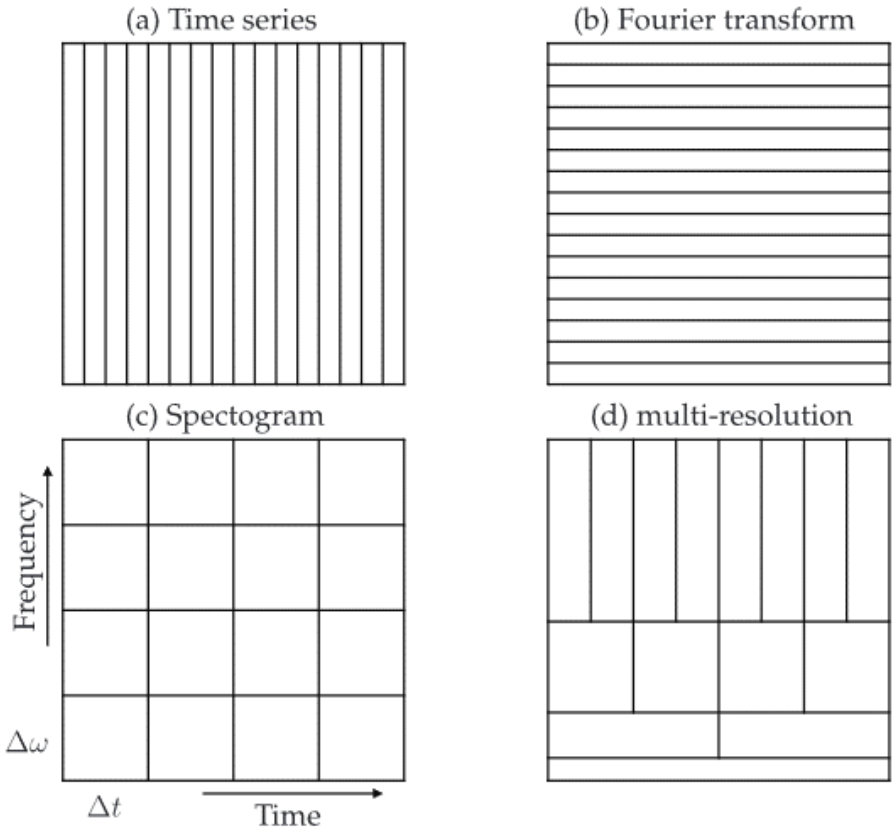

Figure 10: Representation of the uncertainty principle for time-frequency resolution ambiguity for (a) time-series analysis; (b) the Fourier transform; (c) the short-time Fourier transform that uses constant sized window sizes for spectrum computation; and (d) the Discrete wavelet transform that uses dyadic window sizes for spectrum computation.

Mallat (1999) developed a 'fast' implementation of the DWT through a recursive multistage filter bank called the Fast wavelet transform (FWT). For j levels of decomposition, the 1D FWT can be written compactly as a simultaneous high- and low-pass filtering procedure:

$$\varphi_{j+1} = \varphi_j * g[n], n = 0, 1, 2, \dots N, \tag{3.6}$$
$$\psi_{j+1} = \varphi_j * h[n], n = 0, 1, 2, \dots N,$$

where * denotes convolution, g is the low-pass filter kernel and h is the high pass filter kernel. When, $j = 1$, $\varphi_1 = x[n]$, where $x[n]$ is the input signal. To ensure perfect reconstruction of the decomposed signals, the filter kernels must be quadrature mirror filters. In most implementations of the FWT, each level of decomposition is down sampled by 2 as depicted in **Figure 11**. Since we use the FWT for gravity field analysis, we do not perform the down sampling procedure in our

algorithms. To implement the 2D MRA using the FWT for gravity field analysis, we extend our 1D Gaussian filtering algorithm, described in section 3.1, for implementing the 1D FWT. We then extend the 1D FWT to 2D by computing the 1D FWT along rows, followed by the 1D FWT on the resultant columns.

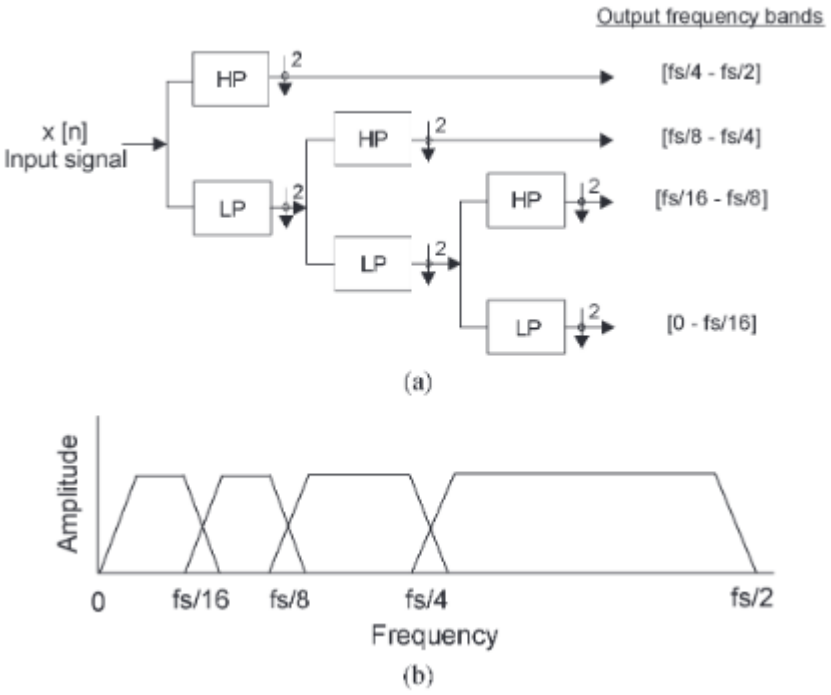

Figure 11: Fast wavelet transform (FWT) multistage filter bank and associated logarithmic frequency decomposition (Barros, 2012).

3.3 Review of GRACE gradiometry

Based on the proof-of-concept introduced by Peidou and Pagiatakis (2019), the GRACE gradiometer mode (GM) was developed for the purpose of using GRACE, GRACE-FO, and future gravity space missions as 'gradiometer missions'. Certainly, GRACE has never carried a gradiometer, it is only the concept of GM which creates a fictitious gradiometer system very similar to GOCE, only the GRACE 'gradiometer' has longer and variable baselines, an unprecedented paradigm for space-based gravitational gradiometry.

In GM, Peidou and Pagiatakis (2019) used GRACE-A and -B in unison to create the fictitious 'gradiometer'. This innovative approach combined two sets of measurements in very close proximity, belonging to each satellite, in the form of non-gravitational accelerations measured by

the on-board 3-axis accelerometer, precise satellite positioning, and satellite attitude, to estimate the full gravitational gradient tensor (GGT) from Level 1B data products only. We herein denote this configuration as dual-satellite GM (DS-GM). To our knowledge, the implementation from Keller & Sharafi (2005) and Peidou & Pagiatakis (2019) are the significant, if only, contributions of GRACE and GRACE-FO gradiometry, so far.

Attitude changes on low Earth orbit (LEO) satellites are induced by torques from non-gravitational perturbations and gravitational gradients (Gerlach, 1965; Peidou & Pagiatakis, 2019). The most significant non-gravitational perturbations for LEO satellites are atmospheric drag and solar radiation pressure (Wang et al., 2023). The outcome of GM was the creation of a system which is very similar to GOCE, where each pair of accelerometers was referenced to a common instrument reference frame. The GRACE 'gradiometer' had a variable baseline and the accelerometers composing it were on a different reference frame, as opposed to the GOCE fixed baseline of 0.5 m.

In GM, Peidou & Pagiatakis (2019) (fictitiously) moved the trailing satellite to be as close as possible to the 'fixed' leading satellite. This procedure of moving the trailing satellite to the air space of the fixed leading satellite, at closest approach, is herein known as the 'time-shift' (McCullough, 2019) procedure. After the time-shift, they then rotated the time-shifted SRF of the trailing satellite about the Z-axis by 180° to achieve a consistent positive axis convention for both SRFs. In this configuration, the time-shifted SRF and leading SRF did not have their axes perfectly aligned. The non-gravitational accelerations on each satellite at closest approach (a few to hundreds of metres) were considered the same. Therefore, the torque which caused the misalignment between each SRF was due to gravitational gradients.

By reciprocity (Peidou & Pagiatakis, 2019), the action of aligning the time-shifted trailing SRF to the leading SRF added the gravitational gradient. The gravitational gradient was estimated at the geometric centre between the positions of the two satellites at the closest approach. In the GRACE dual satellite GM (DS-GM), Peidou & Pagiatakis (2019) minimized the distance between the leading and trailing GRACE-A and -B satellites; therefore, they viewed each satellite at closest approach as one to create the 'gradiometer'.

The concept of the GM established by Peidou & Pagiatakis (2019) was considered valid and realistic when the following conditions were satisfied. First, when they moved (fictitiously) the trailing satellite to the airspace of the leading satellite (at closest approach), the baseline separation between the accelerometers was small enough to satisfy the definition of the gradient operator. Next, the spatial separation of the satellites at closest approach was short enough, such that the non-gravitational perturbations affected the time-shifted trailing and leading satellite in the same way. This assumption was necessary to have inferred that it was the gravitational gradient torque which induced the attitude change on the satellite.

To ensure that the non-gravitational perturbations affected both satellite accelerometers in the same or similar way, Peidou & Pagiatakis (2019) then asserted the dynamic regime of the thermosphere was spatially homogeneous within the area contained by the accelerometers at closest approach and was also temporally homogeneous during the time which elapsed over the time-shift, which was on average about 26 seconds. This was very realistic to postulate in GM, since algorithms that derived neutral wind datasets from Doppler shift measurements, outlined in NASA's Upper Atmosphere Research Satellite study (Shepherd et al., 2012), assumed spatial (within a range of 300 km) and temporal (within 7-10 minutes) homogeneity of the dynamic behavior of the thermosphere (Zhang, 2003). While in GM, the satellite separations at closest approach did not exceed several kilometres (km) and the time-shift did not exceed 35 seconds.

Finally, during the time which elapsed during the time-shift, they assumed that the influence of the Earth's rotation on the gradient signal was not sensed in the GM gradients, and the gravitational field was assumed to be static. Both were realistic assumptions, since their multi-resolution analyses (MRA) of the gradient solutions showed that the fidelity of the gradients was significantly less.

3.4 Processing methodology for DS-GM

We now describe the processing methodology for DS-GM used in this thesis. The processing methodology we apply here is very similar to Peidou & Pagiatakis (2019), except for a few additional steps which may have been performed by Peidou & Pagiatakis (2019), only not described. To recover the GRACE-A and -B non-gravitational linear accelerations, attitude, and

positions in the International Terrestrial Reference Frame – ITRF, we use ACC1B (1 Hz), SCA1B (0.2 Hz), and GNV1B (0.2 Hz) data products, respectively (Case et al., 2010). All Level 1B data products are in GPS time, and the leading and trailing GRACE satellites are denoted as -A and -B, respectively. GRACE Level 1A data products are not released.

To initiate the processing of the data, we apply scale and bias calibration parameters to the accelerations determined by Bettadpur (2009), as described and provided in Section 2.3. Subsequently, we apply zero-phase (forward/backward) Gaussian band-pass filtering to the calibrated accelerations in the 10^{-4} to 10^{-1} Hz bandwidth to isolate the linear part of the SuperSTAR accelerometer response (Touboul et al., 1999). Next, we interpolate the filtered and calibrated accelerations from 1 Hz to 10 Hz using cubic splines, so that the minimum separation between the satellites can be evaluated (cf., Peidou & Pagiatakis, 2019).

Following the preprocessing stage, we transform the positions of the satellites from the ITRF to the TIRF (aka IRF), using the IAU-2000/2006 reduction method to comply with IERS-2010 Conventions (Luzum & Petit, v. 1.3.0., 2019; Kaplan, 2005). To ensure reliable interpolation of the satellite attitude, we apply corrections to the rotational quaternions for discontinuities to flip signs, if needed, to maintain continuity in time (Wu et al., 2006). The 'flip' procedure may be needed, since there is an intrinsic sign ambiguity in quaternion representations, as any rotation can be represented by the positive rotation and the negative rotation, due to the different quadrants in the trigonometric circle.

Finally, we interpolate the IRF positions and the satellite attitude to the GPS time-tags of the satellites GRACE-A and -B accelerations using cubic splines. For every epoch t_0, we then calculate a time-shift τ (aka time-offset) to move GRACE-B to GRACE-A by minimizing the 3D distance squared between GRACE-A and -B using the following optimization function:

$$J = [\boldsymbol{r_A}(t_0) - \boldsymbol{r_B}(t_0 + \tau)]^T [\boldsymbol{r_A}(t_0) - \boldsymbol{r_B}(t_0 + \tau)], \tag{3.7}$$

where the position of each satellite s (A or B) in IRF is $\boldsymbol{r_s} = [x_s(t), y_s(t), z_s(t)]^T$. We use the calculated time-shifts τ and align GRACE-B accelerations to GRACE-A, taking the accelerations from:

$$\text{SRF B}(t_0 + \tau) \rightarrow \text{IRF} \rightarrow \text{SRF A}(t_0). \tag{3.8}$$

We then compute the differential mode (DM) accelerations:

$$\boldsymbol{a_d}(t_0) = \frac{1}{2}\big(\boldsymbol{a_A}(t_0) - \boldsymbol{a_B}(t_0 + \tau)\big), \tag{3.9}$$

and baselines:

$$\boldsymbol{r_d}(t_0) = \frac{1}{2}\big(\boldsymbol{r_A}(t_0) - \boldsymbol{r_B}(t_0 + \tau)\big), \tag{3.10}$$

both referenced in SRF A(t_0). Finally, we estimate the GGT $\boldsymbol{\Upsilon}$ using the following:

$$\boldsymbol{\Upsilon}(t_0) = \begin{bmatrix} -2\frac{a_{d,x}}{r_{d,x}} & -\frac{a_{d,y}}{r_{d,x}} - \frac{a_{d,z}}{r_{d,y}} & -\frac{a_{d,z}}{r_{d,x}} - \frac{a_{d,x}}{r_{d,z}} \\ sym & -2\frac{a_{d,y}}{r_{d,y}} & -\frac{a_{d,z}}{r_{d,y}} - \frac{a_{d,y}}{r_{d,z}} \\ sym & sym & -2\frac{a_{d,z}}{r_{d,z}} \end{bmatrix}. \tag{3.11}$$

For the GRACE gradients, we use a Hampel identifier (Pearson et al., 2016) to remove GGT outliers that significantly deviate from the typical gradient scale, with some additional manual correction as necessary. We skip this processing step for GOCE, as outlier detection is performed in the GOCE Level 1B GGT processing (Siemes, 2018). We compute monthly solutions by determining the average gradients on 1° x 1° grid cells. We then apply an 800 km 2D Gaussian low-pass spatial filter to the gridded gradients to smooth out high-frequency noise.

If a grid cell has no value in a monthly solution, we use inverse 2D Gaussian weighting interpolation to fill the missing value. Since the gravitational gradients do not significantly attenuate with altitude (Keller & Sharifi, 2005; Peidou & Pagiatakis, 2019), we directly compare, as did Peidou & Pagiatakis (2019), the gradients between GOCE and GRACE, without any upward or downward continuation despite the different flight altitudes.

3.5 GRACE-A and -B DS-GM and GOCE GGT solutions

To recover the GOCE GGT in the GRF and positions in the ITRF, we use EGG_GGT_1B (1 Hz) and SST_PSO_02 (0.1 Hz) data products, respectively (ESA, 2008). We then apply band-pass filtering to the GOCE GGT in the 5.10^{-3} to 10^{-1} Hz bandwidth to isolate the linear part of the GOCE gradiometer response (ESA, 2008; Ince, 2016).

We compute the GRACE-A and -B DS-GM GGT and retrieve the GOCE GGT in the respective gradiometer reference frame (GRF). From the GRF, we transform to a common local astronomic (i.e., topocentric) East-North-Up (ENU) frame, using the azimuth of the satellite flight trajectory at each point to make valid comparisons. We rotate the GGT about the respective Z-axis (vertical) to align the X-axis toward North and Y-axis toward East. The Z-axis points Up and deviates from the ellipsoidal normal by a very small deflection angle. To preserve the GGT precision, we keep the gradients as close as possible to the original instrument reference frames (Eshagh, 2010).

It is well outside the scope of this study to examine and discuss what our gradients may show vis-à-vis the complex geological structure and dynamics of the tectonic plates in this region. This would entail a combination of complementary methods and theories such seismic, magnetic, and gravity, to name a few. In this research we endeavour to make only general comments on the gradient patterns produced by our method because they compare favourably with the global characteristics of the Earth's structure and with measurements obtained from GOCE mission.

In our first investigation of GM, we use GOCE and GRACE-A and -B dual-satellite GM (DS-GM) gradients (**Figure 12** and **Figure 13**) to investigate the ongoing collision of the Indian and Eurasian tectonic plates, one of the most complex subduction zones on Earth, extending primarily in the East-West direction (Northern India), curving south at an angle of nearly 90°, forming the Arakan trench[9] to the east and the Chaman fault[10] to the west of the Indian plate. (Tiwari et al., 2010). These geological and geophysical processes are known to be expressed in the gravitational gradients as north-south (N-S) changes from positive to negative anomalies (Panet et al., 2014; Peidou & Pagiatakis, 2019), with features that may delineate subduction zones (Richards & Engebretson, 1992).

In both solutions (except **Figure 13a**) in the Himalayas region, we clearly see the N-S gradient polarity switches, only the GOCE gradients are of much shorter-wavelength due to the much

[9] Trenches form when an oceanic (more dense) plate subducts beneath another (less dense) over-riding plate at a convergent plate boundary, sinking at the subduction zone (Stern, 2021). Trenches are related (but distinct) to continental collision, where two buoyant continental plates collide. Since the continental plates are very-thick and buyout, subduction typically stops, forming high mountain ranges, like, e.g., the Himalayas or Zagros (Stern, 2021).
[10] A fault is boundary between rock bodies where relative movement has occurred (Earle & Panchuk, 2019).

smaller 0.5 m baselines. The longer baselines of the GRACE 'gradiometer' allow the detection of deeper and longer-wavelength structural anomalies of the crust and upper mantle as discussed in the following sections, particularly in Section 4.4 (multiresolution analysis – MRA). In the northern direction (**Figure 12a** and **Figure 12b**, respectively), the GRACE-A and -B DS-GM and GOCE gradients similarly delineate the Eurasian-Indian plate boundary.

The GRACE northern gradients (**Figure 12a**) transition from negative through zero, right at the tectonic plate boundary line (gray solid line), then to positive northward exhibiting long-wavelength deeper Earth structure as revealed from the ascending tracks of the 'gradiometer'. This pattern is similar to the geoid[11] model in the region (**Figure 14**; gray solid line); it is known that the geoid reflects the deeper, and longer-wavelength structure of the Earth. The equivalent GOCE gradient map (**Figure 12b**) exhibits similar transition characteristics at a much shorter-wavelength, with a strong positive gradient right at the tectonic plate boundary (gray solid line).

In the eastern direction, the GRACE-A and -B DS-GM (**Figure 13a**) solution may show the Arakan trench to the east (labelled on Figure), whereas GOCE (**Figure 13b**) delineates weakly the plate boundary to the north (gray solid line), without other significant features elsewhere in the region. We find a good agreement to the GRACE-A and -B DS-GM solutions for the same period and region as presented by Peidou and Pagiatakis (2019), albeit with some differences in the eastern and vertical gradients. The reasons for these differences are not clear.

In **Figure 17** (Section 4.2), we show the vertical gradients for GRACE-A and -B DS-GM and GOCE over the Himalayas region (purple dashed box), also comparing GRACE-B single-satellite (SS)-GM gradients. The trace of the gravitational gradient tensor (GGT) $V_{TT} = V_{EE} + V_{NN} + V_{UU} = 0$ should be zero due to Laplace's condition (Rummel et al., 2011). This means that if we add the eastern, northern, and vertical gradient solutions (**Figure 12a**, **Figure 13a**, and **Figure 17a**, respectively) from GRACE-A and -B DS-GM by point, the result should be zero. This typically serves as a useful indicator to analyze the quality of the GGT, since we can show that our solutions satisfy a criterion that we physically expect. Accordingly, Peidou and Pagiatakis (2019)

[11] The gravity equipotential surface that best approximates the mean sea level over the Earth is the geoid (Vaníček & Krakiwsky, 1986).

performed a frequency domain analysis of the GGT trace to provide an error estimate for GRACE-A and -B DS-GM solutions. In this contribution, we initially experiment by using the GGT trace as a means of identifying outliers in our GM gradients.

During this investigation, we observe that the magnitudes of GM gradients can differ due to the different baseline separations of the 3-axis GRACE gradiometer that change in each axis of the SRF, simultaneously. Further, we see that the amplitude of the trace appears correlated with the dynamic baselines. Hence, it is not clear how to interpret the Laplace condition, when, e.g., the evaluated differential mode (DM) positions (Equation (3.10)) approaches zero faster than the DM accelerations (Equation (3.9)), resulting in GGT estimates that tend to infinity (Equation (3.12)). This is more noticeable along the X-axis of the SRF, since the tandem configuration of the leading and trailing GRACE satellites periodically results in very-short baselines at closest approach yielding near-zero DM positions. Consequently, the trace $V_T(SRF) = V_{XX} + V_{YY} + V_{ZZ} \neq 0$ is clearly violated in the SRF, where V_{XX} is relatively very large compared to the other GGT trace components. Further, there may also be residual bias and scale defects from the GRACE-A and -B accelerometers, which when combined into one as the 'gradiometer' further bias the final DS-GM gradients, even after applying the instrument calibration factors. All together, future work should further investigate the Laplace condition for gradient solutions in both single- and dual-satellite gradiometer modes (GM).

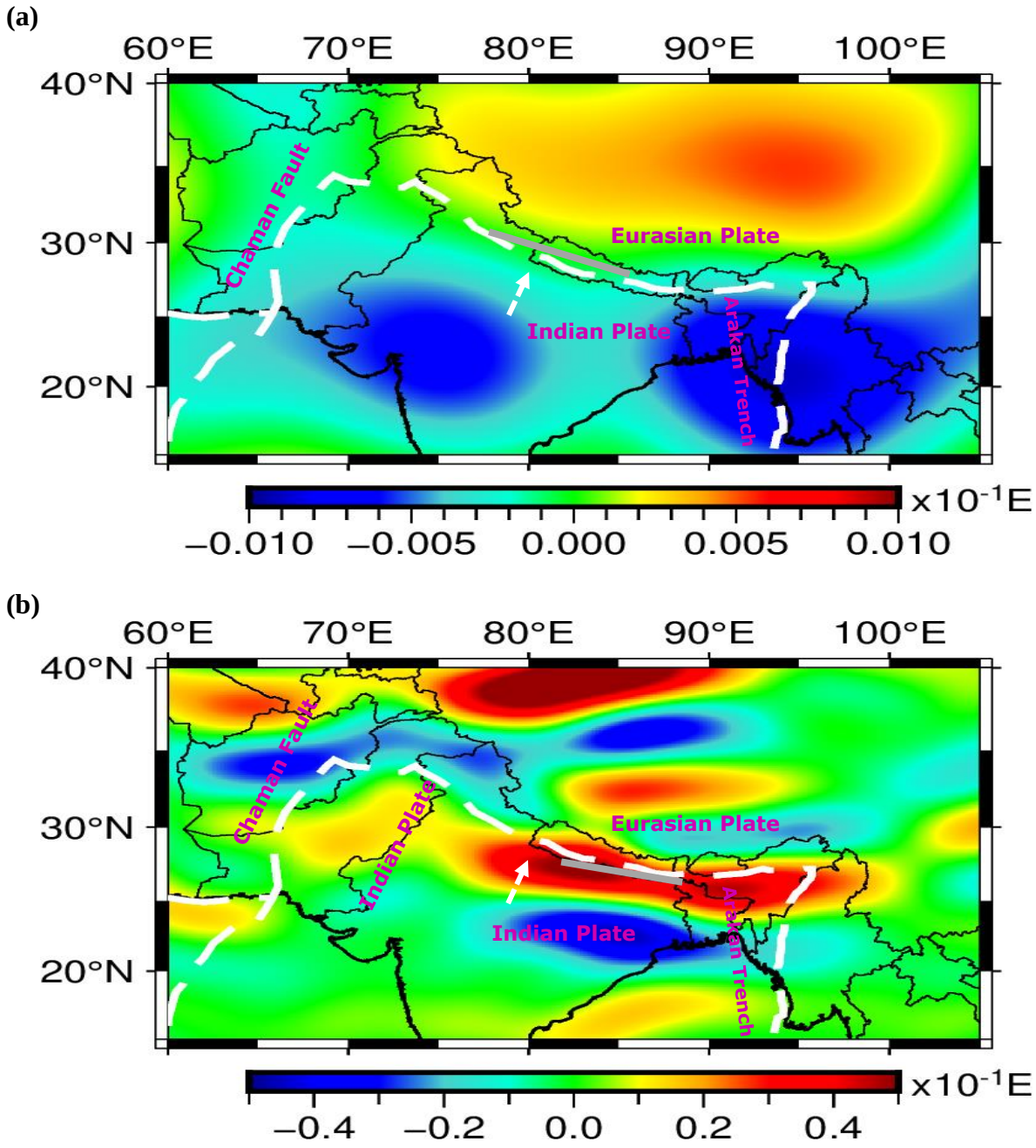

Figure 12: Northern gradients (ascending tracks; May/June 2010) in the Himalayas region. (a) GRACE-A and -B DS-GM and (b) GOCE. Note the difference in scale between the GOCE and DS-GM gradients, likely due to the different baseline lengths resulting in longer-wavelength and deeper probing of the Earth's structure. Tectonic plate boundaries are plotted in white dashed line and approximate plate movement is the shown by white dashed arrow. Gray lines denote features described in the text preceding the Figure.

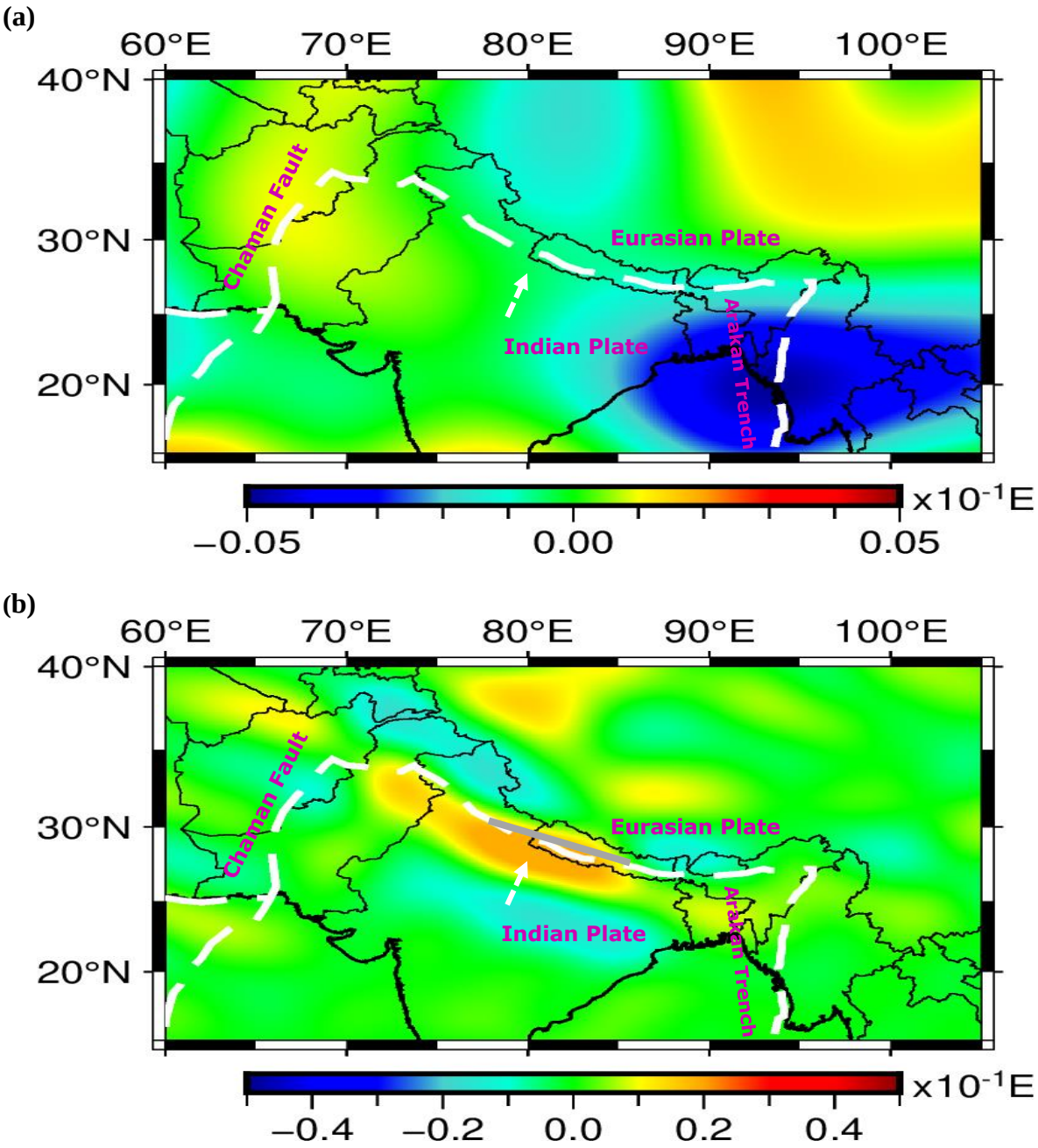

Figure 13: Eastern gradients (ascending tracks; May/June 2010) in the Himalayas region. (a) GRACE-A and -B and (b) GOCE. Note the difference in scale between the GOCE and DS-GM gradients, likely due to the different baseline lengths, resulting in longer wavelength and deeper probing of the Earth's structure. Tectonic plate boundaries are plotted in white dashed line and approximate plate movement is shown by white dashed arrow. Gray lines denote features described in the text preceding the Figure.

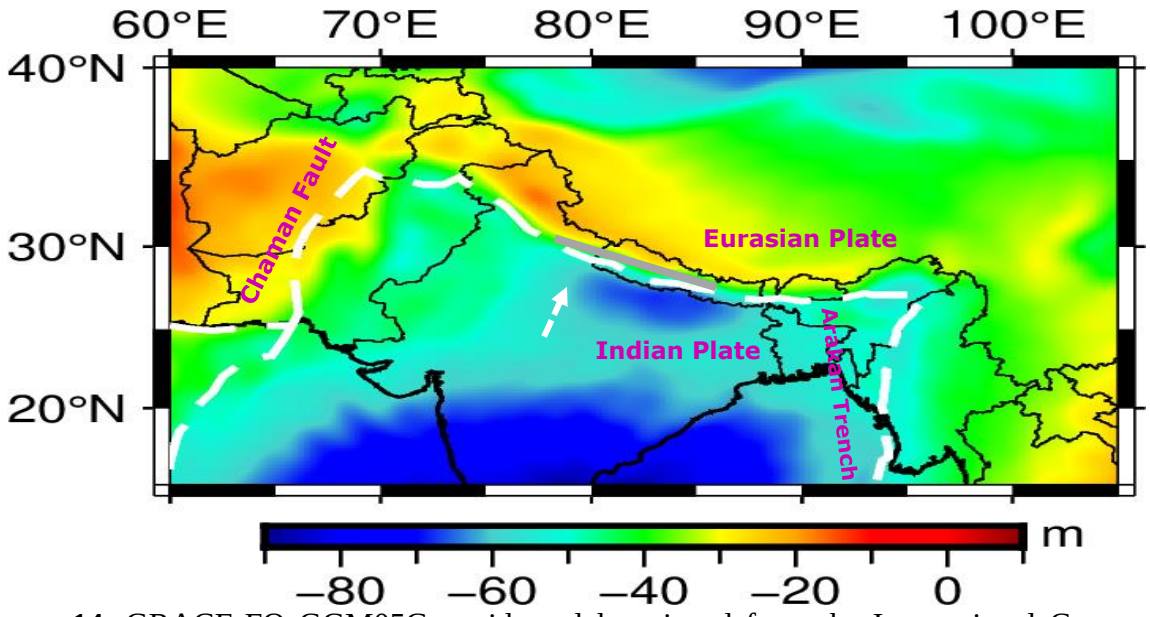

Figure 14: GRACE-FO GGM05G geoid model retrieved from the International Centre for Global Earth Models (ICGEM) and plotted in Generic Mapping Tools (GMT). Tectonic plate boundaries are plotted in white dashed line and approximate plate movement is shown by white dashed arrow. Gray lines denote features described in the text preceding the Figure.

3.6 GRACE-C and -D DS-GM and the accelerometer transplant

The GRACE-D accelerometer was powered down in 2018 (Harvey et al., 2022). Since the GRACE-D accelerometer measurements are needed for accurate gravity field recovery, the JPL Science Data System 'transplants' (aka generates) accelerometer measurements for GRACE-D, using the operational GRACE-C accelerometer measurements. In Section 3.5, we validated the usefulness of GRACE-A and -B DS-GM for geoscience applications. Now, we investigate GRACE-C and -D in dual-satellite GM (DS-GM) for the first time, using measurements from the GRACE-C accelerometer and the transplanted GRACE-D accelerometer data product, keeping all else the same in the processing methodology for DS-GM (Section 3.4).

Our results of GRACE-C and -D DS-GM demonstrate that this configuration of GM does not provide meaningful geophysical information. For the May/June 2021 V_{xx} (SRF) solution (**Figure 15**), nearly 500 thousand gradient estimates reside in the zoom-in region, out of which only 676 estimates are non-zero. In **Figure 15**, we only show the V_{xx} (SRF) gradients as each GGT component is non-zero at the same coordinates. However, for any given non-zero value, they each have different amplitudes. To produce these results, we use the GRACE-D version 04 transplant

(ACT V04) data product (Wen et al., 2019). We provide further details about the ACT data product, including access information in Section 2.2.

For epoch t_0, in GRACE-C and -D DS-GM, we compute the time-shift δ to move GRACE-D forward (along the flight trajectory) into the airspace of GRACE-C to compute differential mode (DM) accelerations. In the GRACE-D accelerometer transplant method, the Science Data System computes the time-shift δ to move GRACE-C backwards into the airspace of GRACE-D. Both methods have minimized the L2 norm to compute the time-shift and so, there is only one time-shift δ which brings the twin satellites as close as possible to each other, either in the forward or backward direction.

This means that GACE-D accelerometer 'measurements' which are time-shifted toward GRACE-C are precisely GRACE-C's measurements which have been time-shifted in reverse and transplanted to GRACE-D. The result is precisely the same 3D linear acceleration measurements, except for the attitude difference between GRACE-C and -D at closest approach. To correct the attitude difference at closest approach, GRACE-C accelerometer measurements are rotated 180° in yaw (McCullough, 2019). Therefore, for any epoch t_0, GRACE-D's accelerometer reference frame is precisely GRACE-C's SRF at C($t_0 - \delta$), rotated by 180° in yaw, where δ is the time-shift which moved GRACE-C in reverse to GRACE-D. Since there is no misalignment of frames between the SRFs at closest approach in the GM, there is no gravitational gradient torque to estimate. Therefore, we believe that an improved transplanted accelerometer data product should consider the gravitational gradient produced in this study.

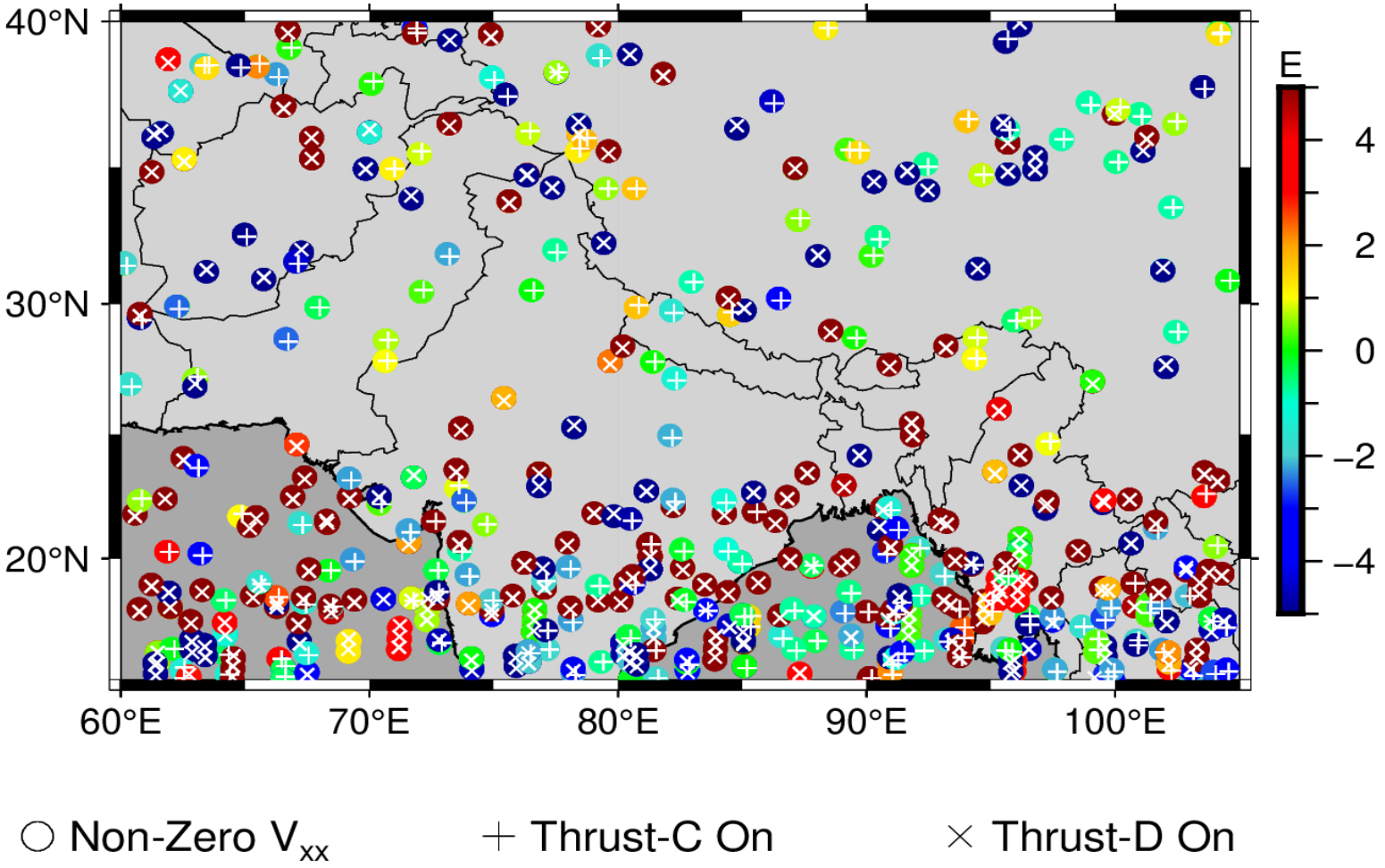

Figure 15: GRACE-C and -D DS-GM V_{xx} (SRF) gradients in the Himalayan region (May/June 2021). The gradients are zero everywhere the solution shows gray. The other GGT components are non-zero at the same coordinates, except with the different amplitudes.

The version 04 transplant (ACT V04) dataset inserts models for the GRACE-C and -D accelerometer response during thruster activations. And so, a 'thruster-free' GRACE-C accelerometer data product is first transplanted to GRACE-D and subsequently, the -D accelerometer thruster models are inserted into the transplanted -D accelerometer data product. Therefore, we expect to observe the 676 non-zero gradient measurements in **Figure 15**, as these correspond to when GRACE-C or -D thrusters were turned on and as a result, where the GRACE-C and -D thruster models are inserted in the accelerometer data products. The reason that each non-zero GGT component has different amplitudes at the same coordinates is because the Science Data System models the accelerometer response during thruster activations by a single value (per thruster type and accelerometer axis) (McCullough et al., 2019; Table 2 and 3). We determine when the thrusters are active using the GRACE-C and -D THR1B data products. In **Figure 16**, we show the time-series of the DM accelerations in the GRACE-C Y_{SRF} direction.

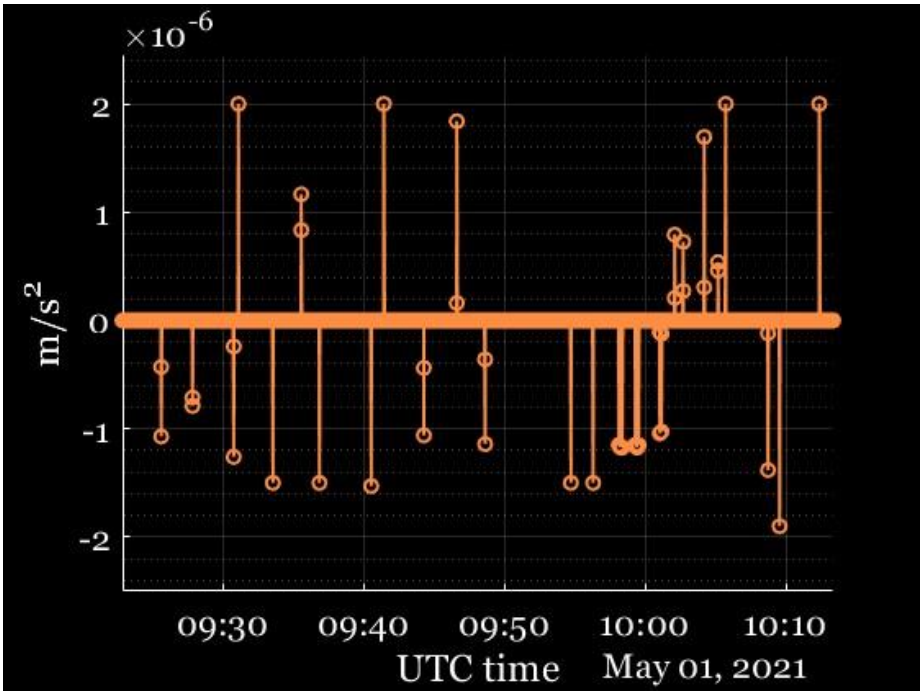

Figure 16: GRACE-C and -D differential mode (DM) acceleration in the SRF (Y-axis). GRACE-D ACT1A measurements are: 1) time-shifted towards GRACE-C; 2) rotated 180° in yaw; and 3) subtracted from ACT1A measurements. The deviations from zero are due to thruster activations from either GRACE-C or -D. The zero-valued DM accelerations highlight that the GRACE-C and -D accelerometer measurements are equivalent, only they are offset by the time-shift. Further, the GRACE-C and -D science reference frames are perfectly aligned at closest approach, meaning there is no gravitational gradient to estimate in the gradiometer mode (GM).

4 GRACE Single-Satellite Gradiometer Mode

As we demonstrated in Chapter 3, the dual-satellite GM (DS-GM) requires an operational accelerometer for the leading and trailing satellites. In this chapter, we develop a new configuration for gradiometer mode (GM), namely the single-satellite GM (SS-GM), that views an individual GRACE or GRACE-FO satellite as the fictitious 'gradiometer'. In particular, we develop this configuration in order to directly use the non-gravitational accelerations measured from the operational GRACE-C accelerometer, taking advantage of the available high sampling frequency of 10 Hz. This very-fast sampling interval achieves the necessary short 'gradiometer' baselines, without any interpolation for the linear accelerations. Our novel SS-GM configuration results in more robust estimates for the gravitational gradient tensor (GGT), as we demonstrate in our global investigations in geodynamically active regions, comparing both single- and dual- satellite gradiometer modes.

4.1 GRACE-C SS-GM processing methodology

To recover the GRACE-C calibrated non-gravitational linear accelerations, attitude, and positions in the Terrestrial Intermediate Reference Frame (TIRF, aka IRF), we use ACT1A (10 Hz), SCA1B (1 Hz), and GNI1B (1 Hz) data products, respectively (Wen et al., 2019). ACT1A is given in the accelerometer frame (AF) and in onboard computer (OBC) time. To correctly use the SCA1B data product to align the accelerometer frames, we transform AF to the science reference frame (SRF) by Equation (2.2). To use a common time reference, we use the TIM1B data product to map onboard-computer time to receiver (REC) time. From receiver time, we use the CLK1B data product to convert receiver to GPS time. We assume linear clock drifts, as TIM1B and CLK1B are given in 8 s sampling interval. We then interpolate the GRACE-C IRF positions and satellite attitude to the GPS time-tags of the 10 Hz accelerations in SRF using cubic splines.

Next, we create a 'thruster-free' ACT1A time-series for use in the GRACE-C SS-GM, as described in Chapter 2. In the context of GM, we consider thrusters as noise, since the accelerometer returns spurious measurements during thruster firings (McCullough et al., 2019). The creation of the 'thruster-free' accelerometer time-series requires the availability of the Level 1A accelerometer data product in 10 Hz. To calculate the gradients, we simply replace GRACE-A and -B in the

GRACE DS-GM processing flow (Section 3.5) with the ‘leading’ and ‘trailing’ GRACE-C, assigned from the successive positions of the single-satellite (SS) in its orbit. The 10 Hz sampling interval archives the necessary short ‘gradiometer’ baselines between the ‘leading’ and ‘trailing’ satellites, without the requirement of computing time-shifts and interpolation.

4.2 GRACE-A and -B DS-GM and -B SS-GM GGT comparison

In **Figure 17**, we extend our Himalayas gradient solution from GRACE-A and -B DS-GM and GOCE (**Figure 12** and **Figure 13**, respectively) to cover North Africa, comparing the vertical gradients for GRACE-A and -B DS-GM, GRACE-B SS-GM, and GOCE. For this investigation, we select GRACE-B for SS-GM arbitrarily, since GRACE-A and -B SS-GM results are very similar. For GRACE-B SS-GM, we interpolate the accelerations to 10 Hz using cubic splines to achieve the necessary short ‘gradiometer’ baselines. Both GRACE-A and -B (**Figure 17a**) and GRACE-B SS-GM (**Figure 17b**) observe the N-S changes in positive to negative anomaly over the Himalayas, as highlighted in the dashed purple boxes.

Over North Africa, DS-GM (**Figure 17a**) shows unknown features, whereas GRACE-B SS-GM (**Figure 17b**) features continue from the Himalayas to the Zagros fold and thrust belt (North Arabian Plate), then to the East Mediterranean Sea (Hellenic Arc subduction zone), continuing to the Calabrian Arc and to the north African plate at the convergent boundary, resulting in the formation of a subduction zone with the Eurasian tectonic plate. **Figure 17c** shows the higher resolution structure as seen from GOCE gradiometer. It is noted that the DS-GM map (**Figure 17a**) is markedly different from its equivalent calculated in SS-GM using satellite B (**Figure 17b**), most probably indicating that estimated biases of the GRACE-A and -B accelerometers contain systematic errors. The GRACE-B SS-GM solution is consistent with the geodynamics of the region studied.

The SS-GM and DS-GM should principally produce nearly identical results. However, one fundamental assumption of DS-GM is that GRACE-A and -B are identical (Peidou & Pagiatakis, 2019). In practice, the satellites and payload can never be identical, which when combined into the DS-GM estimate, may introduce bias and scale defects into the final GGT solution. For example, the GRACE-A and -B accelerometer bias and scale calibration factors identified by Bettadpur

(2009) are different for each accelerometer. Even if only one satellite is used, there may still exist the same scale defect in the recovered SS-GM GGT solution. However, from the previous results, it appears that the biases present in the accelerometers constitute a critical factor in DS-GM because they may distort the gradient patterns significantly. The complex and perhaps the non-linear interactions of scale and bias defects of two sets of satellite instrument and payload, when combined into the GGT estimate, are removed in SS-GM.

Moreover, in the SS-GM, we compute gradients using neighbouring accelerometer measurements of the same satellite. This is an advantage of SS-GM because, e.g., any residual angular accelerations will be nearly constant for the neighbouring accelerometer measurements of the same satellite, and will therefore be significantly reduced, or even eliminated from the differential mode (DM) accelerations. In contrast, the SS-GM GGT time-series also shows amplification of errors when the GM concept is not valid, because of, e.g., abrupt (short-wavelength) changes in the thermosphere, satellite maneuvers, or other anomalies. This facilitates the detection of outliers and their eventual elimination from the final gradient solutions. Hence, we expect to observe with improved fidelity and robustness using SS-GM gradients compared to the DS-GM, as highlighted in **Figure 17**.

We also note here that the SS-GM (**Figure 17b)** reflects the long-wavelength and thus the deeper Earth structure, compared to the GOCE gradients (**Figure 17c**) that are of much shorter-wavelength structure. A fair comparison between GRACE-B SS-GM and GOCE gradients would necessitate a low-pass filtering of the latter. We demonstrate this by performing a multi-resolution analysis (MRA) over the Java trench (south of Sumatra Islands) using both GOCE and GRACE-C SS-GM gradients in Section 5.1.

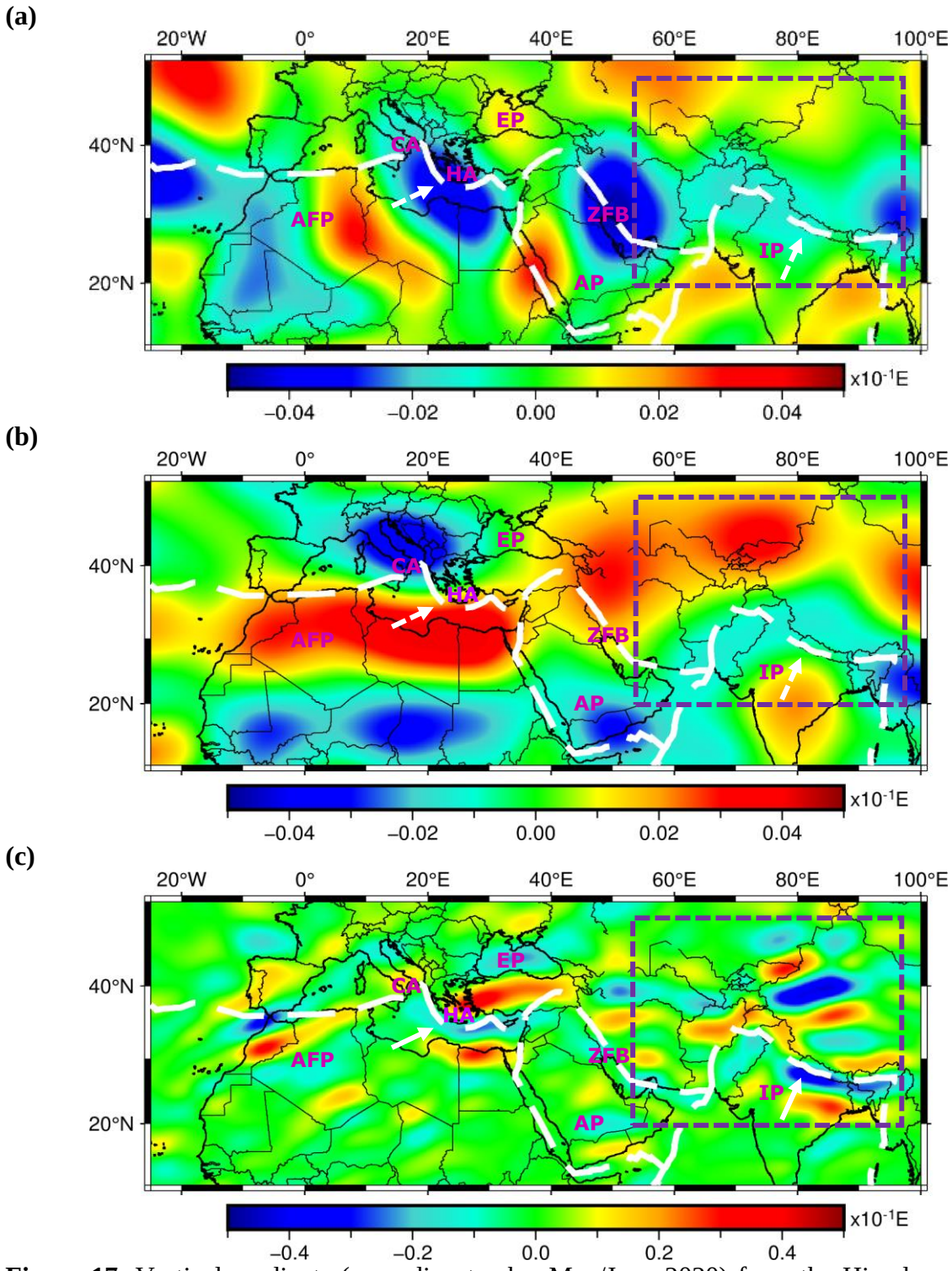

Figure 17: Vertical gradients (ascending tracks; May/June 2020) from the Himalayas to the North Africa regions. (a) GRACE-A and -B DS-GM; (b) GRACE-B SS-GM; and (c) GOCE. Tectonic plate boundaries are plotted in white dashed line and approximate plate movement is shown by white dashed arrow. AP – Arabian plate; AFP – African plate; CA – Calabrian arc; EP – Eurasian plate; IP – Indian plate; HA – Hellenic arc; ZFB – Zagros fold and thrust belt.

4.3 SS-GM GGT global investigation

To aid in the interpretation of our GRACE-C SS-GM gradients, we compute GRACE-FO CSR RL06 gradients referenced to 500 km altitude, using the International Centre for Global Earth Models (ICGEM) calculation service. The ICGEM gradients are calculated using GRACE-FO geopotential models (Level 2 data products) in the direction normal to the ellipsoid (V_{RR}), deviating from our vertical direction gradients (V_{UU}) by a very small (insignificant) deflection angle.

The Level 2 solutions are subject to numerous processing constraints using a-priori force models (Bettadpur et al., 2018), whereas our Level 1A and 1B GRACE-C SS-GM gradients are derived directly from the satellite measurements. Further, the Level 2 solutions are also contaminated by well-known errors such as 'longitudinal stripes' (along the meridians), proven to be sub-Nyquist artefacts that arise from an oversampling of the low-degree disturbing potential (Peidou & Pagiatakis, 2020; Pagiatakis & Peidou, 2021). Intriguingly, the GRACE SS-GM gradients do not show longitudinal stripes, only they are contaminated with 'latitudinal stripes' (along the parallels).

We have determined sources of the latitudinal stripes to correlate with field-aligned currents – FACs, and others to 'jumps' in the accelerometer measurements (see Section 5.2 for details). Analogous to the longitudinal stripes in the Level 2 models, other latitudinal stripes in GM gradients may originate from a critical sampling of the long-wavelength magnetic inclination. Nevertheless, we clearly observe very similar features between the two solutions as we demonstrate in the proceeding investigations, albeit to a different magnitude scale.

In **Figure 18**, we investigate the Himalayas and Northern Africa regions using GRACE C SS-GM. In **Figure 18a** and **Figure 18b**, the delineation of the Eurasian-Indian tectonic plate boundary is clear in the northern and vertical SS-GM gradients, respectively (gray dotted lines). These features then continue to the Arabian plate, delineating the Arabian-Eurasian tectonic plate boundary (**Figure 18a**; gray double-arrow line), and then onto the African plate, eventually deflecting to delineate the western African coast (gray dash-dot lines), and this is especially clear in **Figure 18a**. In **Figure 18a (**GRACE C SS-GM vertical gradients), we also see two north-west signals that are

bounded by the Arabian plate (gray solid line). In the GRACE-FO CSR RL06 radial gradients **(Figure 18d**), we also see nearly identical features of opposite transition from positive to negative anomaly in the Arabian plate (gray solid line), delineation of the Eurasian-Indian and Eurasian-Arabian tectonic plate boundaries (gray dotted line and gray double-arrow line, respectively), and a similar western deflection to trace the African coast (gray dash-dot line).

Similar to GRACE-A and -B DS-GM eastern gradients (**Figure 13a**), GRACE-C SS-GM eastern gradients in ascending tracks do not delineate (strongly or weakly) the Eurasian-Indian plate boundary in the Himalayas, with other unknown features elsewhere in the Northern African region. However, in October 2021 descending tracks (**Figure 18c**), the GRACE-C SS-GM eastern gradients over the Himalayas region show the expected transitions from positive to negative anomaly in the approximate N-S direction in shorter-wavelengths (gray dotted line), compared to GRACE-C SS-GM vertical (**Figure 18a**) and northern gradients (**Figure 18b**).

The eastern gradient features (**Figure 18c**; gray dotted line) in the Himalayas then continue to delineate the African coast, similar to the northern and vertical gradient components (approximately gray dash-dot line), albeit the solution does not delineate the plate boundaries well, unlike **Figure 18a** and **Figure 18b**. Hence, we observe variations in the ascending and descending track gradients solutions, as well as different apparent error characteristics for each '1-axis gradiometer'. These characteristics are also described in GOCE gradiometer (Rummel et al., 2011; Peidou & Pagiatakis, 2019).

Compared to GRACE-B SS-GM (**Figure 17b**), the GRACE-C SS-GM (**Figure 18a**) produces more robust gradients, since the GRACE-C SS-GM maps shorter-wavelength transitions from positive to negative anomaly over the Himalayas, more closely delineates the tectonic plate boundaries and the North African coastline, and also depicts the two north-west signals that are bounded by the Arabian plate in the vertical gradients, also seen in GRACE-FO CSR RL06 radial gradients. The improved GRACE-C SS-GM gradient estimates compared to GRACE-A and GRACE-B SS-GM are primarily due to the improved GRACE-FO data quality, the availability of the Level 1A accelerometer data product, and to the advancements in the satellite design, e.g., improved attitude determination aboard GRACE-FO (Kornfeld et al., 2019).

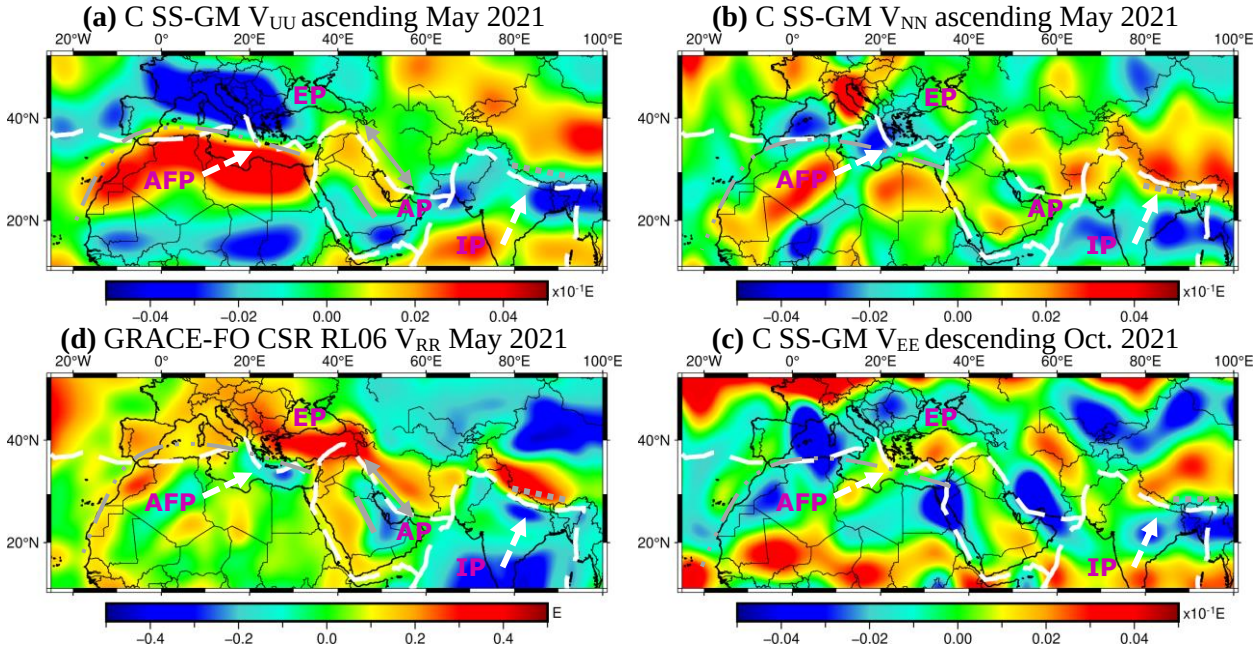

Figure 18: Himalayas and North Africa regions using GRACE-C SS-GM vertical and northern gradients in ascending tracks for May 2021 (panels (a) & (b)); (c) GRACE-C SS-GM eastern gradients in descending tracks for October 2021; and (d) GRACE-FO CSR RL06 radial gradients for May 2021. GRACE-FO CSR RL06 gradients are referenced to 500 km. Tectonic plate boundaries are plotted in white dashed line and approximate plate movement is shown by white dashed arrow. Gray lines denote features described in the text preceding the Figure. AP – Arabian plate; AFP – African plate; CA – Calabrian arc; EP – Eurasian plate; IP – Indian plate; HA – Hellenic arc; ZFB – Zagros fold and thrust belt.

For GRACE-C SS-GM, the mean absolute value separation as calculated for May 2021 is 800 m along X_{SRF}, 1 m along the Y_{SRF}, and 11 m along the Z_{SRF} axis 'gradiometer'. Compared to GRACE-A and -B DS-GM, the mean absolute value separation in May 2010 is 100 m along the X_{SRF}, 700 m along the Y_{SRF}, and 250 m along the Z_{SRF} axis 'gradiometer'. Therefore, the SS-GM 'gradiometer' average baseline separation magnitude is 230 times shorter than in DS-GM configuration, which is very promising, since measurement precision of a gradiometer is inversely proportional to the baseline separation (Rummel, 2003; Keller & Sharifi, 2005).

As a result of the shorter baselines and high-level of robustness observed in the vertical direction of the SS-GM gradients, we focus our proceeding investigations on the GRACE-C SS-GM vertical

calculations. Although the SS-GM Y_{SRF} 'gradiometer' has the shortest GM baselines[12], the Y-axis (SRF) accelerometer has high noise levels (Tzamali & Pagiatakis, 2023), and is also the least-sensitive axis (Bandikova et al., 2019). Given the Y_{SRF} is approximately aligned eastward, and justified by the instabilities we observe in GM eastern gradients, we therefore believe that the GM provides an indicator for accelerometer performance, a notion similarly implied by Peidou & Pagiatakis (2019).

In GRACE-C SS-GM vertical gradients (**Figure 19**), the purple dashed boxes over Africa highlight two features that are nearly identical to terrestrial water storage (TWS) anomalies, observed by GRACE in a nominal operation (Bonsor et al., 2018; Fig. 1). The red region (positive gradients) in Northern Africa is the Sahara Desert (Pinto et al., 2013; Fig 1). The green (zero) line/arch below (gold arrow line) delineates closely the Sahel region, a semi-desert that is a transitionary zone between the arid Saharah Desert to the north, and the semi-arid Sudan Savanna to the South (blue region in the purple dashed box, approximately above beige arrow).

The north-south midpoint of the blue region in the purple dashed box (beige arrow) closely delineates the maximum negative gradient line of the blue region, depicting the transition from the dry Sudan Savanna to the moist Guinea Savanna (light green arrow). The red region below this in the purple dashed box (green arrow) shows the Tropical rain forest in central Africa (very-wet region). In **Figure 19a** and **Figure 19b**, the gradients have different magnitudes, likely depicting significant hydrological changes that change on monthly time scales. Above the dashed box, there is the same delineation of the African coast seen in **Figure 17b** and **Figure 18a**, which continues from the Himalayas.

[12] The very -short Y-axis (SRF) gradiometer baselines probably explains the relatively shorter -wavelength eastern gradient features in **Figure 18c**.

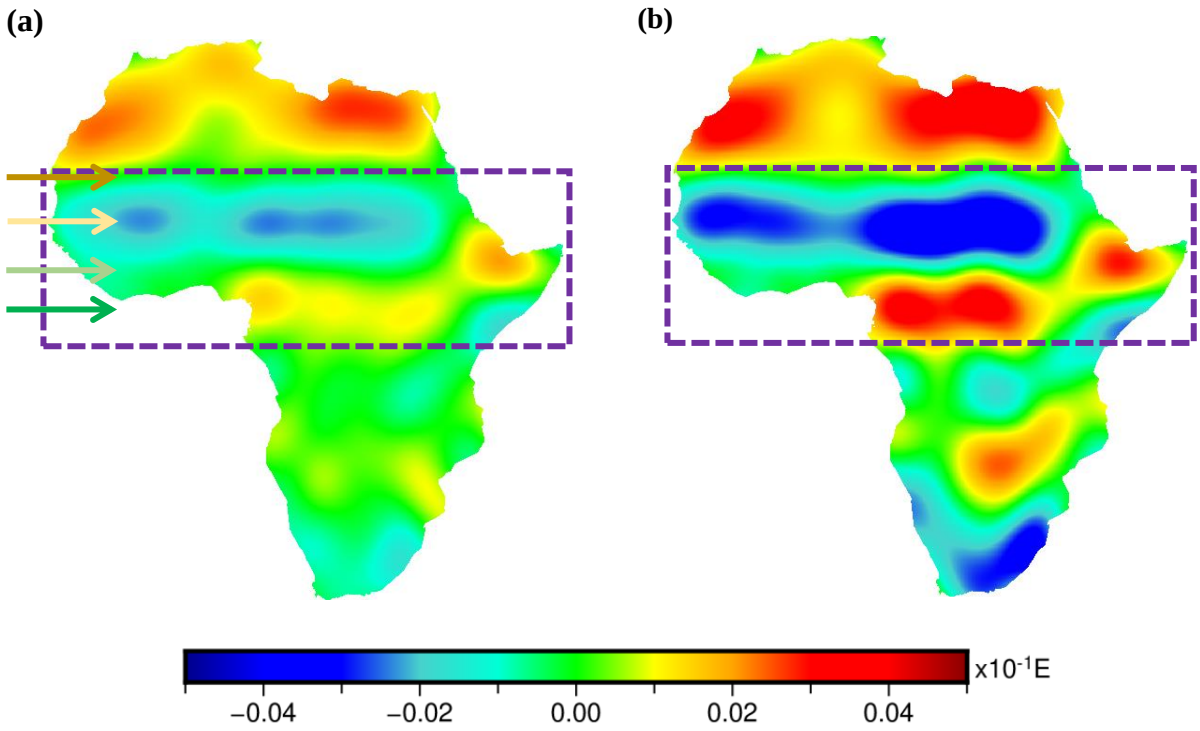

Figure 19: Africa using GRACE-C SS-GM vertical gradients in descending tracks. (a) October 2021 and (b) November 2021. Coloured lines denote features described in the text preceding the Figure. See Pinto et al (2013; Fig. 1) for map of Africa Biomes to accompany text preceding Figure.

In GRACE-C SS-GM (**Figure 20a**), the delineation of the Peru-Chile oceanic trench (also known as Atacama Trench; maximum depth of ~8km) is precise, formed from the subduction of the oceanic Nazca plate beneath the South American plate (Ye et al., 2020), with features to either side that similarly trace the subduction zone. In GRACE-FO CSR RL06 **Figure 20b**, the radial gradients instead delineate very closely the coastline, perhaps reflecting more shallow Earth structure anomalies.

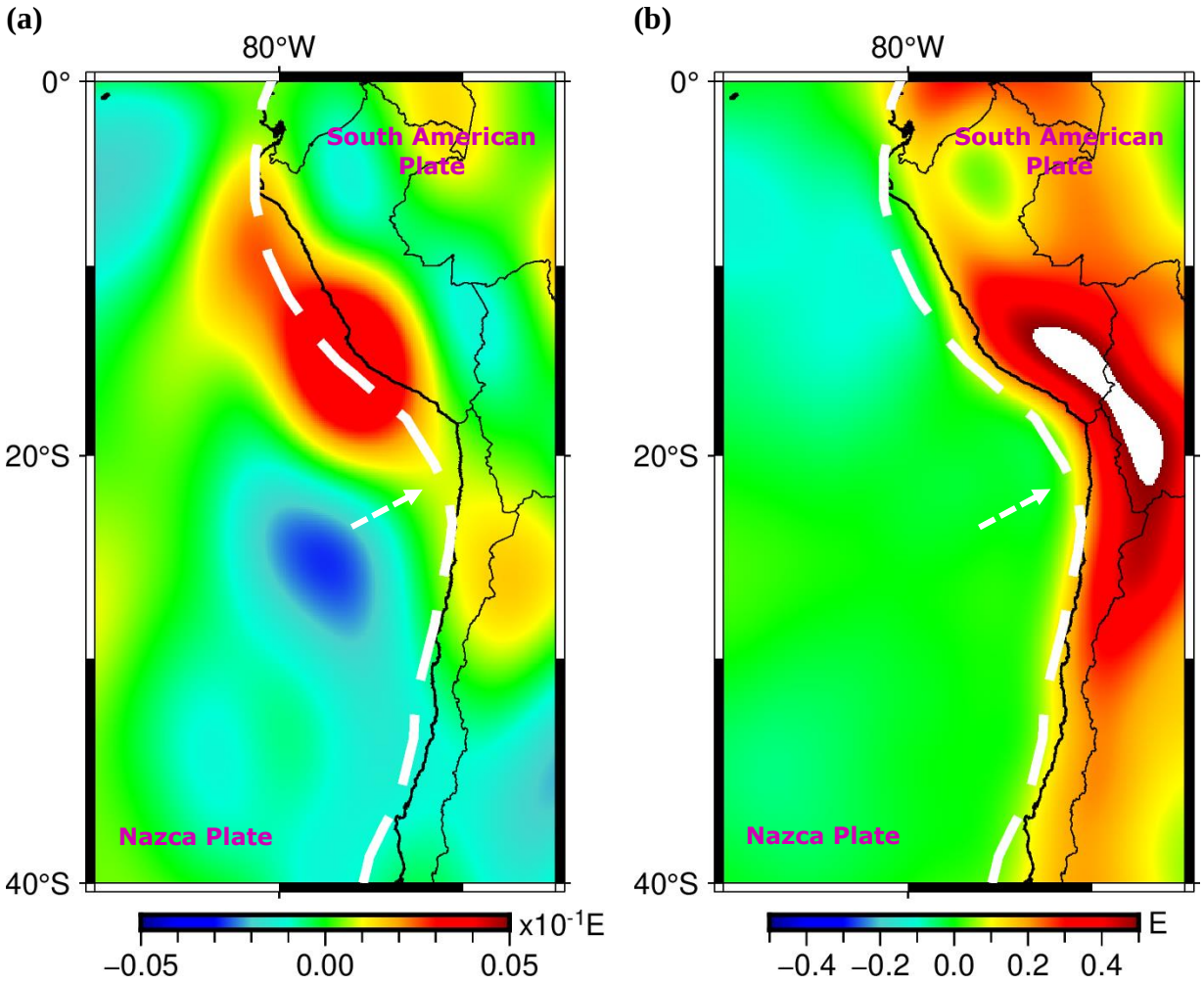

Figure 20: The Peru-Chile trench using (a) GRACE-C SS-GM V_{UU} gradients in ascending tracks and (b) GRACE-FO CSR RL06 V_{RR} gradients referenced to 500 km (September 2021). Tectonic plate boundaries are plotted in white dashed line and approximate plate movement is shown by white dashed arrow.

In GRACE-C SS-GM (**Figure 21a**), the delineation of the Aleutian trench, an oceanic trench at ~8km depth, is similarly very clear, quintessentially delineating precisely the tectonic plate boundaries, this time between the North American and Pacific plates, with the latter subducting under the former. In GRACE-FO CSR RL06 (**Figure 21b**), the radial gradients delineate the boundary in shorter-wavelengths. We note that the gradients obtained from GRACE-C in SS-GM delineates uniformly the Aleutian Trench at its entire length, from the Gulf of Alaska to Kamchatka and then to the south towards Kuril and Japan Trenches. The GRACE-FO CSR RL06 at 500 km altitude probably shows the shallower structure of the crust, yet further evidence that demonstrate

the gradients derived from our method depict the deeper structure of Earth crust, capable of delineating the deep trenches more precisely.

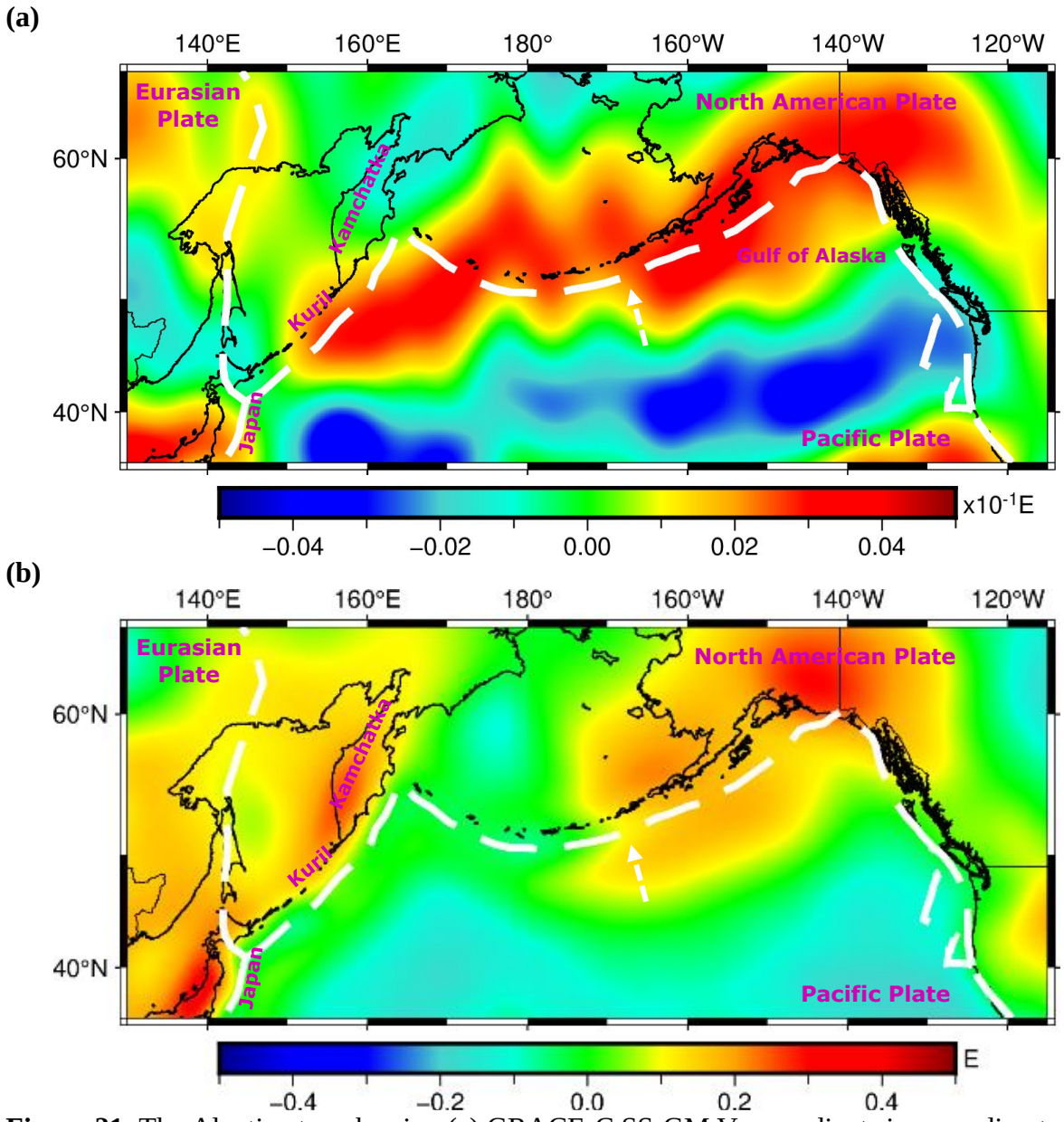

Figure 21: The Aleutian trench using (a) GRACE-C SS-GM V_{UU} gradients in ascending tracks and (b) GRACE-FO CSR RL06 V_{RR} gradients referenced to 500 km (June 2021).

In GRACE-C SS-GM vertical gradients (**Figure 22**), signals from glacial isostatic adjustment[13] (GIA) over Canada are apparent. During the last glacial maximum (LGM), the most recent glacial period, about 20,000 years ago, the Laurentide ice sheet covered most of Canada (Peltier, 2014; Métivier et al., 2016). The mass of the ice during the last glacial maximum pushed the crust downwards, sinking into the space of the relatively more-dense viscoelastic mantle, pushing the viscoelastic mantle away (Earle & Panchuk, 2019). Since then, the ice mass has been removed due to melting, and the crust and mantle are slowly rebounding after the glacial event. For example, the Hudson Bay region shows rebounding in the vertical direction at a maximum rate of ~ 15 mm/yr (Métivier et al., 2016).

The Laurentide ice sheet had a 'multi-dome configuration' (Stokes, 2017; Fig. 2), meaning it consisted of several centres of ice mass (domes), rather than a single, major dome centred in the Hudson Bay region, as initially thought (Stokes, 2017). The variation of mass and ice thickness clearly results in a much more complex process of GIA. In fact, the blue dome-like features over the Canadian shield (**Figure 22**) may reflect the non-uniform ice thickness during the last glacial maximum, as well as the melting of eastern and western Hudson Bay 'domes' (Peltier et al., 2015; Li et al., 2020).

The narrow green arch below the blue traces is very close to the zero line of GIA (Earle & Panchuk, 2019; Fig. 9.4.5), delineating the Canadian shield, while the gray solid line is closely correlated to the boundary between the Laurentide ice sheet to the east, and the Cordilleran ice sheet to the west. Further, the vertical gradient solution shows similar features to the time rate of gravity change (g-dot) pattern (Pagiatakis & Salib, 2003), to surface displacement solutions outlined by Koohzare (2007), and to the current rates of post-glacial isostatic uplift presented by Earle & Panchuk (2019; Figure 9.4.5). Based on previous results[14], where we have demonstrated that our GM solutions depict deep-Earth processes, the features (**Figure 22**) most likely similarly reflect the long-wavelength component of GIA, i.e., the rheology deep in the mantle (Johnston & Lambeck, 1999).

[13] Glacial isostatic adjustment describes the geodetic response to the growth and decay of ice sheets (Whitehouse, 2018).
[14] In section 5.1, we perform a multi -resolution analysis to further demonstrate that gradiometer mode (GM) gradients reflect long-wavelength signals and thus the deeper Earth structure.

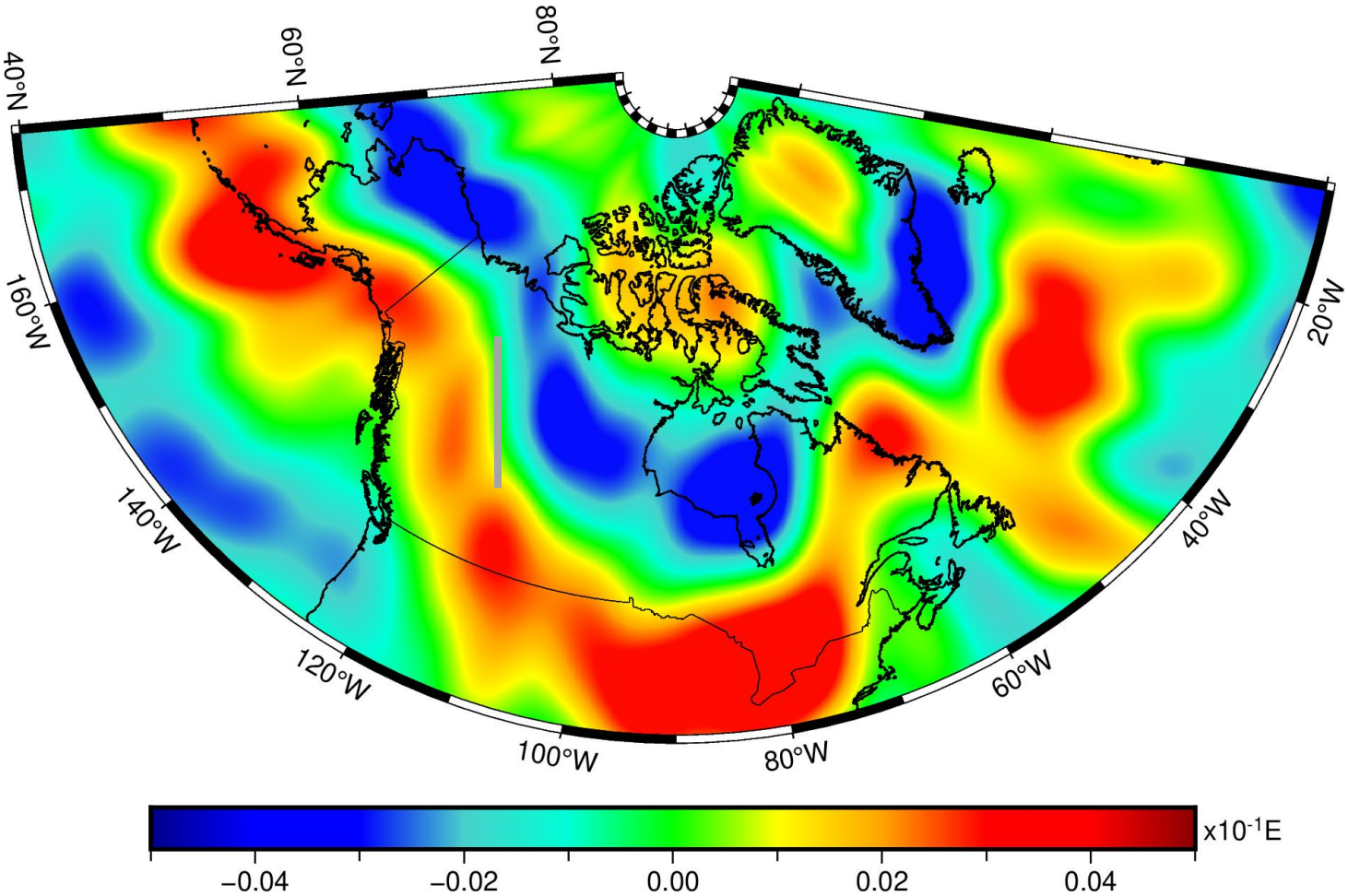

Figure 22: Glacial isostatic adjustment (GIA) over North America and Greenland using GRACE-C SS-GM vertical gradients in ascending tracks (August 2021). Gray lines denote features described in the text preceding the Figure.

5 Multi-resolution Analysis and Supplementary Investigations

In section 5.1 of this Chapter, we perform a multi-resolution analysis (MRA) over the Java trench to compare and assess GRACE-C single-satellite gradiometer-mode (SS-GM) and GOCE gradients. After, in section 5.2, we show how GM gradients can provide an indicator for accelerometer performance.

5.1 Multi-resolution analysis of the Java trench using SS-GM and GOCE

Multi-resolution analysis (MRA) has been demonstrated to be a useful tool for gravity field analysis, e.g., Peidou & Pagiatakis (2019) proved that the variable baseline separation of the GM 'gradiometers' extends the bandwidth of the gravitational gradient solution. In Section 3.2, we provided a theoretical review of the MRA. Now, we perform the MRA over the Java trench using GRACE-C SS-GM and GOCE gradients. The delineation of the Java trench (also known as the Sunda trench; maximum depth of ~8km), formed from the subduction of the Indian-Australian plate under the Eurasian plate (Meltzner et al., 2012), is clear in both GRACE-C SS-GM (**Figure 23**) and GOCE (**Figure 24)** gradients.

In **Figure 23**, we show that the effective bandwidth of the GRACE-C SS-GM is in Levels 1 through 6, or equivalently up to d/o (degree/order) 64 in the spherical harmonic (SH) expansion, while the GOCE gradients contain useful information in Levels 6 through 8 (d/o 32-256). This result demonstrates that the SS-GM provides nearly complementary geophysical information to GOCE, as a result of the long and dynamic 'gradiometer' baselines. Indeed, like the terrestrial water storage (TWS) anomalies over Africa, we also do not see the effects of glacial isostatic adjustment (GIA) over Canada clearly in the GOCE gradients.

The long-wavelength GM solutions are related to the very-long 'gradiometer' baselines that attenuate the short-wavelength gravitational gradient field (Brown et al., 2000), and to the higher GRACE-FO flight altitude that applies further attenuation (Martinec, 2014). Panet et al. (2014) outlined that their GOCE-based gradient solutions similarly traced plate boundaries and subduction zones, and they determined that the sources of the anomalies reach between 1000- 2500

km in depth. Since long-wavelength signals reflect deeper Earth structure variations (Garland, 1977; Smithson et al., 1979; Vaníček & Krakiwsky, 1986), we interpret the GRACE and GRACE-FO ‘gradiometers’ to probe deeper into the Earth than the GOCE gradiometer, reflecting very-deep Earth structure anomalies.

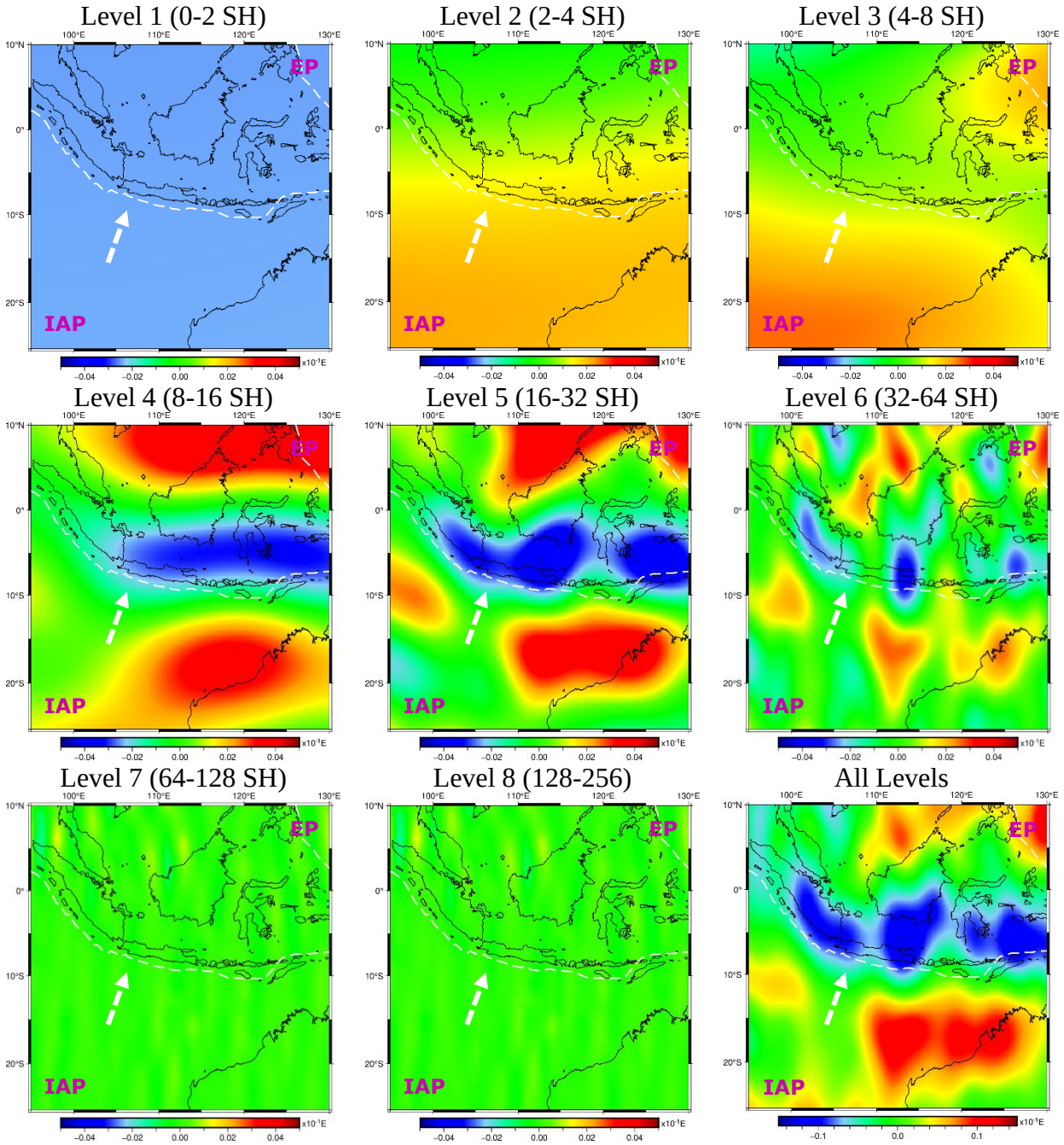

Figure 23: Multi-resolution analysis over Java trench showing the effective bandwidth of GRACE-C SS-GM vertical gradients (2021 and 2022). Monthly solutions are averaged to smooth time-variability of the gradient field. Tectonic plate boundaries are plotted in white dashed line and approximate plate movement is shown by white dashed arrow. IAP – Indian-Australian plate; EP – Eurasian plate.

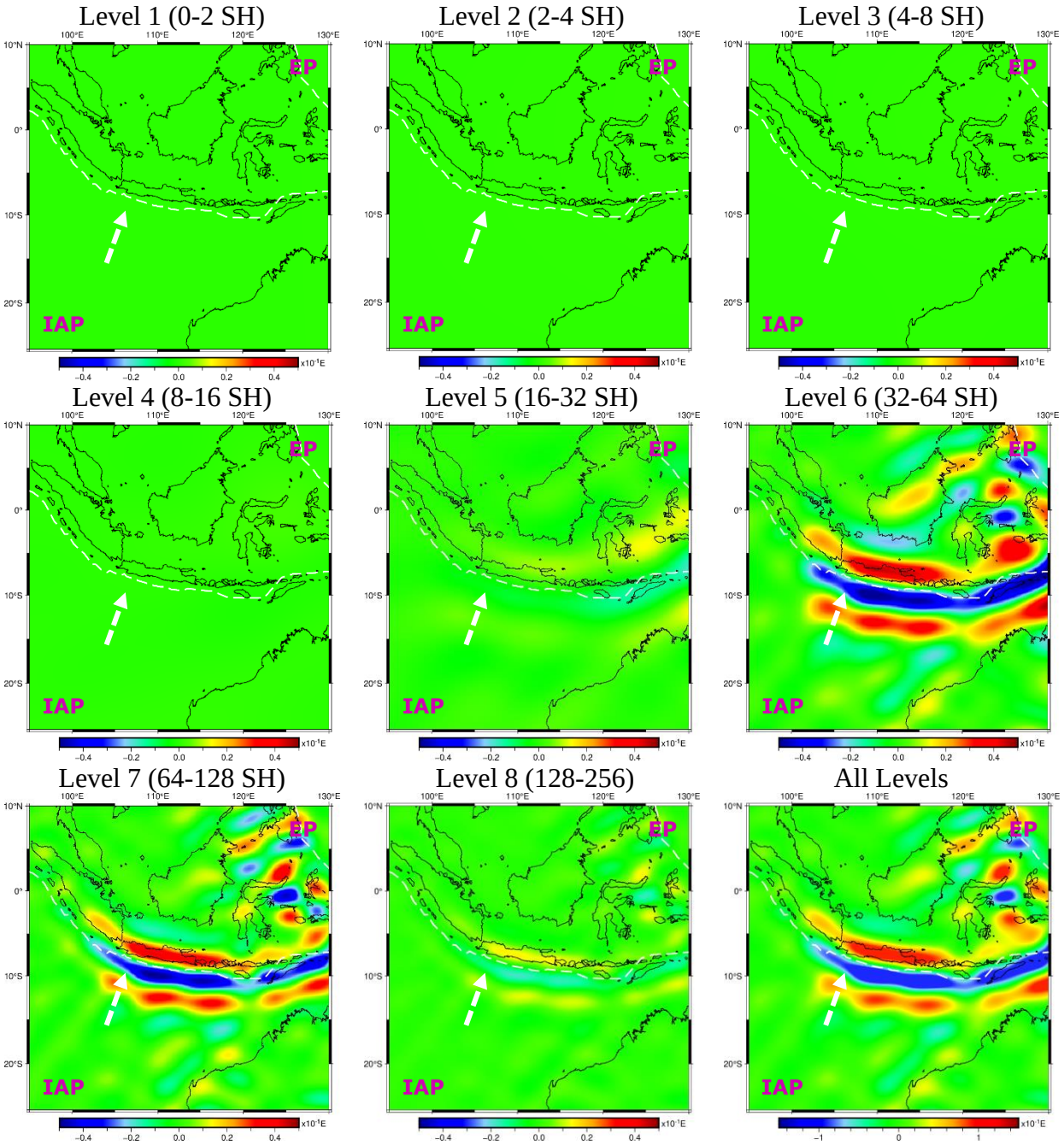

Figure 24: Multi-resolution analysis over Java trench showing the effective bandwidth of GOCE vertical gradients (2010). Monthly solutions are averaged to smooth time-variability of the gradient field. Tectonic plate boundaries are plotted in white dashed line and approximate plate movement is shown by white dashed arrow. IAP – Indian-Australian plate; EP – Eurasian plate.

5.2 Investigations of GRACE and GRACE-FO perturbations using SS-GM

In Chapter 3, we demonstrated that the gradiometer mode (GM) is valid when the non-gravitational perturbations affect both satellite accelerometers in the same (or similar) way. This is necessary to recover the attitude change of the satellite in the science reference frame (SRF), ideally isolated to the contribution of the gravitational gradients and removed from the non-gravitational perturbations. In our investigations of dual-satellite (DS) and single-satellite (SS) -GM, we observe that the GRACE and GRACE-FO payload are perturbed by three primary sources, where the ability for the non-gravitational to cancel in GM is minimized. These perturbations are related to: (1) electromagnetic disturbances; (2) 'jumps' in the accelerometer measurements; and (3) thruster activations that are necessary for attitude and orbit control (AOCS). Accordingly, GM can provide an indicator for accelerometer performance, similarly implied by Peidou & Pagiatakis (2019).

5.2.1 Field-aligned currents – FAC

GRACE orbits in the ionosphere, accumulates charge, and has EM torques induced through their interaction with Earth's magnetic field (Vaníček, 1973). FACs transfer energy between the magnetosphere and ionosphere (Xiong et al., 2021) and flow into the ionosphere in the polar regions (Knipp et al., 2014; Milan et al., 2017). Peidou and Pagiatakis (2020) first discovered a systematic class of accelerometer signatures in the GRACE dual-satellite GM (DS-GM) solutions. These signatures were confined to the 60^{th} parallel north in the satellite ascending tracks and were attributed to annual FACs over 2010. We wish to briefly expand on this discovery, which to our knowledge has not been surveyed since.

(a) GRACE-B GM V_{zz} ascending/Dec 2010 **(b)** GRACE-B GM V_{zz} ascending/Aug 2010

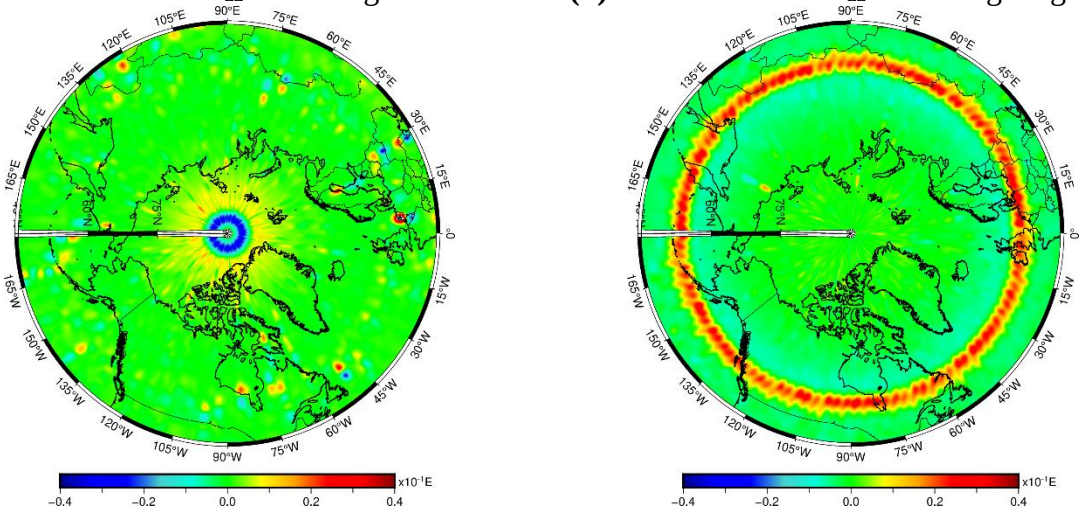

(c) GRACE-B V_{zz} GM descending/April 2010 **(d)** GRACE-B GM V_{zz} descending/June 2010

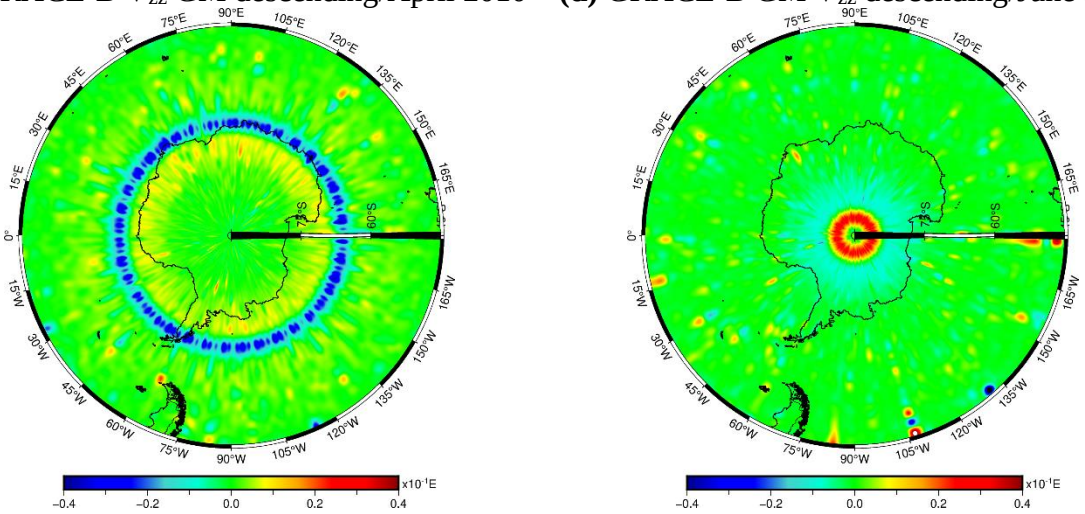

Figure 25: Field-aligned currents (FACs) perturbations in GRACE-B GM in V_{zz} (SRF) gradients. FACs are sensed in the northern and southern hemispheres, confined to different parallels of latitude. Each current ring has a corresponding inner or outer ring of alternate polarity, albeit it is of much lesser magnitude relative to the dominant ring.

In our analyses of FACs and GRACE, we see that the annual FACs over 2010 are contributions from July to September 2010 only. In **Figure 25b**, we show the contribution from August 2010 in ascending tracks. In further monthly investigations of GRACE and GRACE-FO, spanning nearly 20 years, we observe that depending on the month and year of investigation, similar signatures in the GM solutions appear in either (or both) hemispheres, in ascending tracks, descending tracks, or all tracks. In fact, they are confined to variable lines of parallels in the polar regions. Also, GRACE-A, -B and -C single-satellite GM (SS-GM) solutions are perturbed by FACs in a similar way. These disturbances appear in all 3-axis of the accelerometers simultaneously.

5.2.2 Accelerometer jumps

There is a rapid variation in solar radiation pressure (SRP) perturbation on the satellite when it enters and exists the Earth shadow (Tzamali & Pagiatakis, 2023). During the transitions, there may also be thermoelastic disturbances to the satellite and its payload (ESA, 2008), which may further disturb the accelerometer measurement response. These lumped processes are expressed as the jumps in the accelerometer data series (**Figure 26**). During the jumps, the differential mode (DM) accelerations show spikes, distorting the recovered gradient solutions. GM solutions are accordingly separated into ascending or descending track solutions to observe 'jump-free' GGT estimates.

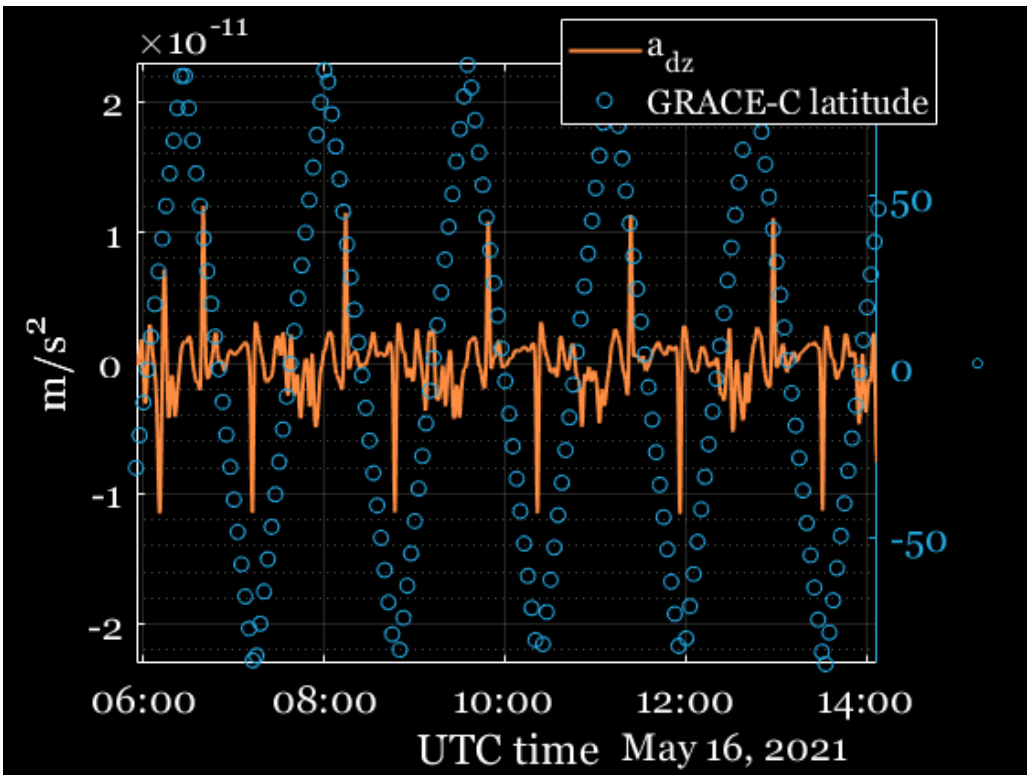

Figure 26: GRACE-C differential mode (DM) accelerations in Z-axis of the SRF. The spikes correspond to when the satellite enters and exits Earth's shadow. In May 2021, shadow crossings occur in descending tracks only.

5.2.3 Thruster activations

The accelerometer observes disturbances related to satellite operation, which are perhaps in response to the satellite flight environment. For instance, the accelerometers measure linear accelerations in response to thruster firings, necessary to control the satellite attitude and orbit. If

the thruster design and alignment were perfect, these residual accelerations would not be sensed by the accelerometer (Bandikova et al., 2019). When any of the magnetic torquer rods are parallel to the magnetic field, there is insufficient torque generated to control the satellite orientation (Bandikova et al., 2019). For this reason, the attitude thruster activations are very frequent and prominent in the mid-equatorial region and around the poles (**Figure 27**).

In the GRACE-A and -B DS-GM solutions, we see a systematic shift in ascending and descending track solutions which is most pronounced in the V_{yy} (SRF) direction. The shift in the solutions corresponds to the shift in thruster activations, which indicates that the residual accelerations from thruster activations constitute another area where the non-gravitational accelerations do not cancel effectively. To mitigate this noise disturbance, we use the 'thruster-free' accelerometer data series for GRACE-C SS-GM processing, as described in Chapter 2.

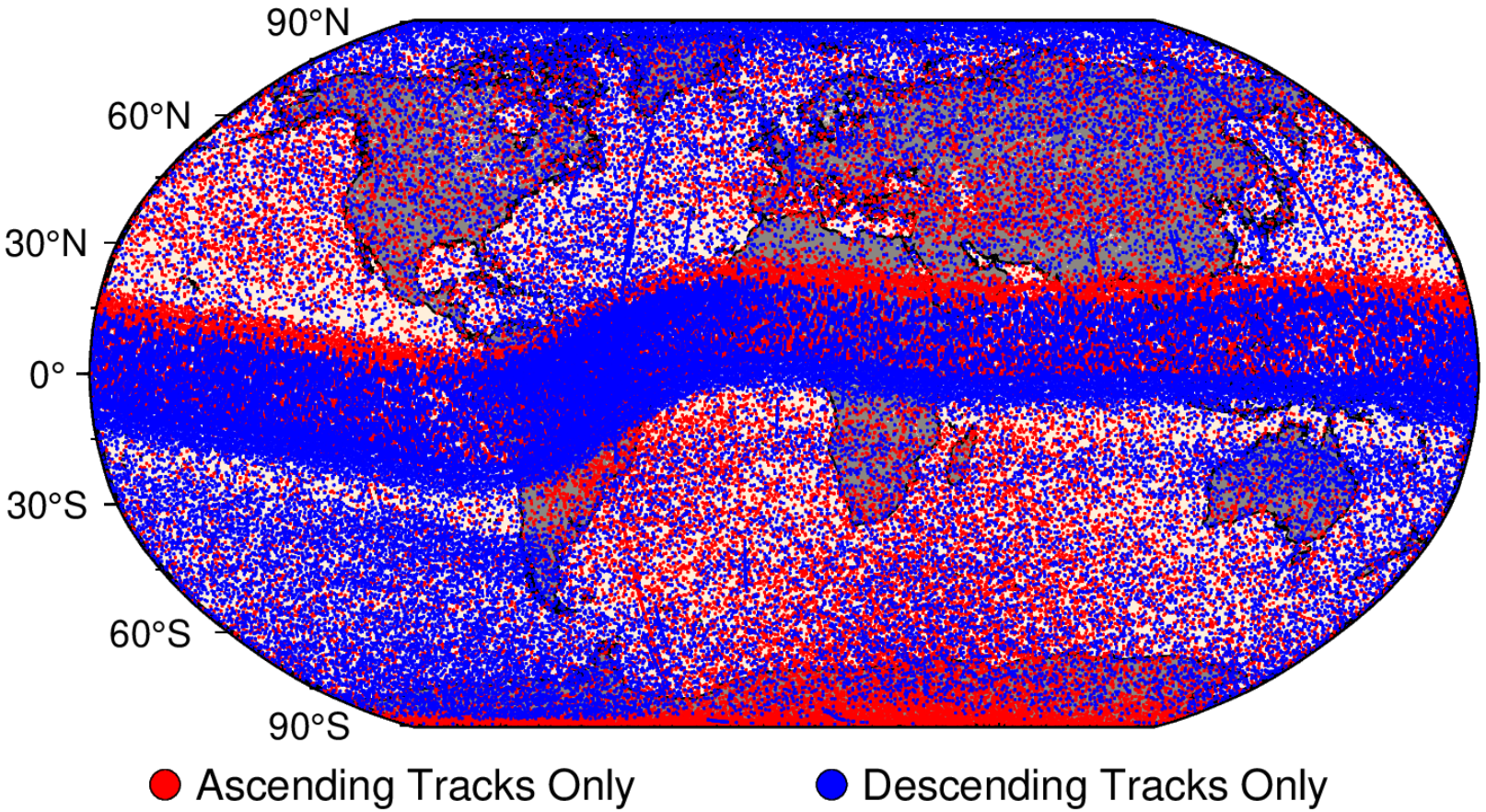

Figure 27: Geographic location of GRACE-C attitude and control thrusters in 2021. Along the geomagnetic equator, there is a deflection of the main cluster of thruster activations in ascending and descending tracks of about ~5°. There are also more thruster activations in the northern hemisphere for descending tracks, and more in the southern hemisphere for ascending tracks. These are both potentially related to how the satellite interacts with Earth's magnetic field in each orbit direction.

6 GRACE and GRACE-FO Gradiometer Mode Toolkit

We produce the results presented in Chapter 3, 4, and 5 using our GRACE and GRACE-FO Gradiometer Mode Toolkit (GGMT). In the research motivation of this thesis, we identified the need for a user-friendly and usable software package to produce gradients using the gradiometer mode (GM). Before this contribution, there has been no available software package for the GM. In this chapter, we provide a very-brief overview of the GGMT.

6.1 Software Manual Overview

The routines are hosted in an online repository, and the full manual is in APPENDIX A. The routines include detailed in-line comments with explanations. In addition to supporting GM, the GGMT offers a great foundation to support research objectives outside the scope of the work presented herein. Specifically, the GGMT is the first and only open-source GRACE and GRACE-FO suite of processing tools for Level 1A and 1B data products. The routines we have developed for, e.g., data product coordinate transformations, accelerometer calibration, and multi-resolution analyses (MRA), are general-purpose routines which can be used to process GRACE (and GOCE) gravity space mission data products for a wide variety of Earth and space science research efforts.

The format of the software manual in APPENDIX A follows a similar style as the “Algorithm Theoretical Basis Document for GRACE Level-1B Data ProcessingV1.2” document (Wu et al 2006). The GGMT is organized into three main processing modules: (1) **GGM1B_compute;** (2) **GGM2B_grid**; and (3) **GGM3B_visualize.** Each of these executable modules are façade modules. We use façade pattern to provide abstraction (encapsulation) for the more complex underlying code in order to improve code readability and ensure code reusability. The relevant data products for GGMT must be retrieved from NASA's Physical Oceanography Distributed Active Archive Center (PO.DAAC) via podaac.jpl.nasa.gov.

6.1.1 GGM1B_compute

The **GGM1B_compute** module calculates the gravitational gradient tensor (GGT) measurements in the leading Science Reference Frame (SRF); and provides GRACE GGT measurements with Global Position System (GPS) time-tags, geodetic (latitude/longitude) coordinates, data quality flags, and satellite vector separations at closest approach (in leading SRF). This is the GGM1B data product.

6.1.2 GGM2B_grid

The **GGM2B_grid** module computes the GGT in the GM reference frame (GRF); grids the GGT time-series; and then computes the average gradients in each grid cell. Optionally, it flags, detects, and removes outliers; applies additional filtering in time domain; separates ascending/descending track solutions; and references gradient solutions to the local East-North-Up (ENU) reference frame. This is the GGM2B data product.

6.1.3 GGM3B_visualize

The **GGM3B_visualize** module interpolates sparsely located values using the inverse distance as weights, if a grid cell is empty from **GGM2B_grid**; and then provides the GGT solutions in map or text file format for visualization in Generic Mapping Tools (GMT). Optionally, it band-pass filters/performs a multi-resolution analysis (MRA). This is the GGM3B data product.

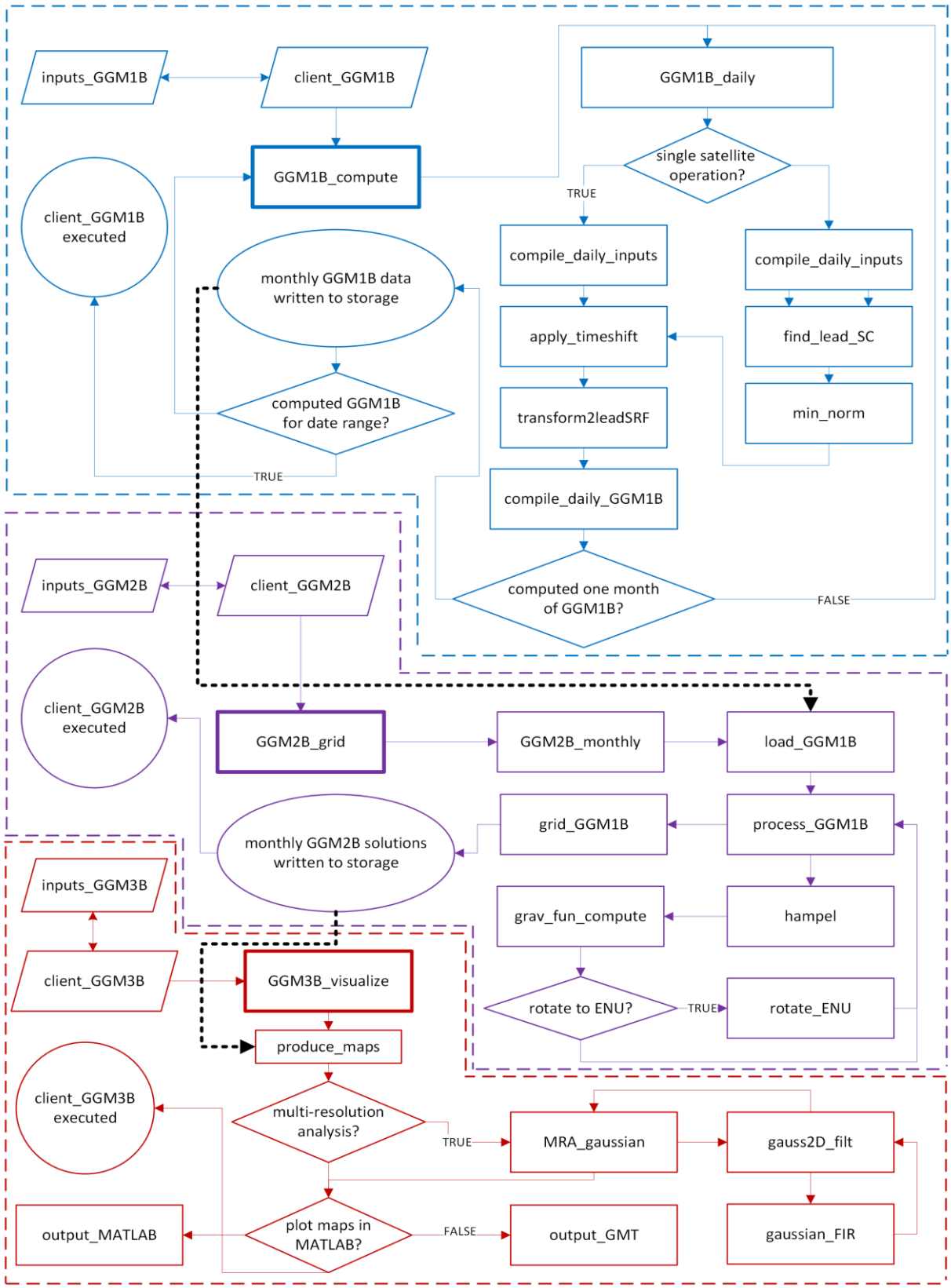

Figure 28: Flow diagram of the GRACE and GRACE-FO Gradiometer Mode Toolkit (GGMT). Blue is GGM1B_compute; purple is GGM2B_grid; and red is GGM3B_visualize.

7 Conclusions and Future Outlook

7.1 Concluding remarks

This contribution focused on the estimation of gravitational gradients using GRACE and GRACE-FO, two missions that were not designed to measure this observable, continuing the first seminal study from Peidou & Pagiatakis (2021). We focused on the new configuration for gradiometer mode (GM), which viewed an individual (single) GRACE or GRACE-FO satellite as the 'gradiometer' (SS-GM). Our efforts were primarily focused on SS-GM, since we demonstrated that the dual-satellite GM (DS-GM) configuration developed by Peidou & Pagiatakis (2019) required an operational accelerometer aboard both the leading and trailing satellites.

We investigated geodynamically active regions around the globe and demonstrated the sensing capabilities of GRACE and GRACE-FO 'gradiometers', by comparing GM configurations using one (SS-GM) and two (DS-GM) GRACE and GRACE-FO satellites. We discovered and demonstrated the benefits of the SS-GM approach, compared to DS-GM, which were further enhanced by GRACE-C improvements in data quality and satellite design.

We showed that using GRACE-C as a 'gradiometer' in SS-GM produces higher-fidelity gravitational gradient estimates, clearly delineating global tectonic plate boundaries and subduction zones in the Himalayas and North Africa regions, the Aleutian trench, the Java trench, and the Peru-Chile trench. This was a significant discovery to further prove that gradiometry using GRACE produces meaningful geophysical information.

Over Canada, we saw the delineation of the Canadian shield and the effect of glacial isostatic adjustment (GIA) was apparent. We also observed well-known signals resembling terrestrial water storage (TWS) changes in Africa, among others. Indeed, similar to the terrestrial water storage (TWS) anomalies over Africa, we also did not see the effects of glacial isostatic adjustment (GIA) over Canada clearly in the GOCE gradients. To assess the gradient solutions, we used a multi-resolution analysis (MRA) to demonstrate that the long and variable GRACE 'gradiometers' probed deeper into the Earth than the GOCE gradiometer, reflecting very-deep Earth structure anomalies.

Although the fictitious ‘gradiometers’ showed limitations, the GM gradients provided an indicator for accelerometer performance, a notion similarly implied by Peidou & Pagiatakis (2019). For instance, when the accelerometers in the GM at closest approach were not affected by non-gravitational perturbations in a similar way, we demonstrated that the GM amplified the perturbation signal in the gradients, providing an effective configuration for studying field-aligned currents (FACs), attitude thruster activations, and accelerometer measurement ‘jumps’ in the GRACE payload.

Our anticipation is that the results presented herein will harbour enthusiasm from geophysicists and other scientists to use our gradients estimated from GRACE. To produce GM gradients, we developed a user-friendly software package and manual, namely the GRACE and GRACE-FO Gradiometer Mode Toolkit (GGMT). Similar to how the GRACE Science Data System (SDS) translates raw satellite measurements into different levels of applied processing, GGMT users may produce Level 1, Level 2, and Level GGMT data products based on their research objectives.

7.2 Recommendations for future investigations

In our GM gradients, we observed that the magnitude of the gradients may change more than an expected change in the true gravitational gradient field. We believe that this may be related to scale and bias estimation defects in the SuperSTAR accelerometers. Therefore, future research work may investigate improved methodologies for estimating the calibration factor of the accelerometer and the resulting impact on the estimated gradients. For instance, the gradients may be re-computed using the accelerometer calibration factors estimated from the on-orbit calibration methodology proposed by Tzamali & Pagiatakis (2023, May), which estimated the accelerometer calibration factors based only on the satellite measurements. Other work can also investigate error estimates for the computed GM gradients.

Further, it may be possible to estimate the full gravitational gradient tensor (GGT) using the precise orbit determination (POD) trajectory solutions, instead of using the non-gravitational accelerations as initially proposed by Peidou & Pagiatakis (2019). To accomplish this, it may be required to compute the linear accelerations derived from the POD solutions, transform the computed accelerations to the science reference frame (SRF), and then ‘replace’ the non-gravitational

accelerations observed by the accelerometer with the POD derived accelerations in the nominal GM processing flow. In our preliminary results, we have seen that it may in fact be possible to estimate the gradients without using the non-gravitational accelerations measured, except there is more investigation required to understand the significance of the results, if any. For example, in **Figure 29**, we show the results of the GRACE-D SS-GM derived gradients using the POD derived accelerations in the SRF, in place of the accelerometer observed non-gravitational accelerations.

Based on the premise of this contribution, we have clearly demonstrated that the satellites experienced torques related to the gravitational gradients, and we therefore believe an improved transplanted accelerometer data product may consider the gradients. As we demonstrated, the GRACE-D transplanted accelerometer data product (ACT V04) does not consider gradients. Indeed, a new version of a transplanted GRACE-D accelerometer data product may incorporate gradient solutions from GRACE-C SS-GM.

Moving forward into the future of space-identified mass change (MC) determination, one of the five highest priority observables to advance Earth systems sciences over the next decade (National Academies, 2018), the European Space Agency (ESA), in collaboration with NASA/JPL, is planning the MC and Geosciences International Constellation (MAGIC) mission, with a tentative launch in 2028 to ensure continuity of observations (Massotti et al., 2021; Wiese et al., 2022). Based on combinations of in-line and Bender[15] orbit formations, enhanced SS-GM and DS-GM configurations can extend the future missions' usefulness beyond the MAGIC design principle for advanced geoscience applications. As described in Chapter 2, the MAGIC mission is currently adopting the laser ranger interferometer (LRI) as the primary payload. Accordingly, further improvements of the GM may similarly investigate the incorporation of LRI measurements into the GM concept. All together, these recommendations will help prepare for the immense scientific opportunities that will accompany the next generation of gravity space missions.

[15] A bender formation is one satellite pair in a polar orbit, and another pair in a lower inclined orbit (Bender et al., 2008; Wiese et al., 2022).

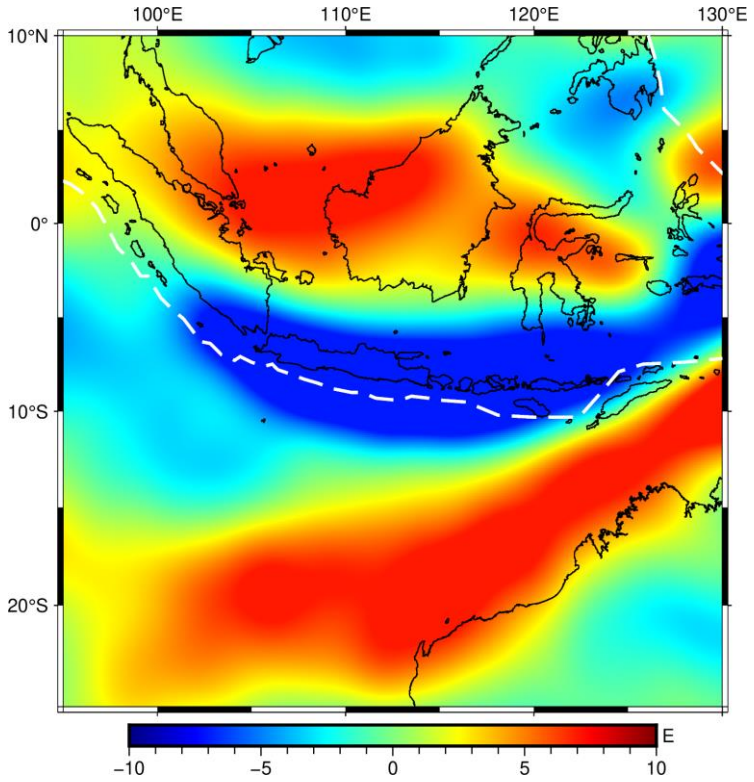

Figure 29: Java trench using GRACE-D SS-GM vertical gradients in ascending tracks (May 2021). The gradient solution is derived from POD and attitude measurements. The transplanted accelerations from C, nor the non-gravitational accelerations observed by GRACE-D onboard SuperSTAR accelerometer are used to produce the solution. GRACE-D is intentionally used for this solution, since the -D accelerometer is powered down.

8 References

1. Abich, K., Abramovici, A., Amparan, B., Baatzsch, A., Okihiro, B. B., Barr, D. C., ... & Zimmermann, M. (2019). In-orbit performance of the GRACE follow-on laser ranging interferometer. *Physical review letters*, *123*(3), 031101.

2. Amidror, I. (2015). Sub-Nyquist artefacts and sampling moiré effects. *Royal Society Open Science*, *2*(3), 140550. https://doi.org/10.1098/rsos.140550

3. Bandikova, T., Mccullough, C., Kruizinga, G. L., Save, H., & Christophe, B. (2019). GRACE accelerometer datatransplant. *Advances in Space Research*, *64*(3), 623-644. https://doi.org/10.1016/j.asr.2019.05.021

4. Barros, J., Diego, R. I., & De apraiz, M. (2012). Applications of wavelet transform for analysis of harmonic distortion in power systems: A review. *IEEE Transactions on Instrumentation and Measurement*, *61*(10), 2604-2611. https://doi.org/10.1109/TIM.2012.2199194

5. Behzadpour, S., Mayer-gürr, T., & Krauss, S. (2021). GRACE follow-on accelerometer data recovery. *Journal of Geophysical Research: Solid Earth*, *126*(5). https://doi.org/10.1029/2020JB021297

6. Bender, P. L., Wiese, D. N., & Nerem, R. S. (2008). A possible dual-GRACE mission with 90 degree and 63 degree inclination orbits. In *Proceedings of the 3rd International Symposium on Formation Flying, Missions and Technologies* (pp. 1-6). Noordwijk: ESA/ESTEC.

7. Bertiger, W., Desai, S. D., Haines, B., Harvey, N., Moore, A. W., Owen, S., & Weiss, J. P. (2010). Single receiver phase ambiguity resolution with GPS data. *Journal of geodesy*, *84*, 327-337.

8. Bettadpur, S. (2009). Recommendation for a-priori bias & scale parameters for level-1b ACC data. JPL Publication GRACE TN-02.

9. Bettadpur, S. V., Condi, F., Pekker, T., & Save, H. (2018). A quick-look atmosphere-ocean de-aliasing product for GRACE-FO. *AGU Fall Meeting Abstracts* (Vol. 2018, pp. G13C-0547).

10. Beyerle, G., Schmidt, T., Michalak, G., Heise, S., Wickert, J., & Reigber, C. (2005). GPS radio occultation with GRACE: Atmospheric profiling utilizing the zero difference technique. *Geophysical Research Letters*, *32*(13).

11. Bonsor, H., Shamsudduha, M., Marchant, B., Macdonald, A., & Taylor, R. (2018). Seasonal and decadal groundwater changes in african sedimentary aquifers estimated using GRACE products and lsms. *Remote Sensing*, *10*(6), 904. https://doi.org/10.3390/rs10060904

12. Borgeaud, M., Drinkwater, M., Silvestrin, P., & Rast, M. (2015, July). Status of the ESA earth explorer missions and the new ESA earth observation science strategy. In *2015 IEEE International Geoscience and Remote Sensing Symposium (IGARSS)* (pp. 4189-4192). IEEE.

13. Bottacchi, S. (2008). *Noise and signal interference in optical fiber transmission systems: An optimum design approach*. John Wiley & Sons.

14. Bouman, J., Ebbing, J., Fuchs, M., Sebera, J., Lieb, V., Szwillus, W., Haagmans, R., & Novak, P. (2016). Satellite gravity gradient grids for geophysics. *Scientific Reports*, *6*(1). https://doi.org/10.1038/srep21050

15. Bouman, J., Ebbing, J., Meekes, S., Abdul fattah, R., Fuchs, M., Gradmann, S., Haagmans, R., Lieb, V., Schmidt, M., Dettmering, D., & Bosch, W. (2015). GOCE gravity gradient data for lithospheric modeling. *International Journal of Applied Earth Observation and Geoinformation*, *35*, 16-30. https://doi.org/10.1016/j.jag.2013.11.001

16. Brown, J. M., Niebauer, T. M., Klopping, F. J., & Herring, A. T. (2000). A new fiber optic gradiometer for 4-D absolute differential gravity. *Geophysical Research Letters*, *27*(1), 33-36. https://doi.org/10.1029/1999gl010421

17. Brunton, S. L., & Kutz, J. N. (Eds.). (2019). *Data-driven science and engineering: Machine learning, dynamical systems, and control*. Cambridge University Press.

18. Case, K., Kruizinga, G., & Wu, S.-C. (2010). GRACE Level 1B Data Product User Handbook. JPL Publication D-22027.

19. Casotto, S., & Fantino, E. (2007). Evaluation of methods for spherical harmonic synthesis of the gravitational potential and its gradients. *Advances in Space Research*, *40*(1), 69-75. https://doi.org/10.1016/j.asr.2007.01.021

20. Cumming, I. G., & Wong, F. H. (2005). Digital processing of synthetic aperture radar data. *Artech house*, *1*(3), 108-110.

21. Doornbos, E. (2012). *Thermospheric density and wind determination from satellite dynamics*. Springer Science & Business Media.

22. Earle, S., & Panchuk, K. (2019). *Physical geology* (2nd ed.). BCcampus, BC Open Textbook Project.

23. ESA. (2008). GOCE L1b products user handbook. The European GOCE Gravity Consortium Publication EGG-GOCE GSEG-EOPG-TN-06-0137.

24. Eshagh, M. (2010). Towards Validation of Satellite Gradiometric Data Using Modified Version of 2 Order Partial Derivatives of Extended Stokes' Formula. *Artificial Satellites*, *44*(4), 103-129.

25. Fatolazadeh, F., & Goïta, K. (2021). Mapping terrestrial water storage changes in Canada using GRACE and GRACE-FO. *Science of The Total Environment*, *779*, 146435.

26. Flurry, J. (2017). Global gravity field modeling from satellite-to-satellite tracking data (M. Naeimi, Ed.). Springer International. http://doi.org/10.1007/978-3-319-49941-3

27. Freeden, W., Nashed, M. Z., & Sonar, T. (Eds.). (2010). *Handbook of geomathematics*. Springer Science & Business Media

28. Frommknecht, B. (2008). Integrated Sensor Analysis of the GRACE Mission. PhD thesis, Technische Universit¨at M¨unchen, https://mediatum.ub.tum.de/doc/630607/454947.pdf.

29. Fullea, J., Rodríguez-gonzález, J., Charco, M., Martinec, Z., Negredo, A., & Villaseñor, A. (2015). Perturbing effects of sub-lithospheric mass anomalies in GOCE gravity gradient and other gravity data modelling: Application to the atlantic-mediterranean transition zone. *International Journal of Applied Earth Observation and Geoinformation, 35*, 54-69. https://doi.org/10.1016/j.jag.2014.02.003

30. Garland, G. D. (1977). *The earth's shape and gravity* (1977 ed.). Pergamon Press.

31. Gelb, A. (1974). *Applied optimal estimation*. M.I.T. Press.

32. Gerlach, C., Flury, J., Frommknecht, B., Flechtner, F., & Rummel, R. (2005). GRACE Performance Study and Sensor Analysis.

33. Gerlach, O.h. (1965). Attitude stabilization and control of earth satellites. *Space Science Reviews, 4*(4). https://doi.org/10.1007/BF00177093

34. GFZ. (2022). 20th anniversary of launch of GRACE with guests from politics, industry, and science. Retrieved from (https://www.gfz-potsdam.de/en/press-public-relations/news/details/jubilaeum-20-jahre-grace-mission-mit-gaesten-aus-wisschenschaft-wirtschaft).

35. Ghaderpour, E., & Pagiatakis, S. D. (2017). Least-Squares wavelet analysis of unequally spaced and non-stationary time series and its applications. *Mathematical Geosciences, 49*(7), 819-844. https://doi.org/10.1007/s11004-017-9691-0

36. Ghobadi-Far, K., Han, S. C., McCullough, C. M., Wiese, D. N., Yuan, D. N., Landerer, F. W., ... & Watkins, M. M. (2020). GRACE Follow-On laser ranging interferometer measurements uniquely distinguish short-wavelength gravitational perturbations. *Geophysical Research Letters, 47*(16), e2020GL089445.

37. Ghobadi-far, K., Werth, S., Shirzaei, M., Loomis, B. D., Döhne, T., Willen, M. O., & Horwath, M. (2023). The impact of new accelerometer transplant data (ACH) on GRACE follow-on along-orbit inter-satellite laser ranging observations and monthly time-variable gravity and mascon solutions. *Journal of Geophysical Research: Solid Earth, 128*(6). https://doi.org/10.1029/2023jb026740

38. Gonzalez, R. C., & Woods, R. E. (2018). *Digital image processing* (4th ed.). Pearson.

39. Harvey, N., McCullough, C. M., & Save, H. (2022). Modeling GRACE-FO accelerometer data for the version 04 release. *Advances in Space Research*, *69*(3), 1393-1407.

40. Hofmann-Wellenhof, B., & Moritz, H. (2006). *Physical geodesy*. Springer Science & Business Media.

41. Hu, W. (2015). *Fundamental spacecraft dynamics and control*. John Wiley & Sons.

42. Ince, S, E. (2016). GOCE gradiometer measurement disturbances and their modelling by means of ionospheric dynamics. [Doctoral dissertation, York University]. YorkSpace. http://hdl.handle.net/10315/33646.

43. Ince, E. S., & Pagiatakis, S. D. (2017). GOCE gradiometer measurements response to ionospheric dynamics. *Journal of Geophysical Research: Space Physics*, *122*(10), 10-712.

44. Jenkins, G. M., & Watts, D. G. (1968). *Spectral analysis and its applications*. Holden-Day.

45. Johannessen, Johnny. (1999). The four candidate Earth Explorer core missions. Report for mission selection. 1. Gravity Field and Steady-state Ocean Circulation Mission.

46. Johnston, P., & Lambeck, K. (1999). Postglacial rebound and sea level contributions to changes in the geoid and the Earth's rotation axis. Geophysical Journal International, 136(3), 537-558.

47. Kang, Z., Bettadpur, S., Nagel, P., Save, H., Poole, S., & Pie, N. (2020). GRACE-FO precise orbit determination and gravity recovery. *Journal of Geodesy*, *94*, 1-17.

48. Kaplan, G. H. (2005). *The IAU resolutions on astronomical reference systems, time scales, and earth rotation models : explanation and implementation*. United States Naval Observatory.

49. Keller, W. (2004). *Wavelets in geodesy and geodynamics*. Walter de Gruyter.

50. Keller, W., & Sharifi, M.a. (2005). Satellite gradiometry using a satellite pair. *Journal of Geodesy*, *78*(9), 544-557. https://doi.org/10.1007/s00190-004-0426-x

51. Knipp, D. J., Matsuo, T., Kilcommons, L., Richmond, A., Anderson, B., Korth, H., Redmon, R., Mero, B., & Parrish, N. (2014). Comparison of magnetic perturbation data from LEO satellite constellations: Statistics of DMSP and AMPERE. *Space Weather*, *12*(1), 2-23. https://doi.org/10.1002/2013SW000987

52. Koohzare, A. (2007). *A Physically Meaningful Model of Vertical Crustal Movements in Canada Using Smooth Piecewise Algebraic Approximation: Constraints for Glacial Isostatic Adjustment Models*. Ph.D. dissertation, Department of Geodesy and Geomatics Engineering, Technical Report No.246, University of New Brunswick, Fredericton, New Brunswick, Canada, 174 pp.

53. Kornfeld, R. P., Arnold, B. W., Gross, M. A., Dahya, N. T., Klipstein, W. M., Gath, P. F., & Bettadpur, S. (2019). GRACE-FO: The gravity recovery and climate experiment follow-on mission. *Journal of Spacecraft and Rockets*, *56*(3), 931-951. https://doi.org/10.2514/1.a34326

54. Li, K., Zhou, X., Guo, N., Zhao, G., Xu, K., & Lei, W. (2017). Comparison of precise orbit determination methods of zero-difference kinematic, dynamic and reduced-dynamic of GRACE-A satellite using SHORDE software. *Journal of Applied Geodesy*, *11*(3), 157-165.

55. Li, T., Wu, P., Wang, H., Steffen, H., Khan, N. S., Engelhart, S. E., Vacchi, M., Shaw, T. A., Peltier, W. R., & Horton, B. P. (2020). Uncertainties of glacial isostatic adjustment model predictions in north america associated with 3D structure. *Geophysical Research Letters*, *47*(10). https://doi.org/10.1029/2020gl087944

56. Liebe, C. C. (1995). Star trackers for attitude determination. *IEEE Aerospace and Electronic Systems Magazine*, *10*(6), 10-16.

57. Luzum, B., & Petit, G. (2012). The IERS Conventions (2010): Reference systems and new models. *Proceedings of the International Astronomical Union*, *10*(H16), 227-228.

58. Mallat, S. G. (1999). *A wavelet tour of signal processing* (2nd ed.). Academic Press.

59. Mandea, M., Dehant, V., & Cazenave, A. (2020). GRACE—Gravity data for understanding the deep earth's interior. *Remote Sensing*, *12*(24), 4186. https://doi.org/10.3390/rs12244186

60. Mandea, M., Panet, I., Lesur, V., De viron, O., Diament, M., & Le mouël, J.-L. (2012). Recent changes of the earth's core derived from satellite observations of magnetic and gravity fields. *Proceedings of the National Academy of Sciences*, *109*(47), 19129-19133. https://doi.org/10.1073/pnas.1207346109

61. Martinec, Z. (2014). Mass-density green's functions for the gravitational gradient tensor at different heights. *Geophysical Journal International*, *196*(3), 1455-1465. https://doi.org/10.1093/gji/ggt495

62. Massotti, L., Siemes, C., March, G., Haagmans, R., & Silvestrin, P. (2021). Next generation gravity mission elements of the mass change and geoscience international constellation: From orbit selection to instrument and mission design. *Remote Sensing*, *13*(19), 3935. https://doi.org/10.3390/rs13193935

63. McCullough, C., Harvey, N., Save, H., & Bandikova, T. (2019). Description of Calibrated GRACE-FO Accelerometer Data Products. JPL Publication D-103863.

64. Meltzner, A. J., Sieh, K., Chiang, H. W., Shen, C. C., Suwargadi, B. W., Natawidjaja, D. H., ... & Briggs, R. W. (2012). Persistent termini of 2004-and 2005-like ruptures of the Sunda megathrust. Journal of Geophysical Research: Solid Earth, 117(B4).

65. Métivier, L., Caron, L., Greff-Lefftz, M., Pajot-Métivier, G., Fleitout, L., & Rouby, H. (2016). Evidence for postglacial signatures in gravity gradients: A clue in lower mantle

viscosity. *Earth and Planetary Science Letters*, *452*, 146-156. https://doi.org/10.1016/j.epsl.2016.07.034

66. Milan, S. E., Clausen, L. B. N., Coxon, J. C., Carter, J. A., Walach, M.-T., Laundal, K., Østgaard, N., Tenfjord, P., Reistad, J., Snekvik, K., Korth, H., & Anderson, B. J. (2017). Overview of solar wind–magnetosphere–ionosphere–atmosphere coupling and the generation of magnetospheric currents. *Space Science Reviews*, *206*(1-4), 547-573. https://doi.org/10.1007/s11214-017-0333-0

67. Misfeldt, M. M. (2019). *Data processing and investigations for the GRACE Follow-On laser ranging interferometer* (Master's thesis, Hannover: Leibniz Universität Hannover, Max Planck Institute for Gravitational Physics).

68. Misfeldt, M., Müller, V., Müller, L., Wegener, H., & Heinzel, G. (2023). Scale Factor Determination for the GRACE Follow-On Laser Ranging Interferometer Including Thermal Coupling. *Remote Sensing*, *15*(3), 570.

69. Pagiatakis, S., & Peidou, A. (2021). The intriguing structure of stripes in GRACE geopotential models. *Remote Sensing*, *13*(21), 4362. https://doi.org/10.3390/rs13214362

70. Pagiatakis, S. D., & Salib, P. (2003). Historical relative gravity observations and the time rate of change of gravity due to postglacial rebound and other tectonic movements in canada. *Journal of Geophysical Research: Solid Earth*, *108*(B9). https://doi.org/10.1029/2001jb001676

71. Panet, I., Pajot-métivier, G., Greff-lefftz, M., Métivier, L., Diament, M., & Mandea, M. (2014). Mapping the mass distribution of earth's mantle using satellite-derived gravity gradients. *Nature Geoscience*, *7*(2), 131-135. https://doi.org/10.1038/ngeo2063

72. Pearson, R. K., Neuvo, Y., Astola, J., & Gabbouj, M. (2016). Generalized hampel filters. *EURASIP Journal on Advances in Signal Processing*, *2016*(1). https://doi.org/10.1186/s13634-016-0383-6

73. Peidou, A. (2020). The new concept of GRACE gradiometry and the unravelling of the mystery of stripes, (Doctoral dissertation). Retrieved from YorkSpace (*http://hdl.handle.net/10315/37695)*. York University

74. Peidou, A., & Pagiatakis, S. (2019). Gravity gradiometry with GRACE space missions: New opportunities for the geosciences. *Journal of Geophysical Research: Solid Earth*, *124*(8), 9130-9147. https://doi.org/10.1029/2018JB016382

75. Peidou, A., & Pagiatakis, S. (2020). Stripe mystery in GRACE geopotential models revealed. *Geophysical Research Letters*, *47*(4). https://doi.org/10.1029/2019gl085497

76. Peidou, A. C., Fotopoulos, G., & Pagiatakis, S. (2017). On the feasibility of using satellite gravity observations for detecting large-scale solid mass transfer events. *Journal of Geodesy*, *92*(5), 517-528. https://doi.org/10.1007/s00190-017-1078-y

77. Peltier, W. R. (2004). Global glacial isostasy and the surface of the ice-age Earth: the ICE-5G (VM2) model and GRACE. *Annu. Rev. Earth Planet. Sci.*, *32*(1), 111-149.

78. Peltier, W. R., Argus, D. F., & Drummond, R. (2015). Space geodesy constrains ice age terminal deglaciation: The global ice-6g_c (VM5a) model. *Journal of Geophysical Research: Solid Earth*, *120*(1), 450-487. https://doi.org/10.1002/2014jb011176

79. Pinto, J., Egyir-Yawson, A., Vicente, J. L., Gomes, B., Santolamazza, F., Moreno, M., ... & della Torre, A. (2013). Geographic population structure of the African malaria vector Anopheles gambiae suggests a role for the forest-savannah biome transition as a barrier to gene flow. Evolutionary applications, 6(6), 910.

80. Poutanen, M., & Rózsa, S. (2020). The geodesist's handbook 2020. *Journal of Geodesy*, *94*, 1-343.

81. Press, W. H., Teukolsky, S. A., Vetterling, W. T., & Flannery, B. P. (1999). *Numerical recipes in C: The art of scientific computing* (2nd ed.). Cambridge University Press.

82. Richards, M. A., & Engebretson, D. C. (1992). Large-scale mantle convection and the history of subduction. *Nature*, *355*(6359), 437-440. https://doi.org/10.1038/355437a0

83. Rummel, R. (2003). How to climb the gravity wall. *Space Science Reviews*, *108*(1/2), 1-14. https://doi.org/10.1023/a:1026206308590

84. Rummel, R., Yi, W., & Stummer, C. (2011). GOCE gravitational gradiometry. *Journal of Geodesy*, *85*(11), 777-790. https://doi.org/10.1007/s00190-011-0500-0

85. Save, H. (2019). Gravity Recovery and climate experiment follow-on CSR level-2 processing standards document for level-2 product release 06, GRACE-FO D-103920 (v1. 1).

86. Seeber, G. (2003). *Satellite geodesy* (2nd ed.). Walter de Gruyter.

87. Shepherd, G. G., Thuillier, G., Cho, Y.-M., Duboin, M.-L., Evans, W. F. J., Gault, W. A., Hersom, C., Kendall, D. J. W., Lathuillère, C., Lowe, R. P., Mcdade, I. C., Rochon, Y. J., Shepherd, M. G., Solheim, B. H., Wang, D.-Y., & Ward, W. E. (2012). The wind imaging interferometer (WINDII) on the upper atmosphere research satellite: A 20 year perspective. *Reviews of Geophysics*, *50*(2). https://doi.org/10.1029/2012RG000390

88. Siemes, C. (2018). GOCE Level 1b gravity gradient processing algorithms. ESA Publication EOPSM-GOCE-TN-3397.

89. Smith, S. (2013). *Digital Signal Processing: A Practical Guide for Engineers and Scientists*. Newnes. https://doi.org/10.1016/B978-0-7506-7444-7/50050-9.

90. Smithson, S. B., Brewer, J. A., Kaufman, S., Oliver, J. E., & Hurich, C. A. (1979). Structure of the laramide wind river uplift, wyoming, from cocorp deep reflection data and from gravity data. *Journal of Geophysical Research*, *84*(B11), 5955. https://doi.org/10.1029/jb084ib11p05955

91. Stern, Robert J. "Ocean trenches." *Encyclopedia of Geology* 2 (2021): 845-854.

92. Stokes, C. R. (2017). Deglaciation of the Laurentide ice sheet from the last glacial maximum. *Cuadernos de investigación geográfica*, *43*(2).

93. Taylor, J. R., & Thompson, W. (1982). *An introduction to error analysis: the study of uncertainties in physical measurements* (Vol. 2, pp. 193-200). Mill Valley, CA: University science books

94. Telford, W. M. (1976). *Applied geophysics*. Cambridge University Press.

95. Tiwari, B., Arora, K., & Kumar, S. (2010). The potential of satellite gravity and gravity gradiometry in deciphering structural setting of the Himalayan Collision Zone. *Current Science (Bangalore)*, *99*(12), 1795–1800.

96. Touboul, P., Willemenot, E., Foulon, B. and Josselin, V., 1999. Accelerometers for CHAMP, GRACE and GOCE space missions: synergy and evolution. *Boll. Geof. Teor. Appl*, 40(3-4), pp.321-327.

97. Tzamali, M., & Pagiatakis, S. (2023, May). On-orbit Calibration of GRACE and GRACE-FO accelerometers. In *EGU General Assembly Conference Abstracts* (pp. EGU-10422).

98. Tzamali, M., & Pagiatakis, S. (2023). Non-gravitational accelerations: A study on the accelerometers of GRACE and GRACE-FO.

99. Vaníček, P. (1973). Gravimetric Satellite Geodesy. UNB Geodesy and Geomatics. Lecture Notes No. 32

100. Vaníček, P., & Krakiwsky, E. J. (1986). *Geodesy, the concepts*. North-Holland Pub.

101. Wang, Y., Li, M., Jiang, K., Li, W., Zhao, Q., Fang, R., Wei, N., & Mu, R. (2023). Improving precise orbit determination of LEO satellites using enhanced solar radiation pressure modeling. *Space Weather*, *21*(1). https://doi.org/10.1029/2022sw003292

102. Wen, H., Kruizinga, G., Paik, M., Landerer, F., Bertiger, W., Sakumura, C., Bandikova, T., Mccullough, C., 2019. Gravity Recovery and Climate Experiment Follow-On (GRACE-FO) Level-1 Data Product User Handbook. JPL Publication D-56935.

103. Whitehouse, P. L. (2018). Glacial isostatic adjustment modelling: historical perspectives, recent advances, and future directions. *Earth surface dynamics*, *6*(2), 401-429.

104. Wiese, D. N., Bienstock, B., Blackwood, C., Chrone, J., Loomis, B. D., Sauber, J., Rodell, M., Baize, R., Bearden, D., Case, K., Horner, S., Luthcke, S., Reager, J. T., Srinivasan, M., Tsaoussi, L., Webb, F., Whitehurst, A., & Zlotnicki, V. (2022). The mass change designated observable study: Overview and results. *Earth and Space Science*, *9*(8). https://doi.org/10.1029/2022ea002311

105. Wöske, F., Kato, T., Rievers, B., & List, M. (2019). GRACE accelerometer calibration by high precision non-gravitational force modeling. *Advances in Space Research*, *63*(3), 1318-1335.

106. Wouters, B., Bonin, J. A., Chambers, D. P., Riva, R. E. M., Sasgen, I., & Wahr, J. (2014). GRACE, time-varying gravity, earth system dynamics and climate change. *Reports on Progress in Physics*, *77*(11), 116801. https://doi.org/10.1088/0034-4885/77/11/116801

107. Wu, S., Kruzinga, G., & Bertiger, W. (2006). Algorithm Theoretical Basis Document for GRACE Level-1B Data Processing V1.2. JPL Publication D-27672.

108. Wu, M., Wang, K., Liu, J., & Zhu, Y. (2023). Relativistic effects of LEO satellite and its impact on clock prediction. *Measurement Science and Technology*, *34*(9), 095005.

109. Xiong, C., Stolle, C., Michaelis, I., Lühr, H., Zhou, Y., Wang, H., Kervalishvili, G., & Rauberg, J. (2021). Correlation analysis of field-aligned currents from the magnetic measurements of GRACE follow-on mission. *Earth, Planets and Space*, *73*(1). https://doi.org/10.1186/s40623-021-01540-y

110. Ye, L., Lay, T., & Kanamori, H. (2020). Anomalously low aftershock productivity of the 2019 MW 8.0 energetic intermediate-depth faulting beneath Peru. *Earth and Planetary Science Letters*, *549*. https://doi.org/10.1016/j.epsl.2020.116528

111. Zhang, S. P. (2003). Climatology of neutral winds in the lower thermosphere over millstone hill (42.6°N) observed from ground and from space. *Journal of Geophysical Research*, *108*(A1). https://doi.org/10.1029/2002JA009512

112. Zhou, R., & Wu, X. (2015). An iterative wiener filtering method based on the gravity gradient invariants. *Geodesy and Geodynamics*, *6*(4), 286-291. https://doi.org/10.1016/j.geog.2015.06.002

Appendix A

SOFTWARE PACKAGE: GRACE AND GRACE-FO GRADIOMETER MODE TOOLKIT

PROCESSING FLOW DOCUMENTATION

A.1 GGM1B_compute

The GGM1B data product is produced using five processing modules in sequence: **compile_daily_inputs, find_lead_SC, apply_timeshift, transform2leadSRF, compile_daily_GGM1B**. Each of these modules are described in the following sub-sections. The five modules are called in sequence in the **GGM1B_daily** module. For single-satellite GM (SS-GM), **find_lead_SC** is not used. Each of the modules depend on low-level routines, and we refer to the low-level routines (aka foundational blocks) as toolkit dependencies.

A.1.1 GGM1B_inputs

The processing parameters for **GGM1B_compute** (and sub-modules) is defined in the **GGM1B_inputs** object. Parse the object into to **GGM1B_compute** to generate the GGM1B data product.

Required and Optional Object Parameters:

- Path of Level 1B GRACE data products - required
- Current directory – required
- GGM1B path out (to write .MAT files) - required
- GRACE-ID – required
- Compute Start Date – required
- Compute End Date – required
- Accelerometer data product selection – required

    - See **compile_daily_inputs** for more information.
- Gradiometer Mode Configuration (i.e., single-satellite or dual-satellite) – required
- Accelerometer filtering type – optional
    - If selected, the filtering routine requires filter shape, filter cut-off(s), and number of filtering stages as input. See **gaussian_FIR.**
- Path of Level 1A GRACE-FO data products - optional
- Debug Mode – optional
    - Debug mode does not run in parallel processing mode, so the user can use the MATLAB debugger tool.

A.1.2 GGM1B_compute

GGM1B_compute calls **GGM1B_daily** for every day in the range (inclusive) of compute start date and compute end date. Every month of **GGM1B** data product generation is computed in parallel using MATLAB's parallel computing toolbox. After one month has been completed, the total outputs of **GGM1B_daily** for the entire month are returned to **GGM1B_compute** and then output to a .MAT file. An associated file specifying the input parameters for **GGM1B_compute** is also written out to storage. See **GGM1B_inputs**. After these two files are written out, the next month will begin computation until the processing date range for GGM1B data product generation has reached its upper temporal limit.

A.1.3 GGM1B_daily

Calls five processing modules in sequence: **compile_daily_inputs, find_lead_SC, apply_timeshift, transform2leadSRF, compile_daily_GGM1B**, with additional error checks.

Inputs:

1. Input structure. See **GGM1B_inputs.**

Outputs:

1. Daily GGM1B data product in MATLAB data table format. See **compile_daily_GGM1B**.

Dependencies:

compile_daily_inputs, find_lead_SC, apply_timeshift, transform2lead, compile_daily_GGM1B.

Algorithm:

1. SS-GM: Calls **compile_daily_inputs** for the requested date and GRACE ID.
2. DS-GM:
    a. Calls **compile_daily_inputs** for GRACE-A and GRACE-B, or GRACE-C and GRACE-D for the requested date.
    b. Determines the leading spacecraft ID along the flight trajectory using **find-_lead_SC**.
3. Pipelines outputs from step (2) for DS-GM/step (1) for SS-GM into **apply_timeshift**.
4. Pipelines outputs from step (3) into **transform2leadSRF** and then into **compile_daily_GGM1B**.

A.1.4 compile_daily_inputs

Compiles and pre-processes GRACE and GRACE-FO data products to compute the GGM1B data product.

Inputs:

1. Input structure. See **GGM1B_inputs**.

Outputs:

1. Accelerometer (ACC) data product in the Science Reference Frame (SRF).
2. Position coordinates in Inertial Reference Frame (IRF) interpolated to the ACC data product time -tags.
3. SCA1B (rotational quaternions) data product interpolated to ACC data product time-tags.

Dependencies:

read_ACC, get_ACCinSRFfromGPS, read_ACT1A_thrustFREE, gaussian_FIR, read_ACT1B, read_ACC1B, truncate_data2pad, ACC_upsample, GGM1B_inputs,

read_GNI1B_IRF, read_GNV1B_ITRF, ITRFtoIRF, interp_spline, read_SCA1B, flip_quats, get_GRACE_coord, find_SCA1B_gaps, avg_sample_rate, timeOBC2GPS, read_CLK1B, read_TIM1B, find_grace_header, find_gracefo_header.

Algorithm:

1. Loads the ACC linear accelerations based on user selection. See **read_ACC.**
    a. For GRACE, the ACC data product is either ACC1B accelerations with calibration factors applied, or precise orbit determination (POD) solution derived accelerations in the selected GRACE-ID SRF. Calibration factors for the ACC1B data product are determined by McCullough et at., (2019) and are applied using **calib_ACC**.
    b. For GRACE-FO, the ACC data product is either ACT1A, ACT1B, 'thruster-free' ACT1A , or POD solution derived accelerations in the selected GRACE-FO ID SRF. ACT1A data products are transformed from the accelerometer frame (AF) to SRF and are also mapped from onboard computer time (OBC) to GPS time using **timeOBC2GPS**, **read_CL1K1B,** and **read_TIM1B**. These coordinate transformations are done internally in **read_ACT1A.**
    c. POD derived accelerations are computed using **get_ACCinSRFfromGPS.**
2. Optionally, Performs zero-phase (forward/background) filtering to the ACC data product. **See gaussian_FIR**.
3. Interpolates the ACC data products to 10 Hz using cubic splines.
4. Loads position coordinates in IRF from the GNI1B data product using **read_GNI1B_IRF**, and then interpolates to time-tags of ACC data using cubic splines.
    a. For GRACE, the GNI1B data product is not released. The positions are only given in the ITRF in the GNV1B data product. The **read_GNI1B_IRF** routine calls **read_GNV1B_ITRF** to load the positions from the GNV1B data product, and then transforms the ITRF positions to IRF using **ITRFtoIRF** internally.
5. Loads rotational quaternions from the SCA1B data product. See **read_SCA1B.**
6. Corrects the quaternions, and then interpolates to ACC data using splines.
    a. The quaternion correction flips signs of the 4 quaternions, if needed, to maintain continuity in time to ensure reliable interpolation. See **flip_quats**. The correction

is called internally in **read_SCA1B**.

A.1.5 find_lead_SC

Determines the leading and trailing satellite along the flight trajectory.

Inputs:

1. IRF position coordinates for GRACE-A or GRACE-C.
2. Rotational quaternions from the SCA1B data product interpolated to IRF positions.

Outputs:

1. The ID of the leading satellite
2. The ID of the trailing satellite.

Dependencies:

IRFtoSRF.

Algorithm

1. Transforms the positions for all epochs (input 1) in IRF to the SRF using rotational quaternions from the first epoch only (input 2).
2. Applies the discrete forward derivative operator to transformed positions.
    a. The result of step (2) is negative if GRACE-A or GRACE-C is the leading satellite and is positive if GRACE-B or GRACE-D is leading. This is because the SRF has the X_{SRF} pointing towards the other satellite. If the result from step 3) is neither all negative nor all positive (i.e., mixed), an error is thrown.
3. Returns the leading and trailing satellite ID.

A.1.6 apply_timeshift

Applies time-shifts to move the trailing satellite to be as close as possible into the air-space of the leading satellite.

Inputs:

1. Input structure. See **GGM1B_inputs**.

2. Outputs from **compile_daily_inputs**.

Outputs:

1. Time-shifted trailing and leading satellite input (2).

Dependencies:

min_norm.

Algorithm:

1. For SS-GM:
    a. Applies a relative one index offset (shift) to input (2) in order to assign the 'time-shifted trailing' and 'leading' satellites. The leading and trailing satellite are the same satellite.
2. For DS-GM:
    a. Computes time-shifts to move the trailing satellite as close as possible to the leading satellite air-space, and then uses then uses evaluated time-shifts to index input (2) to assign the 'time-shifted trailing satellite'. Computes time-shifts by minimizing the L2 (Euclidean) norm of the 3D position separation in IRF between the trailing satellite positions in the interval $[t, t + 50s]$ and the leading satellite position at epoch t. Calculates time-shifts for every epoch of the leading satellite positions from input (2).

A.1.7 transform2leadSRF

Transforms all measurements to the leading satellite SRF.

Inputs:

1. Outputs (1) from **apply_timeshift**.

Outputs:

1. Outputs (1) from **apply_timeshift** in the leading SRF.

Dependencies:

SRFtoIRF, **IRFtoSRF.**

Algorithm:

1. Transforms the time-shifted trailing satellite ACC data from SRF to IRF using SCA1B data of the trailing satellite. SCA1B data is interpolated to the time-tags of ACC data. See **SRFtoIRF**.
2. Transforms time-shifted trailing satellite ACC data from IRF to SRF using SCA1B data of the leading satellite. SCA1B data is interpolated to the time-tags of the leading satellite for which the trailing satellite is time-shifted towards (i.e., in the airspace), determined by the **apply_timeshift** module.
3. Transforms time-shifted trailing satellite and leading satellite position coordinates in IRF to leading satellite SRF. See **IRFtoSRF**.

A.1.8 compile_daily_GGM1B

Compiles daily GGM1B data product in a MATLAB data table format.

Inputs:

1. Outputs (1) from **transform2leadSRF**.

Outputs:

1. Daily GGM1B data product.

Dependencies:

find_SCA1B_gaps, get_GRACE_coord

Algorithm:

1. Determines geodetic ITRF coordinates (latitude and longitude) of the leading satellite. See **get_GRACE_coord**, a wrapper for **ecef2geodetic**.
2. Returns quality warnings when interpolated SCA1B data is interpolated using data that has gaps larger than 5 seconds.

a. Precise attitude determination given by the SCA1B data product is critical for the GM, and therefore gappy SCA1B data should probably not be included in gradient measurements. See **find_SCA1B_gaps**.

A.2 GGM2B_grid

The generation of the GGM2B data product (gridded gradient measurements) from the GGM1B data product involves three processing modules: **load_GGM1B**, **process_GGM1B, grid_GGM1B**. These 3 modules are called in sequence and wrapped by **GGM2B_monthly** which are then encapsulated by the façade **GGM2B_grid**.

A.2.1 GGM2B_inputs

The processing parameters for **GGM2B_compute** (and sub-modules) is defined in the **GGM2B_inputs** object. Parse the object into to **GGM2B_compute** to generate the GGM2B data product.

Required and Optional Object Parameters:

- Working directory – required
- Compute Start Date – required
- Compute End Date – required
- Directory of GGM1B data – required
- Rotation of GGM2B in SRF to local East-North-Up (ENU) frame – optional
- Differential accelerations filtering type – optional

A.2.2 GGM2B_grid

GGM2B_grid calls **GGM2B_monthly** for every day in range (inclusive) of compute start date and compute end date. Every month of GGM1B data product, processed using **GGM1B_compute**, is loaded and gridded using **GGM2B_monthly** until all months in the compute date range have been processed. Once this has been completed, the total outputs of all gridded gradient measurements are returned to **GGM2B_grid** and then output to a .MAT file. An associated file specifying the input parameters for **GGM2B_grid** is written out. See **GGM2B_inputs**

A.2.3 GGM2B_monthly

Calls three processing modules in sequence: **load_GGM1B**, **process_GGM1B, grid_GGM1B**, with additional error checks.

Inputs:

1. Input structure. See **GGM2B_inputs**.

Outputs:

1. Monthly GGM2B monthly solutions. See **grid_GGM1B**.

Dependencies:

load_GGM1B, process_GGM1B, grid_GGM1B.

Algorithm:

1. Pipelines results from **load_GGM1B** to **process_GGM1B** to **grid_GGM1B**.

A.2.4 load_GGM1B

Reads in the outputs of **GGM1B_compute**. There is no processing performed in this utility.

A.2.5 process_GGM1B

Performs outlier removal; computes and filters gravity gradient derived from GGM1B data product in GMRF; rotates to an ENU frame if selected; removes flagged data; and also segregates GGM1B data into ascending track and descending tracks.

1.2.5.1 Inputs:

1. Input structure. See **GGM2B_inputs**,
2. Outputs from **load_GGM1B**.

1.2.5.2 Outputs:

1. Processed gravitational gradient tensor (GGT) in ascending track, descending track, and all track solutions.

1.2.5.3 Dependencies:

grav_fun_compute, rotate_ENU, ascending_tracks, descending_tracks, filtBYsegments, hampel (MATLAB).

1.2.5.4 Algorithm:

1. Calculates the differential mode positions and accelerations referenced in the leading SRF.
2. Applies a Hampel outlier identification algorithm (moving median) to the differential positions to identify and remove when the GRACE satellites operate in nadir-pointing mode. See **hampel** (MATLAB).
3. Filters the differential positions and optionally filters the differential accelerations. The differential positions are low-pass filtered using a corner frequency of $10^{3.5}$ Hz.
    a. The filtering processes are done in segments. A new segment of the input series is created when there is a data gap greater than 500 seconds. For every gap in the input series, the filtering procedure is restarted. If there are no gaps larger than 500 seconds, the filtering procedure assumes there is only one segment. See

filtBYsegments. **filtBYsegments** calls **gaussian_FIR**.

b. Differential positions less than 0.1 m are flagged because differential positions below this threshold significantly modulate the gravitational gradient signal.

4. Calculates the GGT in GMRF using the differential mode positions and accelerations.
5. Optionally transforms the output the GGT in GMRF to the local ENU frame. See **rotate_ENU**.
    a. Calculates the azimuth of the satellite ground track. See **azimuth** (MATLAB). Uses the calculated azimuths to create rotation matrices about the Z-axis of GMRF. The transformation is about the Z-axis of GMRF and aligns the X-axis of the GMRF to North, and Y-axis of the GMRF to East. The Z-axis is kept zenith pointing.
6. Removes flagged GGM1B data and isolates into ascending track and descending track solutions.

A.2.6 grid_GGM1B

Grids the GGT time-series.

1.2.6.1 Inputs:

1. Input structure. See **GGM2B_inputs**
2. Outputs from **process_GGM1B**.

1.2.6.2 Outputs:

1. Gridded global GGT in (1) ascending tracks; (2) descending tracks; and (3) all tracks.

1.2.6.3 Dependencies:

gridbin (Chad, A)

1.2.6.4 Algorithm:

1. Uses **gridbin** (Chad, A) to grid the GGT time-series with one-degree bin spacing and then computes the average value in each bin.

A.3 GGM3B_visualize

The generation of the GGM3B solution from GGM2B data involves one processing module: **produce_map**. This module is encapsulated by **GGM3B_visualize**.

A.3.1 GGM3B_inputs

The processing parameters for **GGM3B_visualize** (and sub-modules) is defined in the **GGM3B_inputs** object. Parse the object into to **GGM3B_visualize** to generate the GGM3B data product.

Required and Optional Object Parameters:

- Working directory – required
- Directory of GGM2B data – required
- Compute Start Date – required
- Compute End Date – required
- Output mode – required
    - 'MATLAB' to produce mapping solutions in MATLAB
    - 'GMT' to produce XYZ text files to be plotted in GMT
- Number of monthly GGM2B solutions to average- required
- 2D filtering wavelength – optional
- Ascending tracks solution only – optional
- Descending track solution only – optional

A.3.2 GGM3B_visualize

GGM3B_visualize calls **produce_map** in a step size equal to the number of monthly GGM2B solutions to average solutions in the range (inclusive) of compute start date and compute end date. For example, if compute start date is 2022/1 and compute end date is 2022/12, and the number of monthly solutions to average is 6 – two sets of 6-month GGM3B solutions would be produced: one from 2022/1 to 2022/6 and another set from 2022/7 to 2022/12. Outputs of **GGM3MB_visualize** are saved in the directory of the GGM2B data under a folder named "plot".

A.3.3 produce_map

Produces gravitational maps using GGM2B data product in MATLAB, or outputs XYZ data to be plotted in GMT.

Inputs:

1. Input structure. See **GGM3B_inputs**.

Outputs:

1. Gravitational map visualized in MATLAB or XYZ data output in text file.

Dependencies:

MRAgaussian, gauss2D_filt, output_MATLAB, output_GMT, filt2 (Chad, A)

Algorithm:

1. Loads computed GGM2B data product and then extracts monthly gradient solutions which correspond to the requested monthly range.
2. If necessary, performs inverse weighting to fill missing gradient grid cells. See **filt2** (Chad, A).
3. Averages monthly GGM2B solutions, if requested.
4. If requested, performs 2D Gaussian low-pass filtering. See **gauss2D_filt**.
5. If requested, performs 2D multiresolution analysis (MRA) to either:
    a. Decomposes gradient solution to 7 levels.
    b. Isolates gradient solution to specific levels of decomposition and then resynthesizes the decomposition. See **MRAgaussian**.
6. Visualizes output(s) from step 5) in MATLAB or returns a text file for GMT plotting. See **output_MATLAB, output_GMT**.